Diss. ETH No. 19943

Experimental Realization of the Dicke Quantum Phase Transition

A dissertation submitted to the
ETH ZÜRICH

for the degree of
Doctor of Sciences

presented by

KRISTIAN GOTTHOLD BAUMANN

Dipl.-Phys.,
Technische Universität München, Germany

born 7.4.1983 in Leipzig, Germany
citizen of Germany

accepted on the recommendation of
Prof. Dr. Tilman Esslinger, examiner
Prof. Dr. Johann Blatter, co-examiner

2011

Zusammenfassung

In dieser Arbeit wird die erste experimentelle Realisierung des Quantenphasenüberganges im Dicke Modell vorgestellt. Wir betrachten die Quantenbewegung eines Bose-Einstein Kondensates die an einen optischen Resonator gekoppelt ist. Konzeptionell ist der Phasenübergang durch langreichweitige Wechselwirkungen induziert, die zum Entstehen eines selbstorganisierten suprasoliden Zustandes führen.

Der Quantenphasenübergang im Dicke Modell wurde bereits 1973 vorhergesagt. Vor dieser Arbeit konnte dieser aber wegen grundlegenden und technologischen Gründen experimentell nicht nachgewiesen werden. Durch die Verwendung von atomaren Impulszuständen konnten wir diese Herausforderung nun bewältigen. Die Impulszustände werden durch Zweiphotonen-Übergänge miteinander gekoppelt, wobei je ein Photon aus dem Resonator und ein Photon aus einer transversalen Lichtwelle gebraucht werden. Diese offene Implementierung des Dicke Modells erlaubt es alle relevanten Parameter einzustellen und bietet eine einzigartige Detektionsmethode in Echtzeit.

Wir zeigen in dieser Doktorarbeit, dass der Phasenübergang von einem makroskopisch besetzten Feld im Resonator und einer starken Veränderung der atomaren Impulsverteilung begleitet ist. Diese Impulsveränderung wird durch spontane Selbstorganisation der atomaren Dichte auf einem Schachbrettmuster hervorgerufen. Wir haben die Grenze des Phasenübergangs durch Variieren von zwei Parametern im Dicke Modells abgetastet und das gemessene Phasendiagramm stimmt mit der Modellbeschreibung überein.

Die superradiante Phase erlaubt zwei verschiedene geometrische Konfigurationen was unausweichlich zu dem Konzept der spontanen Symmetriebrechung am Phasenübergang führt. Wir können die beiden Zustände experimentell unterscheiden und haben die Ursache für den Symmetriebruch untersucht. Die endliche räumliche Ausdehnung unseres Systems induziert außerdem eine kleines symmetriebrechendes Feld, welches sich zufällig zwischen jeder experimentellen Realisierung ändert.

Abstract

We report on the first experimental realization of the Dicke quantum phase transition realized in the quantum motion of a Bose–Einstein condensate coupled to an optical cavity. Conceptually, the transition is driven by cavity-mediated long-range interactions, giving rise to the emergence of a self-organized supersolid phase.

The Dicke phase transition, predicted in 1973, has not been demonstrated experimentally before this work, both due to fundamental and technological reasons. These challenges have been overcome in the present thesis by employing atomic momentum states of a Bose-Einstein condensate, which are coupled via two-photon Raman transitions involving a cavity photon and a free-space pump photon. This open-system implementation of the Dicke model allows to tune all relevant parameters and offers a unique detection scheme to monitor the many-body system in real time.

We demonstrate that the phase transition is accompanied by a macroscopically occupied cavity field and a striking change in the atomic momentum distribution, due to spontaneous self-organization of the atomic density on a checkerboard lattice. The boundary of the transition is mapped out by scanning two parameters of the Dicke model, to reveal a phase diagram in close agreement with the model description.

Two different ordered configurations are allowed in the superradiant phase, giving rise to the concept of spontaneous symmetry breaking at the phase transition. We experimentally distinguish the symmetry-broken states and study the origin of the symmetry-breaking process. The finite spatial extension of our system induces a small symmetry-breaking field which changes randomly on each experimental realization. The influence of this field is studied and shown to diminish upon dynamically crossing the transition point with increasing transition rates.

Contents

1 Introduction **1**

2 Theoretical Framework **5**
2.1 Atoms in an Optical Cavity 5
2.1.1 A Single Atom 5
2.1.2 The Jaynes-Cummings Model 7
2.1.3 Atomic Motion 7
2.1.4 Elimination of the Excited State 9
2.2 Self-Organization of Atoms in a Cavity 12
2.2.1 Light Scattering by Atoms 12
2.2.2 Scattering by an Ensemble 12
2.2.3 Buildup of an Interference Potential 13
2.2.4 The Self-Organization Phase Transition 14
2.2.5 Long-Range Interaction 15
2.3 Mean-Field Description 16
2.3.1 Mean-Field Equations 16
2.3.2 Steady State 17
2.3.3 Phase Boundary 17
2.3.4 Normal and Ordered Phases 18
2.3.5 Numerical Results 19
2.4 The Dicke Model 23
2.4.1 Coupling of Momentum States 23
2.4.2 Mapping to the Dicke Model 23
2.4.3 The Dicke Phase Transition 26
2.4.4 Numerical Diagonalization 27
2.4.5 Thermodynamic Limit 28
2.4.6 Energy Spectrum 29
2.4.7 Long-Range Interaction 30
2.5 Symmetry Breaking 33
2.5.1 Second-Order Phase Transition 33
2.5.2 Finite-Size Effect 34

3 Experimental Setup **37**
3.1 Experimental Sequence 37
3.1.1 MOT - Transport - QUIC 38
3.1.2 Optical Transport and Trapping 39

3.2 The High-Finesse Cavity 40
3.3 The Transverse Pump 40
3.4 Single-Photon Counting Module 42
3.5 Balanced Optical Heterodyne Setup 42
3.6 Data Acquisition Software 47

4 The Dicke Phase Transition with a Superfluid Gas 49
4.1 Introduction 50
4.2 Theoretical Description and Dicke Model 51
4.3 Observing the Phase Transition 54
4.4 Mapping out the Phase Diagram 56
4.5 Methods 58
  4.5.1 Experimental Details 58
  4.5.2 Mapping to the Dicke Hamiltonian 59
  4.5.3 Derivation of the Phase Boundary in a Mean-Field Description 60
4.6 Conclusions and Outlook 61

5 Symmetry Breaking at the Dicke Phase Transition 63
5.1 Introduction 64
5.2 Realizing the Dicke Model 64
5.3 Observing Symmetry Breaking 66
5.4 Crossing Rate 67
5.5 Coherent Switching 69

6 Dynamical Coupling of a BEC and a Cavity Lattice 71
6.1 Introduction 72
6.2 Experimental setup 73
6.3 Theoretical description 73
6.4 Bistability measurement 75
6.5 Dynamics 77
6.6 Conclusion 78

7 Conclusions and Outlook 79

A Rotating-Frame Transformation 81

B Numerical Methods 83

C Physical constants 87

Bibliography 88

List of Publications 101

Acknowledgments 103

Curriculum Vitae 105

1 Introduction

A fundamental model to describe the interaction between light and matter is the Dicke model which has been introduced by Robert H. Dicke in 1954 [1]. This model has been studied extensively since the early years of quantum optics and it became a paradigmatic example to describe collective quantum behavior. In this thesis we present the first experimental demonstration of one of the most striking phenomena provided by the Dicke model: a quantum phase transition from a normal to a steady-state superradiant phase [2, 3, 4].

Dicke studied an ensemble of two-level atoms coupled identically to one mode of the quantized electromagnetic field. He realized, that the atoms may not be considered as independent individuals when describing their radiative properties and modeled the system of all atoms in a surrounding light field as one single quantum system. The central result of his work was that atoms can absorb photons collectively, resulting in the build-up of strong inter-atomic correlations. These quantum correlations strongly influence the atom-field dynamics and lead to collective spontaneous emission: due to interference between each emitter, the collection of atoms radiates faster than a single atom and produces a short and intense burst of radiation. Thus, the name superradiance was established for this non-equilibrium phenomenon [5].

The experimental demonstration of superradiance was initially prevented by the lack of intense coherent field sources. The maser, providing coherent microwave radiation, was still in its infancy as it was experimentally demonstrated just in 1954 [6, 7]. A first functional laser, a source for coherent visible light, was demonstrated in 1960 [8]. The subsequent overwhelming advances of the laser technology paved the way towards experimentally approaching Dicke's non-equilibrium superradiance. The effect was observed in several laboratories in the 1970's [9, 10, 11, 12, 13, 14]. Intimately related effects have recently been observed with ultracold atoms in free space showing superradiant Rayleigh scattering [15, 16]. This phenomenon can be amplified with the help of an optical ring cavity, giving rise to collective atomic-recoil lasing [17, 18] in close relation to the original effect of superradiance. All of these observations show the intrinsic transient character of Dicke's superradiance by producing short bursts of radiation far from equilibrium.

Beyond non-equilibrium superradiance, the Dicke model exhibits a fascinating phase transition between a normal and a steady-state superradiant phase [19, 20]. Compared to the original superradiance, this phase transition requires many orders of magnitude larger light-matter coupling strength. In this regime, the light-matter coupling gives rise to a polaritonic energy spectrum whose excitations show admixtures of both atomic and photonic character. The Dicke quantum phase transition happens when the energy of one polaritonic eigenmode crosses the ground state. The emerging ground state is of counter intuitive nature: it is energetically favorable to occupy the field mode with photons while having the atomic ensemble coherently sharing excitations.

A level crossing in the ground state at zero temperature upon the change of some control parameter can be considered as a quantum phase transition [21]. Such a phase transition originates from the competition of two energy scales. In the Dicke phase transition one scale is determined by the elementary photonic or atomic excitation energies. This energy is counteracted by the light-matter coupling which can lead to a lowering in energy. The phase transition occurs, once the interaction energy exceeds the elementary excitation energy. Thus, the atom-light coupling strength must exceed the energy scale defined by both the atoms and the photons [19, 20, 22].

Up to now, no experiment provided sufficiently strong light-matter coupling to observe the Dicke phase transition. A possible candidate seemed to be the settings of cavity quantum electrodynamics where a small number of two-level atoms are placed in a cavity which enhances the light-matter coupling and ensures that the atoms couple to only one mode of the electromagnetic field. The traditional systems established in the field range from highly-excited Rydberg atoms coupled to the field of a superconducting microwave resonator [23, 24, 25, 26] to alkali atoms inside an optical cavity [27, 28]. Already more than twenty years ago, the regime of strong coupling, where the light-matter coupling rate for a single atom exceeds all decoherence rates, was realized. The available coupling rates in theses systems are however typically eight orders of magnitude too small to reach the Dicke phase transition. The selected group of systems achieving strong coupling was recently joined by systems involving artificial atoms like quantum dots [29] and superconducting Cooper-pair boxes [30]. A new record in terms of coupling-strength was set last year in the latter type of system, achieving light-matter coupling strengths of up to 10 % of the atomic transition frequency [31, 32]. The integration of many artificial atoms might bring the Dicke transition in those systems within experimental reach within the next years.

A rather different approach to the experimental demonstration of the Dicke phase transition is to decrease the energy scales of the atoms and photons while keeping the coupling strength large. A theoretical proposal from 2007 by Dimer et al. followed this strategy by considering an ensemble of alkali atoms in an optical ring cavity [33]. Two long-lived hyperfine ground states of the atoms are coupled via balanced two-photon Raman transitions. It was shown that the Hamiltonian description of the system reduces to the Dicke model with strongly reduced cavity-mode frequency and atomic transition energy. For realistic experimental conditions this seemed to bring the Dicke phase transition within experimental reach. However, due to the technological complexity of the scheme, it has not been pursued.

In this work, we report on the first experimental realization of the Dicke quantum phase transition. We realize an open system formed by a Bose–Einstein condensate (BEC) coupled to an optical Fabry-Pérot cavity [2] which is driven by a laser field transverse to the cavity axis. We use momentum states rather then hyperfine states and achieve a reduction of the atomic energy scale by three orders of magnitude compared to Dimers proposal [33].

Indeed, Helmut Ritsch and Peter Domokos studied dynamical light forces on atoms inside a cavity and predicted a quantum phase transition towards a self-organized phase of a BEC inside a cavity which is driven by a pump laser transverse to the cavity axis [34]. A related classical version of the self-organization phase transition [35] had already been demonstrated with thermal atoms in the group of Vladan Vuletić [36]. Experimentally, also other groups have succeeded in trapping ensembles of ultracold atoms in optical cavities [37, 38, 39, 40, 41, 42, 43] but none of them have studied the BEC self-organization quantum phase transition.

Considering the quantum motion of a BEC inside a cavity gives rise to qualitative new physics. The narrow momentum distribution of the BEC permits to expand the matter field in two distinct momentum states and allows to show the direct equivalence of the BEC self-organization phase transition and the Dicke quantum phase transition [2, 44]. Conceptually, the resonator induces atom-atom interactions which are mediated by the cavity field, thus resulting in effective interactions of infinite-range. We experimentally observe the atomic density modulation emerging into either of two checkerboard patterns, while atomic phase coherence is preserved at the transition. From the perspective of condensed matter physics, the superradiant phase can thus be regarded as a self-organized supersolid [45, 46, 47, 48].

The Dicke model implemented in our experiment offers a tunable atom-light coupling strength, which is determined by the transverse-pump intensity. This feature enables us to map out the phase boundary of the steady-state superradiant phase in quantitative agreement with the Dicke model. The open character of our system is caused by the finite field lifetime of the experimental cavity setup. Detecting the leaking photons allows us to peek deeply into the atom-cavity dynamics without disturbing the many-body state as it has been shown theoretically that the atomic quantum statistics can be mapped onto the cavity field [49].

Our realization of the Dicke model offers a controlled system with unique detection methods for further investigation of different quantum many-body phenomena. Recently, a new theoretical emphasis has emerged on the general role of entanglement at the Dicke quantum phase transition as it might be a key aspect to understand the dramatic effects occurring in quantum critical systems [50, 51, 52, 53, 54]. Further theoretical investigations of the Dicke model have focused on the onset of quantum chaos [55, 56, 57], geometrical phases [58, 59] and finite-size scaling [60, 61, 62]. These phenomena are now within experimental reach by applying the scheme presented in this thesis.

Outline of this thesis:

- In chapter 2 we start with an introduction of the mathematical framework to describe the dispersive interaction of a Bose-Einstein condensate coupled to a single cavity mode. This framework is applied for describing the phenomenon of self-organization. We present self-organization in terms of intuitive models before proceeding with a mathematical mean-field description. The system is then shown to be equivalent to the Dicke model, which is further explored under the aspect of its phase transition and symmetry breaking.

- Chapter 3 is devoted to give an overview of the experimental apparatus which was used to perform all experiments presented in this thesis. The transverse pump beam, a heterodyne detection scheme used to measure the phase of the cavity field and its electronic read out are described in detail.

- Our experimental observation of the Dicke model phase transition is reported on in chapter 4. The phase boundary of this transition is mapped out in quantitative agreement with the Dicke model.

- By measuring the phase of the cavity output field, we are able to distinguish the two ordered states with reduced symmetry. The origin of the symmetry breaking is investigated in chapter 5 by statistically analyzing the occurrence of both states. We identify a small symmetry-breaking field due to the finite spatial extension of the system and investigate its influence on the symmetry-breaking process.

- Experimental results when coherently pumping the cavity mode directly are presented in chapter 6. The Bose-Einstein condensate is subject to a dynamic optical lattice potential whose depth depends non linearly on the atomic density distribution. We observe optical bistability already below the single photon level and a strong back-action dynamics.

2 Theoretical Framework

The system under investigation throughout this thesis is a Bose-Einstein condensate (BEC) dispersively coupled to a high-finesse optical cavity. In this chapter we will introduce its theoretical description. It is organized as follows: section 2.1 derives the basic theoretical formalism starting from the fundamental description of dipole coupling between a BEC and a single quantized cavity mode. The concept of self-organization of atoms in an optical cavity driven by a transverse laser is presented in terms of intuitive models in section 2.2. We proceed by analyzing self-organization in a mean-field description and show fundamental aspects of the phase transition in section 2.3. After mapping the equations to the Dicke model in section 2.4, we apply concepts, which were discussed in the literature covering the Dicke model, to gain more insight to the process. The chapter concludes with a discussion on second-order phase transitions and the symmetry-breaking process in section 2.5.

2.1. Atoms in an Optical Cavity

The goal in this section is to derive an effective Hamiltonian which is applicable to describe a BEC coupled to a high-finesse optical cavity. This forms the common basis for all collective phenomena discussed throughout this thesis. After describing a single atom coupled to one cavity mode, we apply the rotating-wave approximation to arrive at the Jaynes-Cummings model [63]. We will take atomic motion into account and eliminate the atomic excited state.

2.1.1. A Single Atom

Let's consider a two-level atom at a fixed position in an optical Fabry-Pérot cavity. The Hamiltonian of the system consists of three terms

$$\hat{\mathcal{H}} = \hat{\mathcal{H}}_{\mathrm{a}} + \hat{\mathcal{H}}_{\mathrm{c}} + \hat{\mathcal{H}}_{\mathrm{int}},$$

where $\hat{\mathcal{H}}_{\mathrm{a}}$ describes the atomic subsystem, $\hat{\mathcal{H}}_{\mathrm{c}}$ describes the cavity subsystem and $\hat{\mathcal{H}}_{\mathrm{int}}$ the interaction of the two. The two atomic levels are given by the ground state $|g\rangle$ and the excited state $|e\rangle$ (in Dirac notation). To conveniently express the Hamiltonian $\hat{\mathcal{H}}_{\mathrm{a}}$, we introduce the operators

$$\begin{aligned} \hat{\sigma}_z &= \frac{|e\rangle\langle e| - |g\rangle\langle g|}{2} \\ \hat{\sigma}_+ &= |e\rangle\langle g| \\ \hat{\sigma}_- &= |g\rangle\langle e|. \end{aligned}$$

Physically, the operator $\hat{\sigma}_z$ is interpreted to measure the population difference between the excited and ground state. The transition of an atom from the ground state $|g\rangle$ into the excited state $|e\rangle$ is expressed by $\hat{\sigma}_+ = \hat{\sigma}_-^\dagger$ ($\hat{\sigma}_-$ gives the reverse process). These operators satisfy the spin-1/2 algebra of the Pauli matrices, i.e.,

$$\begin{aligned} [\hat{\sigma}_-, \hat{\sigma}_+] &= -2\hat{\sigma}_z \\ [\hat{\sigma}_-, \hat{\sigma}_z] &= \hat{\sigma}_-. \end{aligned}$$

Given this notation and denoting the energies of a ground and excited state atom with E_g and E_e, respectively, the Hamiltonian $\hat{\mathcal{H}}_\mathrm{a}$ is written as

$$\hat{\mathcal{H}}_\mathrm{a} = E_\mathrm{g}|g\rangle\langle g| + E_\mathrm{e}|e\rangle\langle e| \underset{E_\mathrm{g}\equiv 0}{=} E_\mathrm{e}\hat{\sigma}_+\hat{\sigma}_- \equiv \hbar\omega_\mathrm{a}\hat{\sigma}_+\hat{\sigma}_-.$$

The ground state energy E_g is set to zero and the excited state energy E_e is expressed by the atomic transition frequency ω_a. This shift in energy does not influence the system dynamics.

The geometry of a Fabry-Pérot cavity defines its mode function $\mathcal{E}(\boldsymbol{r})$ with a maximum field strength in the presence of a single photon at frequency ω_c given by $\mathcal{E}_\mathrm{max} = \sqrt{\hbar\omega_\mathrm{c}/2\epsilon_0 V}$. Here, we have used the cavity mode volume $V = \int \left|\frac{\mathcal{E}(\boldsymbol{r})}{\mathcal{E}_\mathrm{max}}\right|^2 \mathrm{d}\boldsymbol{r}$ and the electric permittivity of vacuum ϵ_0. We describe the electromagnetic field in the second quantized formalism employing photon creation and annihilation operators $\hat{a}^\dagger$ and $\hat{a}$ (obeying $\left[\hat{a}, \hat{a}^\dagger\right] = 1$) [64]. In this notation the Hamiltonian $\hat{\mathcal{H}}_\mathrm{c}$, neglecting the zero point energy term $\hbar\omega_\mathrm{c}/2$, reduces to

$$\hat{\mathcal{H}}_\mathrm{c} = \hbar\omega_\mathrm{c}\hat{a}^\dagger\hat{a}.$$

The remaining term $\hat{\mathcal{H}}_\mathrm{int}$ describes the interaction between the atom and the light field. One assumes that the electric field is uniform across the extension of the point-like atom and the interaction can thus be described in the dipole approximation [65]. An electron with charge $-e$ at a relative position with respect to the nucleus $\hat{r}$ creates an electric dipole moment $\hat{d} = -e \cdot \hat{r}$ that couples to the electric field $\hat{E}$ at the position of the atom $\boldsymbol{r}$. Formally, the Hamiltonian describing this process is given by

$$\hat{\mathcal{H}}_\mathrm{int} = \hat{d} \cdot \hat{E}.$$

Rewriting the dipole moment $\hat{d}$ in terms of the transition operators $\hat{\sigma}_+$ and $\hat{\sigma}_-$ yields

$$\begin{aligned} \hat{d} = -e \cdot \hat{r} &= -\sum_{i,j\in\{e,g\}} e \cdot |i\rangle\langle i|\hat{r}|j\rangle\langle j| \underset{\mathcal{D}_{i,j}\equiv e\cdot\langle i|\hat{r}|j\rangle}{=} -\sum_{i,j} \mathcal{D}_{i,j}|i\rangle\langle j| \\ &= -\mathcal{D}_{e,g}\hat{\sigma}_+ - \mathcal{D}_{g,e}\hat{\sigma}_- \underset{\mathcal{D}=\mathcal{D}_{e,g}=\mathcal{D}_{g,e}}{=} -\mathcal{D}\left(\hat{\sigma}_+ + \hat{\sigma}_-\right), \end{aligned}$$

where the electric-dipole transition matrix elements $\mathcal{D}_{i,j}$ $(i,j \in \{e,g\})$ was introduced. Without loss of generality, the point-like atom is assumed to be at a position of maximum electric-field strength where the field operator is written as $\hat{E} = \mathcal{E}_\mathrm{max}(\hat{a} + \hat{a}^\dagger)$. To conform with literature, we further introduce the single-atom coupling strength by $g_0 = -\mathcal{D}\mathcal{E}_\mathrm{max}/\hbar$.

We can now write the complete Hamiltonian for the combined system

$$\begin{aligned} \hat{\mathcal{H}} &= \hat{\mathcal{H}}_\mathrm{a} + \hat{\mathcal{H}}_\mathrm{c} + \hat{\mathcal{H}}_\mathrm{int} \\ &= \hbar\omega_\mathrm{a}\hat{\sigma}_+\hat{\sigma}_- + \hbar\omega_\mathrm{c}\hat{a}^\dagger\hat{a} + \hbar g_0\left(\hat{\sigma}_+ + \hat{\sigma}_-\right)(\hat{a} + \hat{a}^\dagger). \end{aligned} \tag{2.1}$$

2.1.2. The Jaynes-Cummings Model

The Hamiltonian (2.1) includes an interaction part consisting of four terms which are commonly grouped into "co-rotating" terms ($\hat{\sigma}_+\hat{a}$ and $\hat{\sigma}_-\hat{a}^\dagger$) and "counter-rotating" terms ($\hat{\sigma}_+\hat{a}^\dagger$ and $\hat{\sigma}_-\hat{a}$). We show, that the latter terms can be neglected in the limit of moderate coupling strength $g_0 \ll \omega_\mathrm{a}, \omega_\mathrm{c}$. The resulting Hamiltonian, in contrast to (2.1), is analytically solvable and known in literature as Jaynes-Cummings Hamiltonian [63].

The counter-rotating terms are eliminated in the interaction picture. The transformed Hamiltonian reads

$$\begin{aligned}\hat{\mathcal{H}}^* = \hbar g_0 \Big[& \hat{\sigma}_-\hat{a}^\dagger e^{-i(\omega_\mathrm{a}-\omega_\mathrm{c})t} & + & \quad \hat{\sigma}_+\hat{a} e^{i(\omega_\mathrm{a}-\omega_\mathrm{c})t} \\ & \hat{\sigma}_+\hat{a}^\dagger e^{i(\omega_\mathrm{a}+\omega_\mathrm{c})t} & + & \quad \hat{\sigma}_-\hat{a} e^{-i(\omega_\mathrm{a}+\omega_\mathrm{c})t} \Big] .\end{aligned}$$

The technical details of the transformation are presented in appendix A. Our experiments are performed in the optical regime and the cavity frequency ω_c is chosen close to the atomic transition frequency ω_a, i.e., $|\omega_\mathrm{c} - \omega_\mathrm{a}| \ll \omega_\mathrm{c} + \omega_\mathrm{a}$. The terms oscillating at a frequency $\omega_\mathrm{a} + \omega_\mathrm{c}$ (in our experiment $\approx 2\pi \cdot 10^{14}\,\mathrm{Hz}$) will average to zero on the relevant timescale given by g_0 (in our experiment $\approx 2\pi \cdot 10^7\,\mathrm{Hz}$). Terms oscillating at a frequency $\omega_\mathrm{a} - \omega_\mathrm{c}$ on the other hand remain relevant. Neglecting the fast oscillating parts and transforming the Hamiltonian back into the Schrödinger picture yields the Jaynes-Cummings model

$$\hat{\mathcal{H}} = \hbar\omega_\mathrm{c}\hat{a}^\dagger\hat{a} + \hbar\omega_\mathrm{a}\hat{\sigma}_+\hat{\sigma}_- + \hbar g_0 \left(\hat{\sigma}_+\hat{a} + \hat{\sigma}_-\hat{a}^\dagger \right) . \tag{2.2}$$

2.1.3. Atomic Motion

In the previous section, the atom was assumed to be at a fixed position with respect to the cavity field mode. This assumption is now dropped and the atom is free to move in an external trapping potential. Additionally, the system is driven by two different pumping lasers. The cavity is subject to a driving field with frequency ω_p and amplitude Ω_c through one of the cavity mirrors and the atomic subsystem is also driven by a standing-wave pump field transverse to the cavity axis with amplitude Ω_p and frequency ω_p (see figure 2.1). The following section closely follows reference [66].

The Jaynes-Cummings model (2.2) is extended to take the atomic motional degrees of freedom into account. Quite generally, we have to add the kinetic energy of an atom of mass m and momentum $\hat{p}$. The atom is further subject to a trapping potential $V(\boldsymbol{r})$, that is different if the atom is in the ground or excited state (thus labeling the potential with e/g). The Hamiltonian description is accordingly extended by the terms

$$\frac{\hat{p}^2}{2m} + V_\mathrm{e}(\boldsymbol{r})\hat{\sigma}_+\hat{\sigma}_- + V_\mathrm{g}(\boldsymbol{r})\hat{\sigma}_-\hat{\sigma}_+ .$$

The transverse pump field is a standing-wave laser field with frequency ω_p and is described by a spatially-varying classical Rabi frequency $h(\boldsymbol{r}) = \Omega_\mathrm{p} h_\mathrm{t}(\boldsymbol{r})$ with mode profile $h_\mathrm{t}(\boldsymbol{r})$ and maximum Rabi frequency Ω_p. Using the dipole approximation and the rotating-wave approximation we include this driving field in the Hamiltonian description by

$$\hbar h(\boldsymbol{r}) \left(\hat{\sigma}_+ e^{i\omega_\mathrm{p}t} + \hat{\sigma}_- e^{-i\omega_\mathrm{p}t} \right) .$$

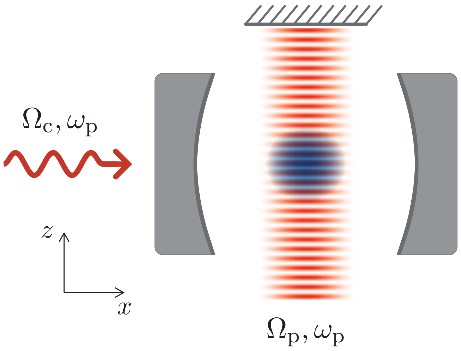
$\Omega_\mathrm{c}, \omega_\mathrm{p}$
z
x
$\Omega_\mathrm{p}, \omega_\mathrm{p}$

FIGURE 2.1.: The general system considered in the present thesis. Atoms are trapped inside an optical resonator and are free to move. The cavity is subject to a driving field (with amplitude Ω_c and frequency ω_p). The atoms themselves are driven by a standing-wave laser field (with amplitude Ω_p and frequency ω_p) from free space.

In a similar fashion, the driving field along the cavity axis with frequency ω_p and strength Ω_c is taken into account by

$$\hbar\Omega_\mathrm{c}\left(\hat{a}e^{i\omega_\mathrm{p}t} + \hat{a}^\dagger e^{-i\omega_\mathrm{p}t}\right).$$

The full extended single-particle Hamiltonian is thus given by

$$\begin{aligned}
\hat{\mathcal{H}}^{(1)} &= \hat{\mathcal{H}}^{(1)}_\mathrm{A} + \hat{\mathcal{H}}^{(1)}_\mathrm{C} + \hat{\mathcal{H}}^{(1)}_\mathrm{Int} \\
\hat{\mathcal{H}}^{(1)}_\mathrm{A} &= \frac{\hat{p}^2}{2m} + V_\mathrm{e}(\boldsymbol{r})\hat{\sigma}_+\hat{\sigma}_- + V_\mathrm{g}(\boldsymbol{r})\hat{\sigma}_-\hat{\sigma}_+ + \hbar\omega_\mathrm{a}\hat{\sigma}_+\hat{\sigma}_- \\
&\quad + \hbar h(\boldsymbol{r})\left(\hat{\sigma}_+ e^{i\omega_\mathrm{p}t} + \hat{\sigma}_- e^{-i\omega_\mathrm{p}t}\right) \\
\hat{\mathcal{H}}^{(1)}_\mathrm{C} &= \hbar\omega_\mathrm{c}\hat{a}^\dagger\hat{a} + \hbar\Omega_\mathrm{c}\left(\hat{a}e^{i\omega_\mathrm{p}t} + \hat{a}^\dagger e^{-i\omega_\mathrm{p}t}\right) \\
\hat{\mathcal{H}}^{(1)}_\mathrm{Int} &= \hbar g(\boldsymbol{r})\left(\hat{\sigma}_+\hat{a} + \hat{\sigma}_-\hat{a}^\dagger\right).
\end{aligned}$$

The explicit time dependency is eliminated by transforming into a frame rotating with the pump frequency ω_p. Since the procedure is very similar to the transformation given in section 2.1.2, the description is kept short here, restricted to presenting the appropriate transformation operator

$$\hat{U}(t) = \exp\left[i\omega_\mathrm{p}t\left(\hat{\sigma}_+\hat{\sigma}_- + \hat{a}^\dagger\hat{a}\right)\right],$$

and the transformed Hamiltonian (while using the same labeling as for the Schrödinger-picture operators)

$$\begin{aligned}
\hat{\mathcal{H}}^{(1)}_\mathrm{A} &= \frac{\hat{p}^2}{2m} + V_\mathrm{e}(\boldsymbol{r})\hat{\sigma}_+\hat{\sigma}_- + V_\mathrm{g}(\boldsymbol{r})\hat{\sigma}_-\hat{\sigma}_+ - \hbar\Delta_\mathrm{a}\hat{\sigma}_+\hat{\sigma}_- \\
&\quad + \hbar h(\boldsymbol{r})\left(\hat{\sigma}_+ + \hat{\sigma}_-\right) \\
\hat{\mathcal{H}}^{(1)}_\mathrm{C} &= -\hbar\Delta_\mathrm{c}\hat{a}^\dagger\hat{a} + \hbar\Omega_\mathrm{c}\left(\hat{a} + \hat{a}^\dagger\right) \\
\hat{\mathcal{H}}^{(1)}_\mathrm{Int} &= +\hbar g(\boldsymbol{r})\left(\hat{\sigma}_+\hat{a} + \hat{\sigma}_-\hat{a}^\dagger\right).
\end{aligned} \tag{2.3}$$

The quantities $\Delta_\mathrm{c} = \omega_\mathrm{p} - \omega_\mathrm{c}$ and $\Delta_\mathrm{a} = \omega_\mathrm{p} - \omega_\mathrm{a}$ describe the detuning of the pump frequency with respect to the bare cavity-resonance and the atomic transition frequency, respectively.

2.1.4. Elimination of the Excited State

After describing a single atom inside a cavity, we will now treat N atoms, that all couple identically to the cavity field which is perfectly realized with a BEC in a cavity [67]. The upcoming description closely follows the procedure presented in reference [66]. For a detailed discussion on the procedure also see reference [68].

Let us introduce the atomic field operators $\hat{\Psi}_{\mathrm{g}}(\boldsymbol{r})$ and $\hat{\Psi}_{\mathrm{e}}(\boldsymbol{r})$ for annihilating an atom at position $\boldsymbol{r}$ in the ground and excited state, respectively. These operators obey bosonic commutation relations

$$\begin{aligned}\left[\hat{\Psi}_i(\boldsymbol{r}), \hat{\Psi}_j^\dagger(\boldsymbol{r}')\right] &= \delta^3(\boldsymbol{r}-\boldsymbol{r}')\delta_{i,j} \\ \left[\hat{\Psi}_i(\boldsymbol{r}), \hat{\Psi}_j(\boldsymbol{r}')\right] &= \left[\hat{\Psi}_i^\dagger(\boldsymbol{r}), \hat{\Psi}_j^\dagger(\boldsymbol{r}')\right] = 0 \qquad i,j \in \{g,e\}.\end{aligned}$$

We now write the derived single particle Hamiltonian (2.3) in the formalism of second quantization

$$\hat{\mathcal{H}} = \hat{\mathcal{H}}_{\mathrm{a}} + \hat{\mathcal{H}}_{\mathrm{c}} + \hat{\mathcal{H}}_{\mathrm{a-a}} + \hat{\mathcal{H}}_{\mathrm{a-c}} + \hat{\mathcal{H}}_{\mathrm{a-p}},$$

where $\hat{\mathcal{H}}_{\mathrm{a}}$ and $\hat{\mathcal{H}}_{\mathrm{c}}$ describe the free evolution of the atomic and cavity subsystem. They are given by

$$\begin{aligned}\hat{\mathcal{H}}_{\mathrm{a}} &= \int d^3\boldsymbol{r}\left[\hat{\Psi}_{\mathrm{g}}^\dagger(\boldsymbol{r})\left(-\frac{\hbar^2}{2m}\nabla^2 + V_{\mathrm{g}}(\boldsymbol{r})\right)\hat{\Psi}_{\mathrm{g}}(\boldsymbol{r})\right. \\ &\qquad \left. + \hat{\Psi}_{\mathrm{e}}^\dagger(\boldsymbol{r})\left(-\frac{\hbar^2}{2m}\nabla^2 - \hbar\Delta_{\mathrm{a}} + V_{\mathrm{e}}(\boldsymbol{r})\right)\hat{\Psi}_{\mathrm{e}}(\boldsymbol{r})\right] \\ \hat{\mathcal{H}}_{\mathrm{c}} &= \hbar\Delta_{\mathrm{c}}\hat{a}^\dagger\hat{a} + \hbar\Omega_{\mathrm{c}}(\hat{a}+\hat{a}^\dagger).\end{aligned}$$

The term $\hat{\mathcal{H}}_{\mathrm{a-a}}$ describes the collisional interaction between two atoms, which is modeled via a short ranged potential characterized by the s-wave scattering length a (see for example reference [69]). This simplification is valid in our experimental regime at ultra-low temperatures, where scattering processes with p-wave or higher character are negligible. Defining $U = 4\pi\hbar^2 a/m$, the Hamiltonian $\hat{\mathcal{H}}_{\mathrm{a-a}}$ is written as

$$\hat{\mathcal{H}}_{\mathrm{a-a}} = \frac{U}{2}\int d^3\boldsymbol{r}\hat{\Psi}_{\mathrm{g}}^\dagger(\boldsymbol{r})\hat{\Psi}_{\mathrm{g}}^\dagger(\boldsymbol{r})\hat{\Psi}_{\mathrm{g}}(\boldsymbol{r})\hat{\Psi}_{\mathrm{g}}(\boldsymbol{r}).$$

The remaining terms $\hat{\mathcal{H}}_{\mathrm{a-c}}$ and $\hat{\mathcal{H}}_{\mathrm{a-p}}$ describe the interaction of atoms with the light fields, where the first describes the cavity field and the latter the transverse-pump field. They read

$$\begin{aligned}\hat{\mathcal{H}}_{\mathrm{a-c}} &= \hbar\int d^3\boldsymbol{r}\left[\hat{\Psi}_{\mathrm{g}}^\dagger(\boldsymbol{r})g(\boldsymbol{r})\hat{a}^\dagger\hat{\Psi}_{\mathrm{e}}(\boldsymbol{r}) + \hat{\Psi}_{\mathrm{e}}^\dagger(\boldsymbol{r})g(\boldsymbol{r})\hat{a}\hat{\Psi}_{\mathrm{g}}(\boldsymbol{r})\right] \\ \hat{\mathcal{H}}_{\mathrm{a-p}} &= \hbar\int d^3\boldsymbol{r}\left[\hat{\Psi}_{\mathrm{g}}^\dagger(\boldsymbol{r})h(\boldsymbol{r})\hat{\Psi}_{\mathrm{e}}(\boldsymbol{r}) + \hat{\Psi}_{\mathrm{e}}^\dagger(\boldsymbol{r})h(\boldsymbol{r})\hat{\Psi}_{\mathrm{g}}(\boldsymbol{r})\right].\end{aligned}$$

With these Hamiltonian at hand, we proceed by calculating the Heisenberg equations for the field operators

$$\begin{aligned}
\frac{\partial\hat{\Psi}_{\mathrm{g}}(\boldsymbol{r})}{\partial t} &= i\left[\frac{\hbar}{2m}\nabla^2-\frac{V_{\mathrm{g}}(\boldsymbol{r})}{\hbar}-\frac{U}{\hbar}\hat{\Psi}_{\mathrm{g}}^{\dagger}(\boldsymbol{r})\hat{\Psi}_{\mathrm{g}}(\boldsymbol{r})\right]\hat{\Psi}_{\mathrm{g}}(\boldsymbol{r}) \\
&\quad+\left[g(\boldsymbol{r})\hat{a}^{\dagger}+h(\boldsymbol{r})\right]\hat{\Psi}_{\mathrm{e}}(\boldsymbol{r}) \qquad (2.4)\\
\frac{\partial\hat{\Psi}_{\mathrm{e}}(\boldsymbol{r})}{\partial t} &= i\left[\frac{\hbar}{2m}\nabla^2-\frac{V_{\mathrm{e}}(\boldsymbol{r})}{\hbar}+\Delta_{\mathrm{a}}\right]\hat{\Psi}_{\mathrm{e}}(\boldsymbol{r}) \\
&\quad-\left[g(\boldsymbol{r})\hat{a}+h(\boldsymbol{r})\right]\hat{\Psi}_{\mathrm{g}}(\boldsymbol{r}) \qquad (2.5)\\
\frac{\partial\hat{a}}{\partial t} &= i\Delta_{\mathrm{c}}\hat{a}+\Omega_{\mathrm{c}}+\int d^3\boldsymbol{r}\; g(\boldsymbol{r})\hat{\Psi}_{\mathrm{g}}^{\dagger}(\boldsymbol{r})\hat{\Psi}_{\mathrm{e}}(\boldsymbol{r}). \qquad (2.6)
\end{aligned}$$

In the present thesis, we have explored the dispersive-coupling regime, which is realized by a large detuning of the light fields with respect to the atomic transition frequency. Typical values of Δ_{a} and Δ_{c} are chosen five orders of magnitude larger then the line width of the atomic states which strongly suppresses any atomic excitation. All atomic internal dynamics, i.e., electronic evolution, are much faster than atomic motion, which allows to discard the kinetic- and potential-energy terms in equation (2.5). We can assume that the atomic excited-state population adiabatically follows atomic motion and accordingly set equation (2.5) to zero, yielding

$$\hat{\Psi}_{\mathrm{e}}(\boldsymbol{r})=-\frac{i}{\Delta_{\mathrm{a}}}\left[h(\boldsymbol{r})+g(\boldsymbol{r})\hat{a}(t)\right]\hat{\Psi}_{\mathrm{g}}(\boldsymbol{r}),$$

which we insert into equation (2.4) and (2.6) to give

$$\begin{aligned}
\frac{\partial\hat{\Psi}_{\mathrm{g}}(\boldsymbol{r})}{\partial t} &= i\left[\frac{\hbar}{2m}\nabla^2-\frac{V_{\mathrm{g}}(\boldsymbol{r})}{\hbar}-\frac{h(\boldsymbol{r})^2}{\Delta_{\mathrm{a}}}-\frac{g^2(\boldsymbol{r})}{\Delta_{\mathrm{a}}}\hat{a}^{\dagger}\hat{a}\right.\\
&\quad\left.-\frac{h(\boldsymbol{r})g(\boldsymbol{r})}{\Delta_{\mathrm{a}}}\left(\hat{a}+\hat{a}^{\dagger}\right)-\frac{U}{\hbar}\hat{\Psi}_{\mathrm{g}}^{\dagger}(\boldsymbol{r})\hat{\Psi}_{\mathrm{g}}(\boldsymbol{r})\right]\hat{\Psi}_{\mathrm{g}}(\boldsymbol{r}) \qquad (2.7)\\
\frac{\partial\hat{a}}{\partial t} &= i\left[\Delta_{\mathrm{c}}-\frac{1}{\Delta_{\mathrm{a}}}\int d^3\boldsymbol{r}\; g^2(\boldsymbol{r})\hat{\Psi}_{\mathrm{g}}^{\dagger}(\boldsymbol{r})\hat{\Psi}_{\mathrm{g}}(\boldsymbol{r})\right]\hat{a}\\
&\quad-\frac{i}{\Delta_{\mathrm{a}}}\int d^3\boldsymbol{r}\; g(\boldsymbol{r})h(\boldsymbol{r})\hat{\Psi}_{\mathrm{g}}^{\dagger}(\boldsymbol{r})\hat{\Psi}_{\mathrm{g}}(\boldsymbol{r})+\Omega_{\mathrm{c}}. \qquad (2.8)
\end{aligned}$$

These equations describe the dynamical behavior of a dispersively-coupled BEC-cavity system. The idea is to find an effective Hamiltonian $\hat{\mathcal{H}}_{\mathrm{eff}}$, that results in the same equations of motion (2.7) and (2.8). One possible Hamiltonian is (omitting the subscript g for readability)

$$\begin{aligned}
\hat{\mathcal{H}}_{\mathrm{eff}} &= \int d^3\boldsymbol{r}\;\hat{\Psi}^{\dagger}(\boldsymbol{r})\left\{-\frac{\hbar^2}{2m}\nabla^2+V(\boldsymbol{r})\right.\\
&\quad\left.+\frac{\hbar}{\Delta_{\mathrm{a}}}\left[h^2(\boldsymbol{r})+g^2(\boldsymbol{r})\hat{a}^{\dagger}\hat{a}+h(\boldsymbol{r})g(\boldsymbol{r})\left(\hat{a}+\hat{a}^{\dagger}\right)\right]\right\}\hat{\Psi}(\boldsymbol{r})\\
&\quad+\frac{U}{2}\int d^3\boldsymbol{r}\;\hat{\Psi}^{\dagger}(\boldsymbol{r})\hat{\Psi}^{\dagger}(\boldsymbol{r})\hat{\Psi}(\boldsymbol{r})\hat{\Psi}(\boldsymbol{r})\\
&\quad-\hbar\Delta_{\mathrm{c}}\hat{a}^{\dagger}\hat{a}-\hbar\Omega_{\mathrm{c}}(\hat{a}+\hat{a}^{\dagger}),
\end{aligned}$$

with a corresponding single particle Hamiltonian

$$\begin{aligned}\hat{\mathcal{H}}_{\text{eff}}^{(1)} &= \frac{\hat{p}^2}{2m} + V(\boldsymbol{r}) + \frac{\hbar h^2(\boldsymbol{r})}{\Delta_{\text{a}}} \\ &+\hbar\left(-\Delta_{\text{c}} + \frac{g^2(\boldsymbol{r})}{\Delta_{\text{a}}}\right)\hat{a}^\dagger\hat{a} \\ &+\hbar\left(-\Omega_{\text{c}} + \frac{h(\boldsymbol{r})g(\boldsymbol{r})}{\Delta_{\text{a}}}\right)(\hat{a}+\hat{a}^\dagger). \qquad (2.9)\end{aligned}$$

This Hamiltonian describes all phenomena discussed in the present thesis. The remainder of this thesis will however be restricted to either of the two case: we will only drive either the cavity ($\Omega_{\text{c}} \neq 0, \Omega_{\text{p}} = 0$) or the atoms ($\Omega_{\text{c}} = 0, \Omega_{\text{p}} \neq 0$), where the majority of this work covers the latter case.

We will now briefly give an interpretation for the individual terms in Hamiltonian (2.9). The part $\frac{\hat{p}^2}{2m} + V(\boldsymbol{r})$ describe the free evolution of a particle in a potential $V(\boldsymbol{r})$ and $-\hbar\Delta_{\text{c}}\hat{a}^\dagger\hat{a} - \hbar\Omega_{\text{c}}(\hat{a}+\hat{a}^\dagger)$ describe an effective cavity mode at frequency Δ_{c} which is subject to pumping with amplitude Ω_{c}. The remaining terms describe lattice potentials for the atoms, starting with $\frac{\hbar h^2(\boldsymbol{r})}{\Delta_{\text{a}}}$ given by the transverse pumping laser and $\frac{\hbar g^2(\boldsymbol{r})\hat{a}^\dagger\hat{a}}{\Delta_{\text{a}}}$ due to the cavity field. Both of these lattice potentials are proportional to the squared of the corresponding mode functions, which in our experimental setting are given by standing waves (i.e., $g(\boldsymbol{r}) = g(x) \propto \cos kx$ and $h(\boldsymbol{r}) = h(z) \propto \cos kz$). The resulting lattice potentials thus show a spatial periodicity of half the optical wavelength. This is in strict contrast to the last remaining expression $\hbar\frac{h(\boldsymbol{r})g(\boldsymbol{r})}{\Delta_{\text{a}}}(\hat{a}+\hat{a}^\dagger)$, which describes a lattice potential due to the interference pattern of the cavity and pump field. Both mode functions $g(\boldsymbol{r})$ and $h(\boldsymbol{r})$ enter linearly implying a λ-periodicity along the cavity and transverse axis.

2.2. Self-Organization of Atoms in a Cavity

The remainder of chapter 2 is devoted to one specific setting of Hamiltonian (2.9). We will consider the atomic ensemble being driven transversely to the cavity axis by a standing-wave laser field while the cavity itself is not subject to a driving field. In this geometry, the atomic ensemble shows the phenomenon of spontaneous self-organization when sufficiently driven from the side [35, 34]. We will introduce this phenomenon here in terms of intuitive pictures to give the reader a physical understanding before proceeding with the mathematical treatment. The explanation is conceptually done with point-like atoms, but the reader should keep in mind that this assumption is strictly speaking not correct for a BEC, where the atoms are delocalized over many µm and one has to adopt a picture of density waves.

2.2.1. Light Scattering by Atoms

Let's consider a single atom inside a cavity which is subject to a free-space transverse laser field. Light from the pump beam can be scattered off-resonantly by an atom. Due to the Purcell effect [70], scattering into the cavity mode will be enhanced and the process is coherent, i.e., the phase of the scattered light field is well defined. This phase value however depends on the position of the atom within the cavity and the pump mode profile.

The scattering process can be seen in terms of radiating atomic dipoles, which are induced in the atoms by the incident pump field. We consider an incident field as a running wave field described by $\propto e^{ikz}$. The relative phase of the atomic dipole oscillation with respect to the position $z = 0$ depends on the atomic position z along the pump axis. This relative phase takes any value between 0 and 2π and the created cavity-field phase will take the same value. Now we consider a standing wave as the incident field, i.e., $\propto \cos(kz)$. This function is real valued which restricts the relative phase of the atomic dipole oscillation to either 0 or π. The resulting cavity field will take the same relative phase and is thus restricted to these two values. The same argument holds along the cavity axis, because the cavity mode in a Fabry-Pérot geometry is also given by a standing wave.

When considering two scattering atoms, their relative position is obviously crucial for the build-up of a cavity field (see figure 2.2). If the separation is half the pump wavelength (or odd multiples of that), the scattered light fields will interfere destructively and the cavity field can not build up (see figure 2.2). If in contrast, the separation is multiples of the pump wavelength, the scattered fields will interfere constructively, enhancing the scattering into the cavity mode and thus increasing the build up of a cavity field.

2.2.2. Scattering by an Ensemble

When replacing two atoms by a large atomic ensemble, we have to consider the distribution of the atoms with respect to the cavity-mode and the pump-mode profile. Two extreme cases are readily seen: (a) the atoms are distributed uniformly, i.e., there is no spatial correlations between individual atoms (see figure 2.3(a)). The light fields scattered at individual atoms will in mean destructively interfere and thereby cancel scattering into the cavity. Intuitively, every atom finds another atom that is separated by odd numbers of half the pump wavelength to cancel its scattered field.

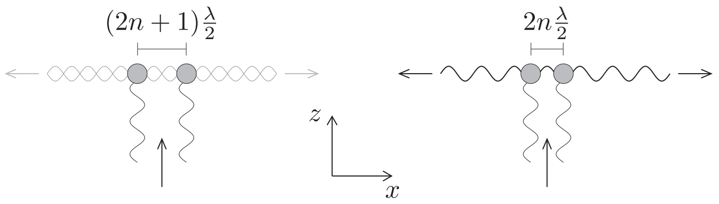

Figure 2.2.: Coherent scattering of light by two atoms. Depending on the spatial separation between the atoms, constructive and destructive interference of the scattered fields can amplify or cancel the scattering.

The other extreme case (b) is a highly ordered state, in which all atoms are separated by multiples of the pump wavelength both along the pump and cavity axis. The interference pattern of the cavity and a standing-wave pump is given by $u(x,z) \propto g(x)h(z) \propto \cos(kx)\cos(kz)$, where x correspond to the cavity axis and the wave vector $k = 2\pi/\lambda$ is expressed by the pump wavelength λ. Positions defined by the condition $u(x,z) = +1$ span a checkerboard lattice with the lattice sites being referred to as “even”. The opposite sites, defined by $u(x,z) = -1$, are referred to as “odd” and the corresponding checkerboard lattice is spatially shifted by half the pump wavelength with respect to the even lattice. If all atoms are localized on either of these two checkerboard lattices, the optical separation between them is always a multiple of the pump wavelength, giving rise enhanced scattering into the cavity due to constructive interference (see figure 2.3(b)).

2.2.3. Buildup of an Interference Potential

After the discussion on the influence of the atomic position on the cavity field in terms of scattering properties, we will now focus on how the cavity light influences the atomic motion.

Throughout the present thesis, we have chosen all involved light fields to oscillate at a frequency that is smaller than the atomic transition frequency. This gives rise to a dipole force on the atoms due to the AC-Stark shift [71, 72], resulting in a potential that shows its minima at the positions of highest electric-field strength. The potential acting on the atoms is given by the interference pattern of the cavity field $\mathcal{E}_\mathrm{c} = \mathcal{A}\cos(kx + [0/\pi])$ with real amplitude $\mathcal{A}$ and the pump field $\mathcal{E}_\mathrm{p} = \mathcal{B}\cos(kz)$ with real amplitude $\mathcal{B}$. The cavity field is thereby created by scattering of light from the pump beam, which gives the additional phase freedom in the cavity field determined by the atoms either at the even or odd site. The resulting interference potential $V(x,z)$ is given by

$$\begin{aligned} V(x,z) &\propto |\mathcal{E}_\mathrm{c} + \mathcal{E}_\mathrm{p}|^2 \\ &= \mathcal{A}^2\cos^2(kx) + \mathcal{B}^2\cos^2(kz) \\ &\quad \pm 2\mathcal{A}\mathcal{B}\cos(kx)\cos(kz). \end{aligned}$$

This potential consists of two terms that are quadratic in either $\cos(kx)$ or $\cos(kz)$ and thus creates minima at both the even and odd site. Atoms subject to this lattice will localize on both checkerboard lattices and, due to destructive interference, not scatter light into the cavity. The additional term in the last row however is different because it shows its minima at either the even or odd sites, depending on the ± sign. If the atoms are on even sites and

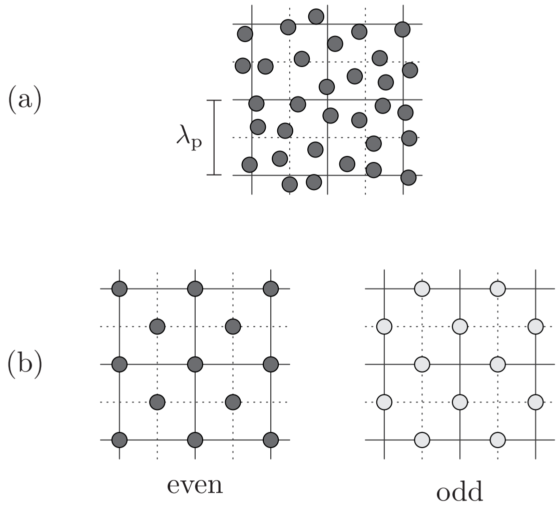

FIGURE 2.3.: The distribution of atoms with respect to the combined mode of the cavity and pump fields. (i) The atoms are distributed equally over all sites suppressing the scattering due to destructive interference. (ii) The atoms are distributed on either the even or odd sub-lattice, thereby maximizing the scattering of pump light into the cavity.

thus create a cavity field with zero phase shift, the last term is added positively, yielding an overall potential with minima at exactly the even sites (and vice versa for the odd case). The restriction of the cavity phase to two values, which yields the ± sign in the last row, is crucial for yielding a potential with its minima at one of two checkerboard lattices.

2.2.4. The Self-Organization Phase Transition

Having discussed the two extreme cases for the atomic position, we will now show how the system enters the ordered phase when starting from the unordered state. Lets consider to start with a cloud of atoms, which are randomly distributed, and we slowly increase the pumping strength beyond a critical value. The atomic cloud is subject to fluctuations (thermal or quantum) which for a short moment leave more atoms on the even checkerboard (the discussion is analogous for more atoms on the odd sites). As there are now more atoms on the even sites, destructive interference between the scattered fields is not perfect and the atomic ensemble will scatter a small light field into the cavity. The interference of cavity and pump field results in a potential with minima at the even sites, therefore attracting even more atoms there. That in turn increases the scattering and amplifies the potential depth which leads to a runaway process localizing all atoms at the even sites. This organization happens at a well defined transverse-pump amplitude as a second-order phase transition [34].

Below the pump-power threshold, this runaway process is counteracted by a characteristic energy scale. The unordered phase is stabilized by thermal fluctuations when considering a thermal atomic ensemble. In the case of a BEC, thermal fluctuations are negligible. Here, the relevant scale is given by kinetic energy of the atomic wave function. Localization costs kinetic energy due to the strong curvature of the wave function, whereas the interference pattern between pump and cavity field yields a gain in potential energy. The transition point is determined by the interplay between these two energy contributions.

2.2.5. Long-Range Interaction

The dynamical nature of the cavity field can be interpreted to induce an effective interaction of infinite range between the atoms. All atoms are subject to a global potential which is created by the cavity-light field interfering with the pump field. It is the position of each individual atom, that determines the scattering rate from the pump into the cavity and thus this global potential. If one atom moves in position, the scattering rate and with that the global potential will change for all other atoms. Each atom thus effectively interacts with each other. We want to mention here that a related effect has been reported on in the group of G. Rempe in 2000 [73]. A cavity mode was driven by a resonant laser instead of driving the atoms from free space. A small number of thermal atoms in the cavity revealed effective long-range interaction, demonstrated in an asymmetric normal-mode splitting.

At the end of the section, we want to recall, that all experiments presented later are performed with a BEC. The picture of localized atoms provides only a qualitatively understanding. The next two sections follow a mathematical approach which correctly take the matter-wave nature of a BEC into account.

2.3. Mean-Field Description

2.3.1. Mean-Field Equations

Atomic self organization is now described with a set of coupled mean-field equations based on the Hamiltonian derived in section 2.1.4. The discussion focuses on one spatial dimension (the cavity axis x) in the infinite system (i.e., no trapping potential, infinite number of atoms but at finite density) to simplify the equations without loosing the main physical content. We will discuss effects due to the finite size of the BEC in section 2.5.

The model follows references [34, 74] and assumes the cavity field to be in a coherent state described by the complex field amplitude α. Entanglement between the atoms and the light field is thus neglected and can not be described. In addition to our previous description, we include a decay of the cavity field with rate κ. Under those assumptions, the set of coupled mean-field equations reads:

$$
\begin{aligned}
i\frac{\partial}{\partial t}\alpha &= \left[-\Delta_\mathrm{c} + N\langle U(x)\rangle - i\kappa\right]\alpha + N\langle \eta(x)\rangle && (2.10)\\
i\frac{\partial}{\partial t}\psi(x,t) &= \left[\frac{p^2}{2m\hbar} + Ng_\mathrm{c}|\psi(x,t)|^2\right.\\
&\quad \left. + |\alpha(t)|^2 U(x) + (\alpha(t)+\alpha(t)^*)\eta(x)\right]\psi(x,t). && (2.11)
\end{aligned}
$$

Equation (2.10) describes the time evolution of the cavity-field amplitude α which is subject to a dynamic pumping term described by $N\langle\eta(x)\rangle$. Here, $\eta(x) = \eta_\mathrm{p}\cos kx$ denotes the spatial-varying effective pump amplitude, $\eta_\mathrm{p} = \Omega_\mathrm{p} g_0/\Delta_\mathrm{A}$ the maximum two-photon Rabi frequency and g_0 the single atom coupling strength (see 2.1.1). The spatial dependency along the cavity axis is due to the cavity-mode profile ($\cos kx$) and the expectation values are defined by $\langle\cdot\rangle = \langle\psi|\cdot|\psi\rangle$ with ψ the atomic wave function normalized to 1. A single atom inside the optical resonator gives rise to a position dependent dispersive shift of the cavity resonance given by $U(x) = U_0\cos^2 kx$. Hence, a single atom at an anti-node of the cavity-mode function gives rise to the maximum shift of $U_0 = g_0^2/\Delta_\mathrm{A}$. The cavity-field decay is properly taken into account by the expression $-i\kappa\alpha$.

The time evolution of the atomic wave function ψ is described by equation (2.11), which is a Gross-Pitaevskii-type equation (GPE) [75] including kinetic energy $\frac{p^2}{2m\hbar}$ and s-wave interaction $Ng_\mathrm{c}|\psi(x,t)|^2$ with the strength given by $g_\mathrm{c} = 4\pi\hbar^2 a/m$. Additionally, two potential terms are present, where the first term describes a potential $|\alpha(t)|^2 U_0\cos^2 kx$ with a strength dependent on the intracavity photon number $|\alpha(t)|^2$. U_0 is thus reinterpreted as the lattice depth created by one intracavity photon. The part $(\alpha(t)+\alpha(t)^*)\eta(x)$ describes a lattice potential with periodicity λ and a strength determined by the external pump amplitude η_p and the cavity field $(\alpha(t)+\alpha(t)^*) = 2\mathrm{Re}(\alpha)$.

It is important to realize, that the light field depends on the atomic density distribution $n(x) = |\psi(x)|^2$ via the expectation values $\langle U(x)\rangle$ and $\langle\eta(x)\rangle$ (see equation (2.10)). On the other hand, the potentials acting on the atoms in equation (2.11) depend on the intracavity field α. This complex interplay renders an analytic solution difficult and we will thus proceed by deriving general properties of the steady-state solution analytically before presenting numerical results.

2.3.2. Steady State

The light field adapts to a changing atomic density within a time proportional to the inverse of the field decay rate κ whereas the atomic motion is limited by the inverse of the recoil frequency $\omega_{\mathrm{r}} = \frac{\hbar k^2}{2m}$ (k is the wave vector of the light field and m the mass of an atom). These scales differ by two orders of magnitude in our experiment and it is thus reasonable to approximate the light field to adapt instantaneously to the atomic density profile. We accordingly set the time derivative in equation (2.10) to zero. The atomic wave function is described by $\psi(x,t) = \psi_0(x)e^{-i\mu t}$ with a normalized spatially-dependent part $\psi_0(x)$ and a time varying term, determined by the chemical potential μ. With those assumptions, equation (2.10) and (2.11) are rewritten as

$$\alpha_0 = \frac{N\eta_{\mathrm{p}}\Theta}{\Delta_{\mathrm{c}} - NU_0B + i\kappa} \tag{2.12}$$

$$\mu\psi_0(x) = \left[\frac{p^2}{2m\hbar} + |\alpha_0|^2 U(x) + (\alpha_0 + \alpha_0^*)\eta(x) + Ng_{\mathrm{c}}|\psi_0(x)|^2\right]\psi_0(x). \tag{2.13}$$

Here we have introduce the order parameter

$$\Theta = \langle\psi|\cos kx|\psi\rangle \qquad (-1 \leq \Theta \leq 1), \tag{2.14}$$

which measures the overlap of the atomic density with the $\cos kx$ mode profile of the cavity. For localized atoms, i.e., the atomic density is a sum of delta distributions, this parameter counts the population imbalance of atoms on the even and odd sites. We will later use Θ as the order parameter for describing the phase transition. In a similar mathematical fashion, we define the bunching parameter $B = \langle\psi|\cos^2 kx|\psi\rangle$ $(0 \leq B \leq 1)$, which measures the density overlap with the square of the cavity mode profile. This quantity gives rise to a dispersive shift of the cavity resonance.

We can explicitly write an effective potential acting on the atomic wave function by inserting equation (2.12) into (2.13). The obtained GPE consists of terms describing kinetic energy and atom-atom interaction as well as a potential of the form

$$V(x) = U_1 \cos kx + U_2 \cos^2 kx. \tag{2.15}$$

The coefficients are given by $U_1 = 2\Theta N I_0\left[\Delta_{\mathrm{c}} - NU_0B\right]$ and $U_2 = \Theta^2 N^2 I_0 U_0$. The expression $I_0 = |\eta_{\mathrm{p}}|^2 / \left(\left[\Delta_{\mathrm{c}} - NU_0B\right]^2 + \kappa^2\right)$ can be interpreted as the maximum scattering rate of a single atom.

2.3.3. Phase Boundary

Self-organization of a BEC is described by the first potential term in equation (2.15). We will now determine the critical pump amplitude η_{cr} for the phase transition where the system's state abruptly changes from a normal to an ordered state.

The analytic expression for the threshold pump amplitude η_{cr} is obtained by performing a linear stability analysis of the equation (2.13) [34]. We start with the trivial steady-state solution below threshold, which corresponds to a constant atomic density and a zero cavity field, i.e., we define $\psi_0 = 1$ and $\alpha_0 = 0$. Only density perturbations proportional to $\cos kx$, i.e., periodic in λ, will couple to the cavity field and we thus write the atomic state as

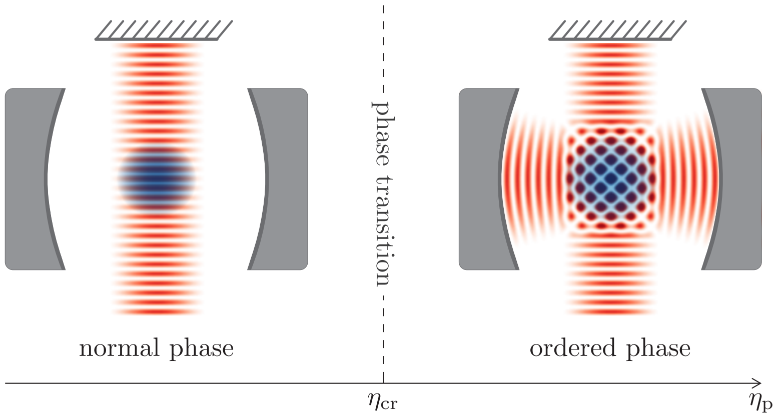

FIGURE 2.4.: Ground state below and above the critical pump amplitude η_{cr}. The normal phase is characterized by no coherent cavity-field and a constant atomic density. A coherent population of the cavity field and a modulated atomic field characterize the ordered phase.

$\psi(x) = \psi_0 + \epsilon \cos kx = 1 + \epsilon \cos kx$. The parameter $\epsilon \ll 1$ characterizes a small perturbation around the constant atomic ground-state density. The light field is further eliminated and we neglect terms of quadratic order in ϵ.

Propagating the atomic state for one time step in imaginary time $i\Delta\tau$ yields (for a brief introduction to imaginary-time propagation see appendix B)

$$\frac{\Delta\psi}{\Delta\tau} = -Ng_{\mathrm{c}} - \epsilon \cos kx \left(\omega_{\mathrm{r}} + N\eta_{\mathrm{p}}^2 \frac{2\Delta_{\mathrm{c}} - NU_0}{(\Delta_{\mathrm{c}} - NU_0/2)^2 + \kappa^2} + 3Ng_{\mathrm{c}} \right).$$

The constant part of the wave function decays with a rate of Ng_{c} whereas the perturbation part decays with a rate depending on the pump amplitude η_{p} $\left(\omega_{\mathrm{r}} = \frac{\hbar k^2}{2m}\right)$. Since we have chosen $\Delta_{\mathrm{c}} < 0$, the decay rate of the perturbation will decrease upon an increase of the pump amplitude. The trial solution remains stable if the perturbation decays faster than the constant term. The condition for the critical pump amplitude is thus given by the equality of the two decay rates. This yields

$$\eta_{\mathrm{cr}} = \frac{1}{\sqrt{N}} \sqrt{\frac{(\Delta_{\mathrm{c}} - NU_0/2)^2 + \kappa^2}{NU_0 - 2\Delta_{\mathrm{c}}}} \sqrt{\omega_{\mathrm{r}} + 2Ng_{\mathrm{c}}}. \tag{2.16}$$

It is crucial to realize that the denominator in the square root has to be positive in order to give a real (and therefore physical) results. Experimentally, we thus choose Δ_{c} and U_0 to be negative and obey the condition $|NU_0/2| < |\Delta_{\mathrm{c}}|$. The self-organization process is otherwise prevented.

2.3.4. Normal and Ordered Phases

We will now qualitatively discuss the steady states of the normal and ordered phase. If the pump amplitude is below the critical value ($\eta_{\mathrm{p}} < \eta_{\mathrm{cr}}$), the ground state of the system is given by the trivial solution of equation (2.12) and (2.13). This corresponds to a constant atomic density $n(x) = |\psi_0|^2 = \mathit{const}$ and no coherent cavity field $|\alpha_0|^2 = 0$ (figure 2.4). The order parameter Θ vanishes for this configuration, therefore rendering the effective potential

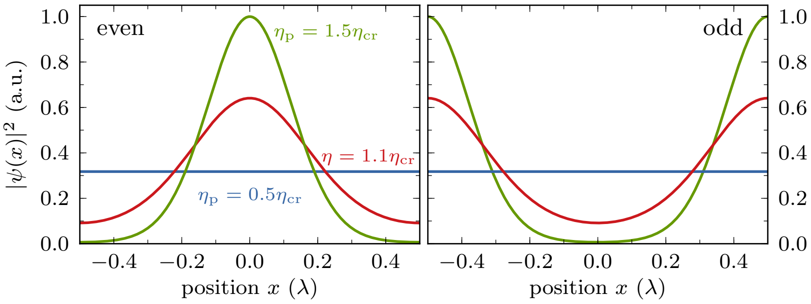

FIGURE 2.5.: Atomic density as a function of position x along the cavity axis for different pump amplitudes η_p. The left and right panel display the even and odd solution respectively. The parameters for the simulation are given in section 2.3.5.

(equation (2.15)) to zero and equation (2.13) reduces to the description of a BEC with s-wave atom-atom interaction.

The ground state of the system dramatically changes when tuning the control parameter η_p beyond its critical value, where two energetically equivalent ground states emerge. Both states show a modulated atomic density with maxima at either of the two checkerboard lattices. The order parameters Θ acquires a macroscopic value with its sign determined by the choice between the even and odd sites. A non-zero order parameter gives rise to a non-zero coherent cavity field, evident from equation (2.12), which oscillates either in phase or with a π phase shift with respect to the pump beam.

The finite value of the cavity decay rate κ induces an additional cavity-field phase shift. However, the light-phase difference between the system organized on the even sites and the system on the odd sites remains independent of κ and always shows the value π. Detecting the relative phase between pump and cavity field can thus be used to distinguish the two self-organized states experimentally.

2.3.5. Numerical Results

The self-consistent ground state solution of equations (2.12) and (2.13) obtained from a numerical simulation is discussed in the following section. We use a split-step technique to propagate a trial wave function in imaginary time to obtain an approximation of the system's ground state. An introduction of the algorithm is given in appendix B.

It is sufficient to consider a computational cell of length λ by applying periodic boundary conditions, since the one-dimensional infinite system without a trapping potential is investigated. The parameters chosen for the simulations are in close accordance to our experimental settings. We typically work with $2 \cdot 10^5$ atoms yielding a density on the order of 10^{14} atoms/cm^3. The line density chosen in the one-dimensional simulations is set to a value of 10^8 atoms/cm, according to our trapping potential. The pump-cavity detuning Δ_c is set to a value of $\Delta_c = -2\pi \cdot 20\,\text{MHz}$. Equation (2.16) shows that weak atom-atom interactions do not alter the phase transition significantly, apart from a small shift of the transition point. We will thus neglect the interaction due to the small scattering length of ^{87}Rb.

Figure 2.5 shows the atomic density $|\psi(x)|^2$ for different values of the pump amplitude. For values below the critical pump strength, the condensate exhibits a flat atomic density

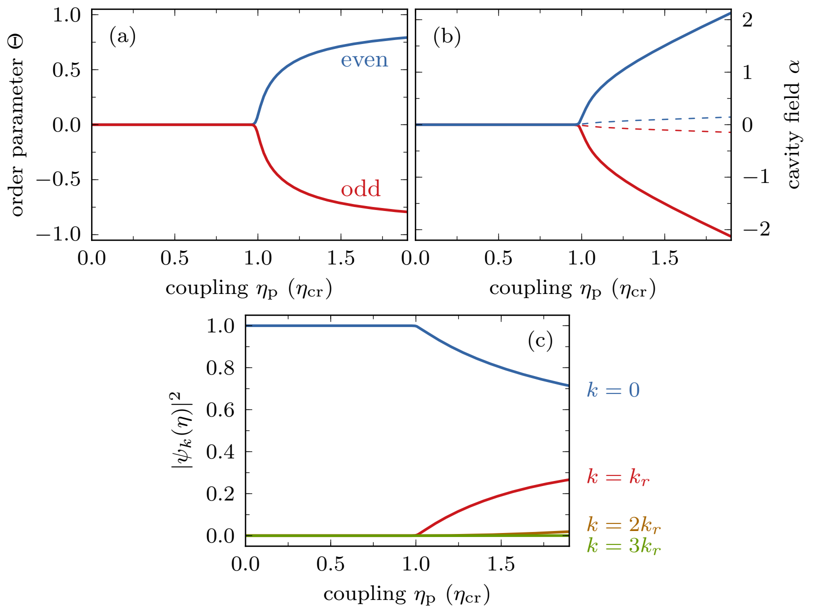

FIGURE 2.6.: Displayed are properties of the ground-state solution as a function of pump amplitude η_p. Shown is (a) the order parameter Θ, (b) the real (full lines) and imaginary part (dashed lines) of the intracavity light field α and (c) a Fourier decomposition of the even solution into different momentum modes with wave vector of $nk_r = n\frac{2\pi}{\lambda}$ $(n = 1, 2, ...)$. The simulation parameters are given in section 2.3.5.

and constant phase over the unit cell (the latter is not shown in the figure but apparent from the raw simulation data). As the pump strength is increased beyond the critical value, the atomic density shows a modulation with periodicity of λ. Further increasing the pump power yields an even stronger modulation of the atomic density, equivalent to stronger localization of the atomic density onto the checkerboard lattice. The two panels of the figure show the two possible ground states, corresponding to the even and odd configuration.

To get further insight into the process of self-organization, the order parameter Θ, as a function of pump strength η_p, is shown in figure 2.6. Below threshold, the trivial ground state exhibits a zero order parameter. At the phase transition point, two degenerate ground states emerge in a pitchfork bifurcation with the even solution yielding a positive branch and the odd solution the negative branch. Kinetic energy counteracts the increase in the order parameter, which results in a slow approach of the extreme values. The second panel in figure 2.6 shows the real and imaginary part of the cavity-field amplitude. The non-zero imaginary part is solely due to cavity decay κ, which becomes apparent by analyzing equation (2.12). The different scales of the real and imaginary part are determined by the pump-cavity detuning Δ_c compared to κ, but the scaling behavior, i.e., linear in the order parameter Θ, is identical for both.

The third panel in the figure shows the absolute square of different Fourier components of the atomic field for the even solution. Below threshold, only the component which is constant in space is populated. As the phase transition is crossed, the population in the mode with a wave function proportional to $\cos kx$ starts to increase. Due to matter-wave interference with the ground state, this results in a modulated density distribution. As the

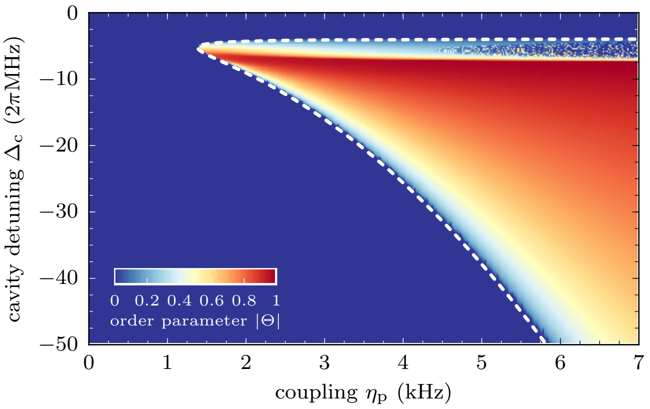

FIGURE 2.7.: Phase diagram of the order parameter as a function of pump-cavity detuning Δ_c and pump amplitude η_p. The white lines shows the phase boundary from equation (2.16). The parameters for the simulation are given in section 2.3.5.

pump strength is further increased and the atomic density gets more and more modulated, other Fourier components are populated, visible in the Fourier decomposition, as the value of higher components $\cos nkx$ with $n = 2, 3, ...$ increases. It is however also apparent, that the population in modes $\cos nkx$ with $n > 1$ is very little for moderate pumping. Hence, the two lowest lying momentum states are dominant at the phase transition and will be used to formulate an effective two-mode description in section 2.4.

Figure 2.7 shows the order parameter as a function of both the pump-cavity detuning Δ_c and the pump amplitude η_p in a two-dimensional color plot. A clear boundary between the normal and ordered phase is apparent which reproduces the analytic result presented in equation (2.16) (dashed curve in the figure). The upper boundary in frequency for self-organization is given by the condition, $\Delta_c - NU_0/2 < 0$, i.e., the pump laser has to be negatively detuned with respect to the dispersively shifted cavity resonance. Below this region, the phase boundary increases like $\sqrt{\Delta_c}$. Accessing the ordered phase for large detuning should be possible due to the moderate scaling of the critical pump amplitude with detuning.

The region defined by $NU_0 < \Delta_c < NU_0/2$ ($-2\pi \cdot 8\,\text{MHz} < \Delta_c < -2\pi \cdot 4\,\text{MHz}$) is predicted to be unstable [76] which is also visible in the simulation by the "noise" in the upper right corner of figure 2.7. This area is dominated by the dispersive-shift term of the cavity, given by the expression NU_0B. The crucial parameter here is the bunching parameter B, as it takes the value $\frac{1}{2}$ for a flat condensate density and can rise up to $+1$, if the atoms are fully localized onto one of the checkerboard lattices. The resulting doubling of the dispersive cavity shift flips the sign of the effective pump-cavity detuning $\Delta_c - NU_0B$ and thus stop the self-organization process. As the atomic density relaxes towards a flat distribution, the sign flips again and starts the process again. This instability has been observed experimentally and will be presented in chapter 4.

Finally, the scaling of the intracavity intensity as a function of atomic density is shown in figure 2.8. The left panel (a) shows results from simulations with a pump amplitude $\eta_p = 1.05\eta_{cr}$, set for each data point independently since η_{cr} depends on both the atomic density and pump-cavity detuning. The light intensity increases almost perfectly linear in atomic density. On the other hand, the right panel (b) shows the simulation for constant

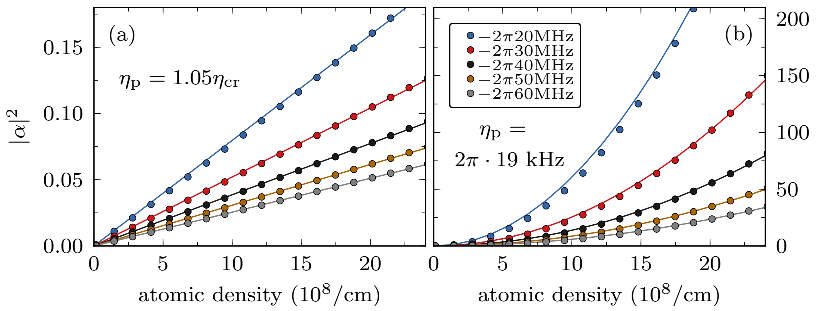

FIGURE 2.8.: Intracavity photon number $|\alpha|^2$ as a function of atomic density and pump-cavity detuning Δ_c. (a) calculated for a pump amplitude $\eta_p = 1.05\eta_{cr}$, where η_{cr} is evaluated for each data point independently. The lines are fits according to $|\alpha|^2 = \epsilon x$. (b) calculated for a value of $\eta_p = 2\pi \cdot 19\,\text{kHz}$ for all data points and the lines are fits according to $|\alpha|^2 = \epsilon x^2$. The color code, representing the pump-cavity detuning Δ_c, is the same for both panels.

pump amplitude of $\eta_p = 2\pi \cdot 19\,\text{kHz}$ for all data points, resulting in a quadratic increase of the intracavity photon number. This rather unusual scaling behavior constitutes a strong hint towards a connection with the superradiant phase of the Dicke model as the light field is predicted to scale identically.

2.4. The Dicke Model

We have seen that only two atomic momentum modes are populated in the vicinity of the transition point (see figure 2.6). We will thus restrict our discussion to two atomic momentum states and show that atomic self-organization corresponds to the Dicke quantum phase transition. We will then discuss the system further, using the Dicke model framework.

2.4.1. Coupling of Momentum States

The ground state of an atom is characterized by zero momentum $|p_x, p_z\rangle = |0, 0\rangle$ along the pump (z) and cavity axis (x) which is a good approximation for a BEC, where the momentum-distribution is ultra narrow around zero. The scattering of photons between the pump and cavity field will couple this ground state to a superposition state $|\pm\hbar k, \pm\hbar k\rangle \equiv \sum_{\mu,\nu=\pm 1} |\mu\hbar k, \nu\hbar k\rangle/2$, denoted as the excited state in the following. The constituents of this superposition each have one photon momentum $\hbar k$ along the cavity and pump axis, resulting in an energy lifted by twice the recoil energy ($E_\mathrm{r} = \hbar^2 k^2/2m$) with respect to the ground state (see figure 2.9).

Let's consider an atom in its ground-state that scatters a photon from the pump beam into the cavity mode. We can think of the process as the virtual absorption of a photon from the pump beam (see figure 2.9(b)). The atom therefore gains one photon momentum along the pump axis, but due to the standing-wave nature of the pump field, the sign of the momentum is not determined yielding a superposition of both. The subsequent emission of a photon into the cavity mode yields a momentum "kick" along the cavity axis, which once again results in a superposition of both signs due to the standing-wave nature of the cavity mode. An atom is thus transferred from the ground state $|0, 0\rangle$ into the excited state $|\pm\hbar k, \pm\hbar k\rangle$. A different point of view is given in figure 2.9(a), where the process is interpreted as a two-photon Raman transition including the pump and cavity field. The electronic intermediate level is however not populated during the transition due to the large value of Δ_a. The figure also shows the reversed processes, i.e., first virtual absorption of a cavity photon and subsequent emission into the pump beam (figure 2.9 dashed lines). Both paths can thus transfer an atom from the ground state into the excited state (and vice versa). The resulting four coupling processes of the two momentum states describe the phenomenon of self-organization extremely well. The next section will restrict the atomic Hilbert space to the discussed momentum modes to derive an effective Hamiltonian description, which is the Dicke model.

2.4.2. Mapping to the Dicke Model

The single particle Hamiltonian (2.9) derived in section 2.1 forms the starting point of the following discussion. We neglect the external trapping potential and the potential arising from the standing-wave pump field because both do not alter the physical process significantly, but hamper the analytical treatment. The presented transformation has been published for reducing the system to two spatial dimensions [2] and to one spatial dimension [44]. We will proceed with in two dimensions, where the Hamiltonian reads

$$\hat{\mathcal{H}}^{(1)} = \frac{\hat{\mathbf{p}}^2}{2m} - \hbar\left[\Delta_\mathrm{c} - \frac{g^2(x)}{\Delta_\mathrm{a}}\right]\hat{a}^\dagger\hat{a} + \frac{\hbar g(x)\eta(z)}{\Delta_\mathrm{a}}\left(\hat{a} + \hat{a}^\dagger\right).$$

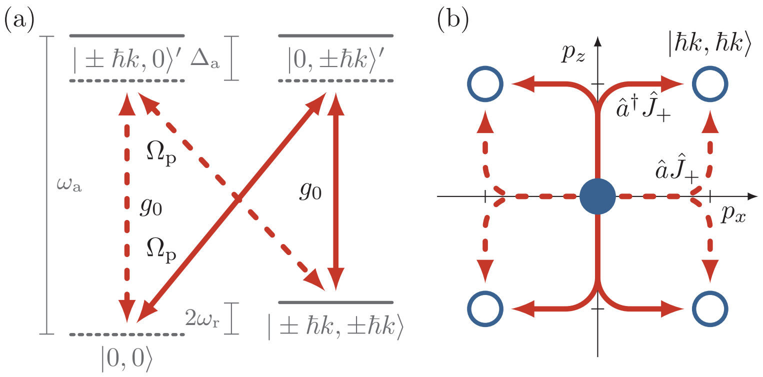

FIGURE 2.9.: Basis for mapping atomic self-organization onto the Dicke phase transition. (a) energy diagram showing the relevant two-photon transitions from the atomic ground state $|0,0\rangle$ to the excited momentum state $|\pm\hbar k,\pm\hbar k\rangle$. (b) the possible excitation paths shown in a momentum diagram.

The size of the BEC in the experiment is small compared to the waist radius of both the cavity mode and the transverse pump beam. We can therefore neglect the transverse Gaussian envelope function of both and write the cavity mode function as $g(x)=\cos(kx)$ and the pump mode function as $\eta(z)=\eta_{\mathrm{p}}\cos(kz)$ with a maximum single-atom single-photon coupling strength g_0 and a maximum two-photon Rabi-frequency of $\eta_{\mathrm{p}}=\frac{\Omega_{\mathrm{p}}g_0}{\Delta_{\mathrm{a}}}$. By further introducing the momentum operators along the cavity axis and pump axis as $\hat{p}_x$ and $\hat{p}_z$, we can rewrite the Hamiltonian as

$$\begin{aligned}\hat{\mathcal{H}}^{(1)} &= \frac{\hat{p}_x^2+\hat{p}_z^2}{2m}\\ &+\hbar\eta_{\mathrm{p}}\left(\hat{a}^\dagger+\hat{a}\right)\cos(kx)\cos(kz)\\ &-\hbar\left(\Delta_{\mathrm{c}}-U_0\cos^2(kx)\right)\hat{a}^\dagger\hat{a}.\end{aligned}\tag{2.17}$$

Similar to section 2.1.4, the many-body Hamiltonian is written in the formalism of second quantization neglecting atom-atom interaction

$$\begin{aligned}\hat{\mathcal{H}} &= -\Delta_{\mathrm{c}}\hbar\hat{a}^\dagger\hat{a}+\iint_0^\lambda\hat{\Psi}^\dagger(x,z)\left[\frac{\hat{p}_x^2+\hat{p}_z^2}{2m}\right.\\ &+\hbar\eta_{\mathrm{p}}\left(\hat{a}^\dagger+\hat{a}\right)\cos(kx)\cos(kz)\\ &\left.+\hbar U_0\cos^2(kx)\hat{a}^\dagger\hat{a}\right]\hat{\Psi}(x,z)\mathrm{d}x\mathrm{d}z.\end{aligned}\tag{2.18}$$

The atomic ground state ψ_0 is coupled to the excited state ψ_1 via the processes discussed in the previous section. Explicitly, the considered states are written as

$$\begin{aligned}\psi_0 &= 1\\ \psi_1 &= 2\cos kx\cos kz.\end{aligned}$$

The ground state shows a spatially constant atomic density $|\psi_0|^2$ while the excited state shows a modulated density $|\psi_1|^2$ with a periodicity of $\lambda/2$. Matter-wave interference between the ground and excited state leads to the modulation according to a checkerboard patter, with a periodicity of λ along both axis. Thus, the ordered configuration is given by a superposition state of both basis states.

We expand the atomic field operator in this basis, $\hat{\Psi} = \psi_0 \hat{c}_0 + \psi_1 \hat{c}_1$, and insert it into the many-body Hamiltonian (2.18). The kinetic energy term is then evaluated to be

$$\iint_0^\lambda \hat{\Psi}^\dagger \left[\frac{\hat{p}_x^2 + \hat{p}_z^2}{2m}\right] \hat{\Psi} \mathrm{d}x \mathrm{d}z = \hat{c}_1^\dagger \hat{c}_1 \frac{\hbar^2 k^2}{m},$$

reflecting that the kinetic energy of the ground state vanishes. Cross-terms involving $\hat{c}_0$ and $\hat{c}_1$ vanish due to the orthogonality of ψ_0 and ψ_1. The only non-vanishing expression is the kinetic energy of the excited state given by twice the recoil energy $E_\mathrm{r} = \hbar^2 k^2/(2m)$. The cavity potential term is evaluated to

$$\begin{aligned} \iint_0^\lambda \hat{\Psi}^\dagger \left[\hbar U_0 \cos^2(kx) \hat{a}^\dagger \hat{a}\right] \hat{\Psi} \mathrm{d}x \mathrm{d}z &= \hat{c}_0^\dagger \hat{c}_0 \; \hat{a}^\dagger \hat{a} \; \hbar \frac{U_0}{2} \\ &\quad + \hat{c}_1^\dagger \hat{c}_1 \; \hat{a}^\dagger \hat{a} \; \hbar \frac{3U_0}{4}. \end{aligned}$$

The remaining expression couples the ground state ψ_0 with the excited state ψ_1. Explicitly, the interaction reads

$$\begin{aligned} \iint_0^\lambda \hat{\Psi}^\dagger \left[\hbar \eta_\mathrm{p} \left(\hat{a}^\dagger + \hat{a}\right) \cos(kx) \cos(kz)\right] \hat{\Psi} \mathrm{d}x \mathrm{d}z &= \hat{c}_0^\dagger \hat{c}_1 \left(\hat{a}^\dagger + \hat{a}\right) \hbar \eta_\mathrm{p} \frac{1}{2} \\ &\quad + \hat{c}_1^\dagger \hat{c}_0 \left(\hat{a}^\dagger + \hat{a}\right) \hbar \eta_\mathrm{p} \frac{1}{2}. \end{aligned}$$

The resulting Hamiltonian with all computed terms is given by

$$\begin{aligned} \hat{\mathcal{H}} &= \frac{\hbar^2 k^2}{m} \hat{c}_1^\dagger \hat{c}_1 + \hbar \frac{U_0}{2} \hat{c}_0^\dagger \hat{c}_0 \; \hat{a}^\dagger \hat{a} + \hbar \frac{3U_0}{4} \hat{c}_1^\dagger \hat{c}_1 \; \hat{a}^\dagger \hat{a} \\ &\quad + \frac{\hbar \eta_\mathrm{p}}{2} \left(\hat{c}_0^\dagger \hat{c}_1 + \hat{c}_1^\dagger \hat{c}_0\right) \left(\hat{a}^\dagger + \hat{a}\right) - \hbar \Delta_\mathrm{c} \hat{a}^\dagger \hat{a}. \end{aligned}$$

The number of atoms is assumed to be conserved by all processes, i.e., $N = \hat{c}_1^\dagger \hat{c}_1 + \hat{c}_0^\dagger \hat{c}_0$. Following section 2.1.1, we introduce collective spin operators

$$\begin{aligned} \hat{J}_- &= \hat{c}_0^\dagger \hat{c}_1 \\ \hat{J}_+ &= \hat{c}_1^\dagger \hat{c}_0 \\ \hat{J}_z &= \left(\hat{c}_1^\dagger \hat{c}_1 - \hat{c}_0^\dagger \hat{c}_0\right)/2, \end{aligned}$$

which obey the angular-momentum commutation relations. The many-body Hamiltonian is then rewritten with those operators to take the form

$$\begin{aligned} \hat{\mathcal{H}}/\hbar &= \omega_0 \hat{J}_z + \omega \hat{a}^\dagger \hat{a} + \frac{\lambda}{\sqrt{N}} \left(\hat{J}_+ + \hat{J}_-\right) \left(\hat{a}^\dagger + \hat{a}\right) \\ &\quad + \frac{N \omega_0}{2} + \frac{U_0}{4} \left(\hat{J}_z + \frac{N}{2}\right) \hat{a}^\dagger \hat{a}. \end{aligned} \tag{2.19}$$

The first line of this expression is exactly the Dicke Hamiltonian, that describes N two-level atoms with transition frequency ω_0 coupled to one cavity mode with frequency ω and a coupling constant of λ. In our realization of this Hamiltonian, the transition frequency of the atoms is given by the energy difference between the two involved momentum states, i.e., $\omega_0 = \hbar^2 k^2/m$. The effective frequency of the radiation field is given by $\omega = -\Delta_\mathrm{c} + NU_0/2$. A convenient feature of our implementation is the ability to tune the atom-light coupling strength $\lambda = \eta_\mathrm{p}\sqrt{N}/2$ via the transverse pump amplitude.

The first expression in the second line of Hamiltonian (2.19) is constant and is therefore omitted. The remaining term is small as long as the population of the excited state is small. This condition is met anyways, since otherwise coupling to higher momentum states can not be neglected, violating the basic assumption of our two-mode momentum expansion. We can therefore omit the full last line of Hamiltonian (2.19) to describe the phase transition.

2.4.3. The Dicke Phase Transition

It was shown in 1973 that the Dicke model in the thermodynamic limit exhibits a second order phase transition from a normal to a steady-state superradiant phase [19, 20]. Taking into account the counter-rotating terms (as in our realization), it was pointed out by Carmichael et al. [22] that the critical coupling strength is given by

$$\lambda_\mathrm{c} = \sqrt{\frac{\omega\omega_0}{4\tanh\beta\frac{\hbar\omega_0}{2}}} \qquad \beta = \frac{1}{k_\mathrm{b}T}.$$

The corresponding phase diagram is displayed in figure 2.10. The critical coupling strength λ_c increases in temperature whereas for low temperatures, the slope diverges and the value approaches the zero-temperature limit given by $\lambda_\mathrm{c} = \sqrt{\omega\omega_0}/2$. Since our experiments are carried out with a BEC, the atomic two-level system is not thermally populated and we thus effectively realize this zero-temperature limit of the Dicke model.

Our realization relies on a high-finesse optical cavity. Even though built with the best commercially available mirrors, a finite cavity-field decay rate κ remains, which is caused by the finite transmission of the cavity mirrors and loss due to manufacturing imperfections. This can be taken into account giving rise to a correction of the critical coupling strength [33]. The corrected expression is given by

$$\lambda_\mathrm{c} = \frac{1}{2}\sqrt{\left(\frac{\omega_0}{\omega}\right)(\omega^2+\kappa^2)}\left(\xrightarrow[\frac{\kappa}{\omega}\to 0]{}\frac{\sqrt{\omega\omega_0}}{2}\right).$$

In the normal phase, the ground state of the original Dicke system is a state with no coherent cavity field and all atoms in their electronic ground state. In our effective Dicke system, this corresponds to all atoms in the zero momentum state (i.e., a flat atomic density) and no coherent occupation of the cavity field. Beyond the phase transition however, the new ground state in the original Dicke setting is a state with non-vanishing cavity field and collective atomic excitation. In our realization, this excited state is characterized by a BEC with modulated density of periodicity λ and a non-vanishing coherent cavity field.

It should be noted that our implementation constitutes an open-system version of the Dicke transition. There is a constant energy loss rate, mainly due to the cavity-field loss rate, which is compensated by a flux of energy from the pump beam. The system is thus to be regarded in a non-equilibrium state (see for example [77, 78, 79]). This however does not prevent an open system to reach a steady state, where all properties (or state variables)

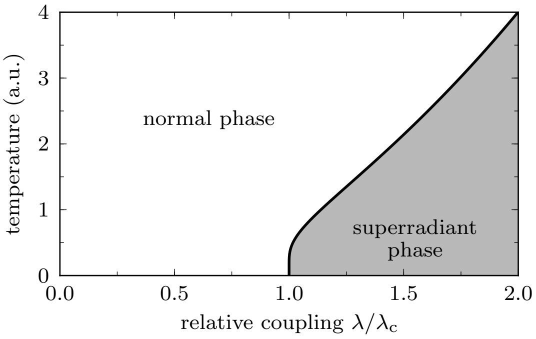

FIGURE 2.10.: Finite temperature phase diagram of the Dicke model. Displayed is the phase boundary between the normal and the superradiant phase. Our realization using a BEC corresponds to the zero-temperature limit.

are constant in time [80]. An intriguing feature of our system is the ability to monitor light leaking out of the cavity. This gives us the possibility to infer about the systems current state in real time as the cavity field is an intrinsic part of the system. Further effects of the openness of the system regarding critical exponents and measurement-induced backaction is subject to ongoing theoretical [81, 82] and experimental work.

2.4.4. Numerical Diagonalization

We will proceed by analyzing atomic self-organization within the framework of the Dicke model. Two techniques are employed in the following: exact numerical diagonalization of the finite atom-number Dicke Hamiltonian and analytic results in the thermodynamic limit (i.e., $N \to \infty$). The technical details for the numerically diagonalization are described in this section. The actual results are shown in the following section alongside the analytic results in the thermodynamic limit. We find good agreement of both methods.

A basis for describing N two-level atoms is given by the product states

$$|\mu_1\rangle_1 |\mu_2\rangle_2 \dots |\mu_\mathrm{N}\rangle_\mathrm{N},$$

where $|.\rangle_\mathrm{i}$ describes the state of the i-th atom and μ_i takes either g or e, denoting ground and excited state. This basis consists of 2^N states. A different basis that is better adapted to the problem is given by the so called Dicke states [83]

$$|j, m\rangle \quad m = -j, -j+1, \dots, j-1, j$$

which are eigenstates of the collective spin operators $\hat{J}^2 = \hat{J}_x^2 + \hat{J}_y^2 + \hat{J}_z^2$ and $\hat{J}_z$

$$\begin{aligned} \hat{J}^2 |j, m\rangle &= j(j+1)|j, m\rangle \\ \hat{J}_z |j, m\rangle &= m|j, m\rangle. \end{aligned}$$

Ladder operators are defined as $\hat{J}_\pm = \hat{J}_x \pm \hat{J}_y$ and fulfill

$$\begin{aligned} \hat{J}_+ |j, m\rangle &= \sqrt{j(j+1) - m(m+1)}|j, m+1\rangle \\ \hat{J}_- |j, m\rangle &= \sqrt{j(j+1) - m(m-1)}|j, m-1\rangle. \end{aligned}$$

There are $(N/2{+}1)^2$ of those states if N is even and $[(N{+}1)/2{+}1](N{+}1)/2$ states if N is odd. This number is in general smaller than 2^N, from which we can follow that the Dicke states labeled with j and m are degenerate. The label j corresponds to Dicke's co-operation number and takes the values $j = 1/2, 3/2, \ldots, N/2$ for $N = 1, 3, 5\ldots$ (odd) and $j = 0, 1, \ldots, N/2$ for $N = 2, 4, 6\ldots$ (even). The interest of this thesis lies in the Dicke phase transition, which is a phenomenon of the ground state. This state is contained in the manifold given by the maximal value $j = N/2$. The Dicke interaction does not couple states with different j-values and we can thus restrict our discussion to $j = N/2$.

We can readily diagonalize the Dicke Hamiltonian in the Dicke basis numerically when truncating the photonic Hilbert space. Using a standard solver for eigenvalue problems of a square matrix, a Hamiltonian with 1000 atoms and five photonic states (including the zero photon state) is diagonalized within minutes. The cavity frequency for all shown results is set to $\omega = 1000\omega_0$, according to our experimental parameters, and all energies are scaled in units of ω_0. It should be noted, that the used atom number is two orders of magnitude smaller compared to our experimental value.

2.4.5. Thermodynamic Limit

The Dicke model is now discussed in the thermodynamic limit, i.e., the atom number approaches infinity. The details for deriving the expressions are omitted, but can be found in reference [55, 56]. Mathematical expressions for the atomic inversion, the cavity-field amplitude and the order parameter are given, which are not analytically available from the mean-field description of section 2.3. By comparing them to the numerical results, we will justify their applicability to our experimental situation.

The expectation value of $\hat{J}_z$ measures the atomic inversion. It takes the value $-N/2$ in the normal phase where all atoms occupy the ground state and the coherent cavity field vanishes, i.e., $\hat{a}^\dagger\hat{a} = 0$. Above the critical coupling strength λ_c, both the cavity field and the atomic inversion will be macroscopically occupied. The corresponding mathematical expressions are given in the following table [55, 56]. Note that the values are scaled by the number of atoms N, since all quantities diverge in the thermodynamic limit $j = \frac{N}{2} \to \infty$

	$\lambda < \lambda_\mathrm{c}$	$\lambda > \lambda_\mathrm{c}$
$\langle \hat{J}_z \rangle / N$	$-1/2$	$-\lambda_\mathrm{c}^2/(2\lambda^2)$
$\langle \hat{a}^\dagger \hat{a} \rangle / N$	0	$(\lambda^4 - \lambda_\mathrm{c}^4)/(\omega\lambda)^2$

The values of $\langle \hat{J}_z \rangle$ and $\langle \hat{a}^\dagger \hat{a} \rangle$ as a function of coupling strength λ are shown in figure 2.11 alongside the numerical results. Both quantities show a sharp increase at the critical coupling strength λ_c. The numerical results show agree with the analytic expressions, despite the small atom number used. The high atom number in the experiment thus justifies to apply the thermodynamic-limit expressions to describe our experimental data.

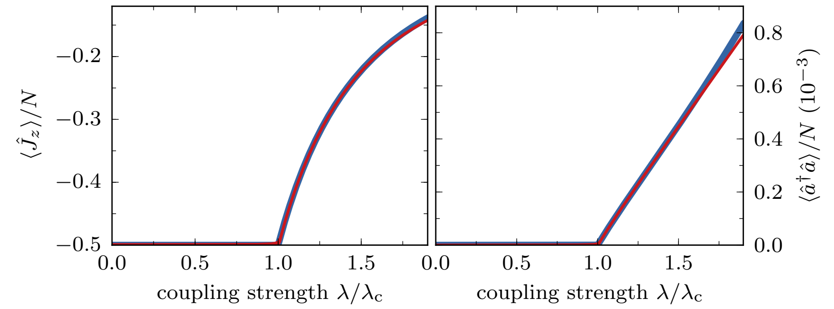

FIGURE 2.11.: The expectation values of $\langle \hat{J}_z \rangle$ and $\langle \hat{a}^\dagger \hat{a} \rangle$ as a function of coupling strength. A clear threshold behavior is visible in both quantities. The blue curves show the analytic results in the thermodynamic limit and the thin red curves present the result of exact numerical diagonalization. The parameters are given in section 2.4.4.

The order parameter for the phase transition in the framework of the Dicke model is given by the expectation value $\frac{1}{2}\langle \hat{J}_+ + \hat{J}_- \rangle = \langle \hat{J}_x \rangle$ and is explicitly written as

$$\Theta = \frac{1}{2}\langle \hat{J}_+ + \hat{J}_- \rangle = \begin{cases} 0 & \text{if } \lambda < \lambda_c \\ \pm\sqrt{1 - \frac{\lambda_c^4}{\lambda^4}} & \text{if } \lambda > \lambda_c \end{cases} . \tag{2.20}$$

The Dicke model correctly reflects the symmetry breaking at the phase transition, as the order parameter takes either positive or negative values. Figure 2.12 shows the order parameter as a function of coupling strength. It is zero below the critical point $\lambda < \lambda_c$, where it shows a pitchfork bifurcation with the two branches tending towards the extreme values, in agreement with the mean-field results of presented in section 2.3. Each of those branches corresponds to one ordered state which are label by “even” and “odd” to draw the connection to the self-organized states (see figure 2.5).

2.4.6. Energy Spectrum

The excitation-energy spectrum of the Dicke model yields further insight into the origin of the phase transition due to the competition between elementary excitation energy and interaction energy. Those energies are on the one hand the terms describing the occupation of the cavity mode and the atomic mode (which cost energy when occupying). On the other side, there is the coupling term which reduces energy if the cavity field is occupied and the atomic polarization is at a finite value. Therefore, upon an increase of the coupling strength, an eigenmode in the excitation spectrum is expected to “soften”, i.e., lower its energy and becoming degenerate with the ground state at the critical coupling strength. There a new two-fold degenerate ground state with macroscopic occupation of the fields emerges.

The Dicke model in the thermodynamic limit reduces to a set of coupled harmonic oscillators with a harmonic energy spectrum, i.e., the difference in energy of adjacent excitations is a constant. We will therefore present and discuss only the first excitation in the spectrum.

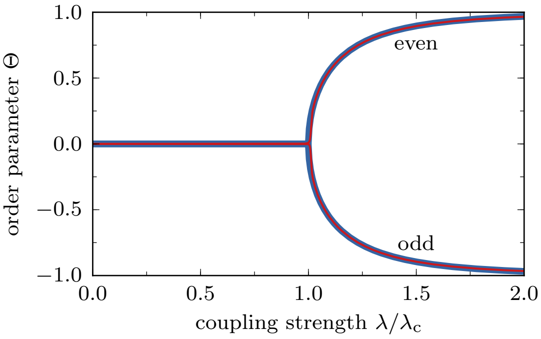

Figure 2.12.: The order parameter Θ as a function of coupling strength λ. Shown are the analytic results in the thermodynamic limit (thick blue line) alongside with the result of exact numerical diagonalization (thin red lines). The branches are labeled "even" and "odd" in accordance with previous sections. The parameters are given in section 2.4.4.

Below the threshold (i.e., $\lambda < \lambda_\mathrm{c}$) the two lowest lying energy states are given by [56]

$$\begin{aligned} \mathrm{E}_0/N &= -\omega_0 \\ \mathrm{E}_1/N &= \sqrt{\frac{1}{2}\left(\omega^2+\omega_0^2-\sqrt{\left(\omega^2-\omega_0^2\right)^2+16\lambda^2\omega\omega_0}\right)}. \end{aligned}$$

Beyond the critical point (i.e., $\lambda > \lambda_\mathrm{c}$), the energies are expressed by

$$\begin{aligned} \mathrm{E}_0/N &= -\frac{2\lambda^2}{\omega}-\frac{2\lambda_\mathrm{c}^4}{\lambda^2\omega} \\ \mathrm{E}_1/N &= \sqrt{\frac{1}{2}\left(\omega^2+\frac{\omega_0^2\lambda^2}{\lambda_\mathrm{c}^2}-\sqrt{\left(\frac{\omega_0^2\lambda^2}{\lambda_\mathrm{c}^2}-\omega^2\right)^2+4\omega^2\omega_0^2}\right)}. \end{aligned}$$

These excitation energies are displayed in figure 2.13. Indeed, we can identify a mode that "softens" and merges with the ground state. From the numerical results it is obvious, that many modes bend towards zero energy at the transition point. A small energy gap between the merged ground state and the next excited state however remains in the finite system. This gap is theoretically expected to scale with the atom number $\propto N^{-1/3}$ [60]. Regarding realistic experimental atom numbers closes this gap by another factor of 5.

2.4.7. Long-Range Interaction

The long-range character of the interaction induced by the cavity mode is discussed here within a mathematical treatment. We start with the many-body Hamiltonian (2.18), used for mapping to the Dicke model in section 2.4.2

$$\begin{aligned} \hat{\mathcal{H}} &= -\hbar\Delta_\mathrm{c}\hat{a}^\dagger\hat{a}+\int\hat{\Psi}^\dagger(\mathbf{r})\left[\frac{\hat{\mathbf{p}}^2}{2m}\right. \\ &\qquad \left.+\hbar\eta_\mathrm{p}\left(\hat{a}^\dagger+\hat{a}\right)u(\mathbf{r})\right]\hat{\Psi}(\mathbf{r})\mathrm{d}\mathbf{r}, \end{aligned}$$

where we have neglected a term ($\propto \cos^2 kx$) because, for our experimental parameters, it is much smaller compared to all other terms. In addition, it will not alter the physical content of

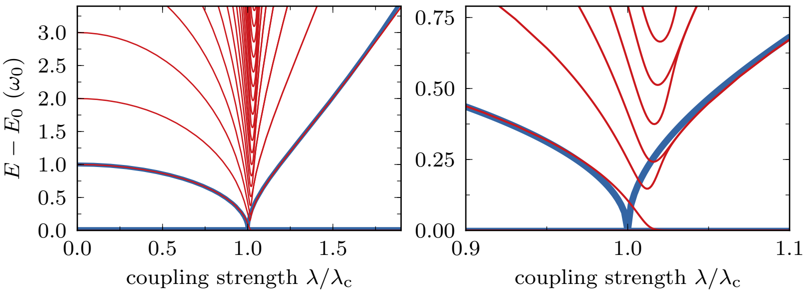

FIGURE 2.13.: Displayed is the excitation-energy spectrum as a function of coupling strength λ from analytic expressions (blue lines) and numerical diagonalizing (red lines). As the coupling strength approaches the critical value, the energy gap between the ground and the first excited state vanishes in the thermodynamic limit and a new two-fold degenerate ground state emerges. The parameters are given in section 2.4.4.

the present discussion. The interference pattern between pump and cavity field is defined in the usual way as $u(\mathbf{r}) = \cos(kx)\cos(kz)$ with the position vector $\mathbf{r} = (x, y, z)$. We calculate the equations of motion for the operators $\hat{\Psi}(\mathbf{r})$ and $\hat{a}$. They read

$$\begin{aligned} \frac{\partial \hat{\Psi}(\mathbf{r})}{\partial t} &= i\left[\frac{\hat{\mathbf{p}}^2}{\hbar 2m} - \eta_{\mathrm{p}}\left(\hat{a}^\dagger + \hat{a}\right)u(\mathbf{r})\right]\hat{\Psi}(\mathbf{r}) \\ \frac{\partial \hat{a}}{\partial t} &= i\Delta_{\mathrm{c}}\hat{a} - i\eta_{\mathrm{p}}\int \hat{\Psi}^\dagger(\mathbf{r})u(\mathbf{r})\hat{\Psi}(\mathbf{r})\mathrm{d}\mathbf{r}. \end{aligned}$$

The cavity-field follows the atomic degree of freedom within a time scale given by the cavity decay rate κ whereas the timescale of atomic motion is set by the recoil frequency, which is much lower. The cavity field will therefore adiabatically follow the atomic motion and the corresponding equation for $\frac{\partial \hat{a}}{\partial t}$ is accordingly set to zero and solved for the field operator $\hat{a}$. This yields

$$\hat{a} = \frac{\eta_{\mathrm{p}}}{\Delta_{\mathrm{c}}}\int \hat{\Psi}^\dagger(\mathbf{r})u(\mathbf{r})\hat{\Psi}(\mathbf{r})\mathrm{d}\mathbf{r}.$$

This expression is substituted back into the equation of motion for $\frac{\partial \hat{\Psi}(\mathbf{r})}{\partial t}$ yielding a single equation describing the systems dynamics. We can read off an effective Hamiltonian giving the same equation of motion as

$$\begin{aligned} \hat{\mathcal{H}} &= \int \hat{\Psi}^\dagger(\mathbf{r})\frac{\hat{\mathbf{p}}^2}{2m}\hat{\Psi}(\mathbf{r})\mathrm{d}\mathbf{r} \\ &\quad + \iint \hat{\Psi}^\dagger(\mathbf{r})\hat{\Psi}^\dagger(\mathbf{r}')U(\mathbf{r},\mathbf{r}')\hat{\Psi}(\mathbf{r}')\hat{\Psi}(\mathbf{r})\mathrm{d}\mathbf{r}'\mathrm{d}\mathbf{r}. \end{aligned}$$

The second term, where we have introduced $U(\mathbf{r},\mathbf{r}') = \left(\hbar\eta_{\mathrm{p}}^2/\Delta_{\mathrm{c}}\right)u(\mathbf{r})u(\mathbf{r}')$, has the mathematical form of an effective two-body interaction. The shape of the interaction potential $U(\mathbf{r},\mathbf{r}')$ is given by the interference pattern between cavity and pump field.

Let us consider two atoms at position $\mathbf{r}_1$ and $\mathbf{r}_2$, to illustrate the effect of this term. The atomic density for localized atoms is written as a sum of delta distribution. Evaluating the integrals leads to an interaction energy of $U(\mathbf{r}_1,\mathbf{r}_1) + 2U(\mathbf{r}_1,\mathbf{r}_2) + U(\mathbf{r}_2,\mathbf{r}_2)$ which will be minimized ($\Delta_{\mathrm{c}} < 0$) if both atoms are either on even site (i.e., $u(\mathbf{r}) = +1$) or both atoms are on odd sites (i.e., $u(\mathbf{r}) = -1$). The interaction is thus not dependent on the actual separation of the two atoms, but rather on their relative position with respect to the cavity and pump-mode function. It will thus induce correlations in their relative position of multiples of the optical wavelength along pump and cavity axis, no matter how far the atoms are apart. When considering a Bose-Einstein condensate, i.e., delocalized atomic wave-functions, the interaction minimizes its energy for a density distribution that is modulated as $\pm u(\mathbf{r})$. This implies spatial correlations of multiples of the optical wavelength.

2.5. Symmetry Breaking

The Dicke model in the thermodynamic limit shows a second-order phase transition and spontaneous symmetry breaking . The previous discussion focused on the microscopic physics of these phenomena. In this section we will give a brief introduction to the relevant concepts of second-order phase transitions and spontaneous symmetry breaking and apply them to the Dicke phase transition. The presence of an external symmetry-breaking field in our setting is discussed. For detailed information on the concepts we refer to the textbooks [84, 85, 86].

2.5.1. Second-Order Phase Transition

A phase transition is the transformation of a system from one state to another with qualitatively different properties upon the change of a control parameter. In general, a second-order transition exhibit a discontinuity in the second derivative of the free energy with respect to some thermodynamic variable at the critical point. A typical example for a second-order transition is the transition from a paramagnet to a ferromagnet. The magnetization shows a finite value below a critical temperature. It continuously reduces and eventually vanishes due to thermal fluctuations as the temperature approaches a critical point.

Characteristic for a second order phase transition is that the states on one side of the transition point show a reduced symmetry compared to the Hamiltonian describing the system. This feature is termed spontaneous symmetry breaking. For the mathematical description of the phases, a parameter measuring the degree of order, thus called order parameter, is introduced. Its mean value vanishes on one side of the transition and acquires a non-zero value on the other side.

Landau has introduced a phenomenological theory to unify the description of second-order transitions [86]. His theory deliberately circumvents the exact microscopic physics to describe

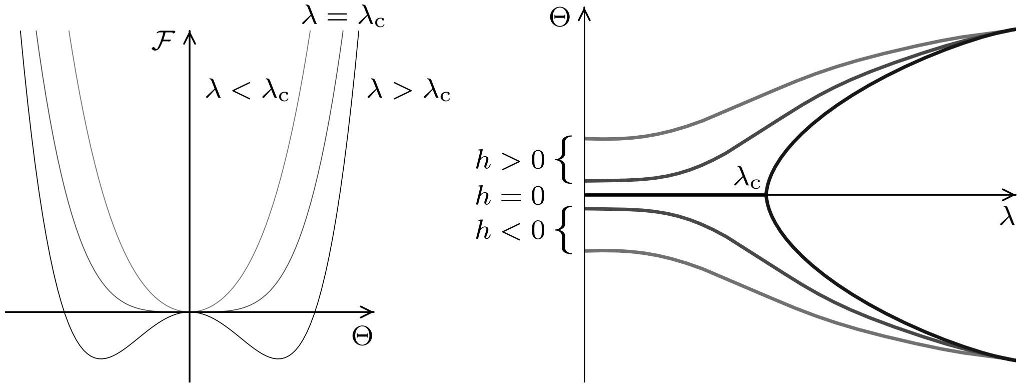

FIGURE 2.14.: The left panel shows the free energy $\mathcal{F}$ as a function of the order parameter Θ. Below threshold, i.e., the control parameter λ is smaller than the critical value λ_c, one minimum exists. Upon increasing λ beyond λ_c, the free energy shows two or more minima, between which the system may randomly decide. The right panel shows the order parameter Θ as a function of the control parameter λ in the presence of an externally applied field h. A non-zero value of h determines a finite order parameter below threshold and predetermines the sign beyond. The symmetry is thus broken explicitly rather than spontaneously.

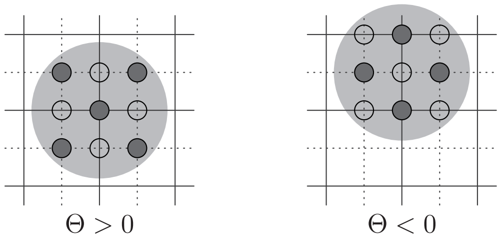

Figure 2.15.: An overlap due to the finite extension of the atomic cloud. Depending on the trap position, the number of atoms on the even sites does not balance the number of atoms on the odd sites.

the system in close vicinity of the transition point and it has proven to be very successful in describing second-order transitions. The theory is based on the assumption, that the free energy $\mathcal{F}$ of a system can be expanded in the order parameter Θ. The odd terms vanish for a second-order transition, which can yield a characteristic functional form of the free energy that is sketched in figure 2.14. It shows that the free energy in the unordered phase exhibits a minimum at zero order parameter, with a characteristic parabolic shape. As the control parameter is increased beyond the critical point, the minimum flattens and eventually splits into two or more equivalent minima. It is fluctuations, either of thermal or quantum nature, which will drive the system into either of the two minima. As an observer from the outside, not being aware of the fluctuations, the system randomly picks a final state.

The presence of any additional external field h will alter the behavior significantly, giving rise to a linear term in the Taylor expansion of the free energy. This could be an externally applied magnetic field in the example of the ferromagnetic transition. Figure 2.14 shows a sketch of the evolution of the order parameter as a function of control parameter for various values of h. The order parameter starts with a finite value below the phase transition given by the strength and sign of the field h. Upon increasing the control parameter, the order parameter increases well before the critical point and approaches the no-field curve well beyond the critical value. In this case, the symmetry was broken by the external field and the process is thus termed explicit symmetry breaking.

In order to distinguish between explicit and spontaneous symmetry breaking experimentally, great care has to be taken. One can evaluate the statistical occurrence of the symmetry-broken states over many experimental realizations. However, it is misleading to conclude that spontaneous symmetry breaking has occurred if equal probabilities for all configurations are observed. It is crucial to see that the external field might change from measurement to measurement. If the external field changes randomly between consecutive measurements, we can very easily observe equal number of occurrences of the individual final states but the symmetry was actually broken explicitly due to technical noise.

2.5.2. Finite-Size Effect

In our experiment a symmetry-breaking field originates from the finite extension of the atomic cloud which has not been taken into account by the previous discussion. We had argued, that the order parameter vanishes in the normal phase because the overlap integral $\int n(x,z)\cos kx \cos kz \mathrm{d}x\mathrm{d}z$ (see 2.14 and 2.20) vanishes for a constant atomic density. Taking

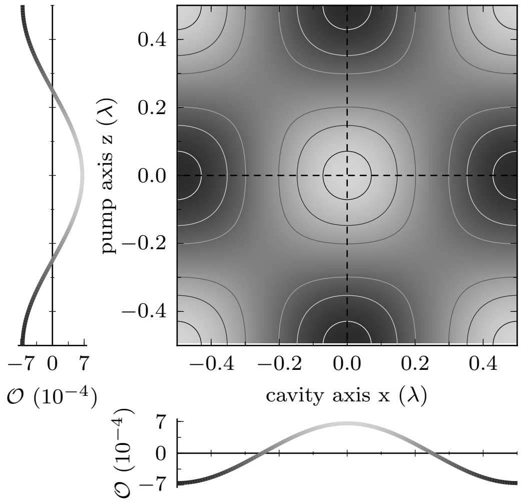

FIGURE 2.16.: Overlap due to the finite size of the atomic cloud. The atomic density $n(x, z)$ is taken from numerically solving for the ground state in the trapping potential. Shown is the overlap $\mathcal{O} = \int n(x', z') \cos(k(x' - x)) \cos(k(z' - z)) \mathrm{d}x' \mathrm{d}z'$ as a function of spatial offset x' between cavity-mode and pump axis. The plots on the side show slices indicated by dashed lines in the main graph.

into account the external trapping potential for the atomic sample yields an atomic density that is not constant in space. The population of atoms on the even sites might not exactly balance the population on the odd sites, depending on the exact location of the trapping potential with respect to the cavity mode profile. This imbalance thus yields a finite order parameter already below the threshold. Figure 2.15 illustrates the phenomenon for a very small number of atoms. More atoms residing on the even site (left panel), gives a positive order parameter. This situation is reversed if the trap center is shifted by half an optical wavelength yielding a negative order parameter.

The overlap as a function of trap location can be computed from the numerical solution of the ground state in the trapping potential. Figure 2.16 displays the result showing a sinusoidal spatial oscillation in the trap position. The maximum value of $6.6 \cdot 10^{-4}$ corresponds to a population imbalance between the even and odd sites of 66 atoms, a minute number compared to the total atom number of 10^5.

This finite-size effect can effectively be taken into account within the two mode description of equation (2.19). We expand the atomic field operator in eigenstates $\phi_n(x, z)$ of the trapping potential, obeying

$$\left[\frac{\hat{p}^2}{2m} + V(x, z)\right] \phi_n(x, z) = E_n \phi_n(x, z).$$

The Hilbert space is again restricted to the ground state ϕ_0 and one additional state, that has the largest overlap with the cavity mode profile, denoted as ϕ_1. The atomic-field operator is then written as $\hat{\Psi} = \hat{c}_0 \phi_0(x, z) + \hat{c}_1 \phi_1(x, z)$ and inserted into the many-body Hamiltonian 2.18. This yields one additional relevant term:

$$2\hbar\lambda(\hat{a}^\dagger + \hat{a})\mathcal{O}\sqrt{N} \qquad \left(\mathcal{O} = \int |\phi_0|^2 \cos(kx) \cos(kz) \mathrm{d}x \mathrm{d}z\right).$$

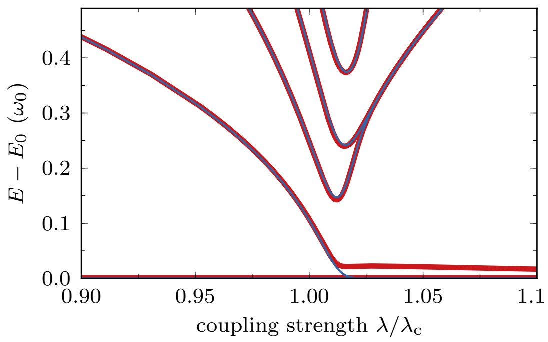

FIGURE 2.17.: The energy spectrum of the Dicke model including a symmetry breaking term. Shown is the spectrum in close vicinity of the transition point. The blue lines correspond to zero symmetry-breaking field and the red lines include a strong symmetry-breaking field. The parameters are given in section 2.4.4.

A direct consequence of this additional term is a coherent cavity field already below the threshold which explicitly breaks the symmetry. Intuitively, this can be seen by considering the scattering of photons from the pump field into the cavity mode. We had argued, that due to destructive interference, no light is scattered. This perfect cancellation can not work with a population imbalance between the even and odd sites. The resulting cavity field, despite being small, gives rise to an interference pattern with the pump field. The arising checkerboard-intensity pattern will be adapted by the atomic density, thus breaking the symmetry already before the threshold for self-organization.

The physical changes induced by the symmetry-breaking field can further be visualized in the excitation-energy spectrum obtained from numerical diagonalization. It is displayed in figure 2.17, where we have plotted a reference spectrum with no symmetry breaking field alongside. We have further chosen the finite size overlap much larger than experimentally relevant values to enhance the effect for the discussion. The no-field spectrum shows an excitation, that becomes degenerate with the ground state at the critical point. There a new two-fold degenerate ground state emerges and the system may randomly decide to occupy either of the two state. Figure 2.17 shows, that the presence of a symmetry-breaking field lifts this degeneracy of the ground states. Thus the basis for spontaneous symmetry breaking, two or more degenerate ground states, is lost. When slowly crossing the “transition point”, the system will seek the lowest-energy state and the symmetry is broken explicitly.

Experimental evidence for this symmetry-breaking field is presented in chapter 5. The influence of this field is studied and shown to vanish upon dynamically crossing the transition point with increasing transition rates.

3 Experimental Setup

The experimental apparatus used for the research discussed in this thesis has continuously evolved since its constitution in 2002. It has proven to be a versatile setup which was extended and modified in several stages and allowed to explore various physical phenomena. Initially, the apparatus was used to produce an atom laser [87, 88, 89, 90] passing a high-finesse cavity as an ultra-efficient single-atom detector. The experiments demonstrated higher order coherence of the atom laser [40] and studied the thermal to Bose-Einstein condensate (BEC) transition [91, 92, 93]. Later, the setup was modified to trap the BEC inside the cavity and allowing it to coherently couple a BEC to a single cavity mode. In those experiments collectively enhanced vacuum-Rabi splitting [94] and self-sustaining density oscillations of the BEC [95, 96] were observed.

Many experimental details have been presented thoroughly in reference [97] and various Ph.D. theses. Explicitly, the thesis of Anton Öttl [98] and Stephan Ritter [99] describe almost all aspects of the Vacuum system, the BEC production setup and the cavity itself. The thesis by Tobias Donner [100] gives a detailed description of an optical transportation system and Ferdinand Brennecke describes the cavity-laser setup [67]. This chapter will briefly review the apparatus and focus on newly build parts which are the transverse-pumping beam geometry, the optical heterodyne-detection setup and a software framework for data acquisition.

The experimental setup is conveniently distributed onto two optical tables. One of the tables is devoted to the laser system, which consists of several external-cavity diode lasers [101] and the control electronics to generate the optical frequencies needed for cooling, manipulating, and probing the atomic ensemble. Optical fibers guide the light to the second table, where the BEC is prepared in an ultra-high vacuum chamber.

3.1. Experimental Sequence

Experiments with ultracold atoms typically end with a destructive method of detecting the atomic cloud by imaging it optically. Then a new sample, i.e., a cloud of ultracold atoms, has to be prepared. The preparation procedure in our experimental setup takes around 1 min while the experiments on a sample only take $\approx 100\,\mathrm{ms}$. Each step in the preparation sequence is timed on a µs scale, while this severe timing requirement has to be maintained during the entire experimental cycle. It is achieved by a computer-control system managing the full experiment and its timing. The hardware level requires control of 36 analog-output channels, 64 digital-output channels, a local-area network interface (LAN) and a GPIB bus. On a software level, the experiment is controlled by a framework developed in our group [102].

For describing an experimental run, a data format based on XML is employed where the experiment is described in a matrix-type representation: one axis describes timing edges whereas the other axis describes hardware channels. Each entry in the matrix consist of a value (which may be time dependent) for the specific hardware channel at the corresponding time edge. The matrix concept is kept very general to cover hardware from TTL-level logic channels (i.e., on or off), digitally controlled frequency synthesizers and analog output channels controlling for example analog PID-loops. After defining the next experimental sequence with a graphical user interface, the description in XML format is sent to the main personal computer (PC) via a LAN connection. This PC has all required hardware features build in (i.e., analog/digital output cards, network connections, GPIB cards,...) and will be referred to as the "runner computer". It interprets the next sequence, pre-computes the output values and uploads the results onto all hardware devices. The timing of all devices is controlled during the sequence by sending TTL-level pulses to the specific device whenever an action is required. The experimenter may change values in the matrix from run to run (also possible automatically in a loop fashion). If no changes are made, the last matrix is automatically repeated to allow the setup to thermalize.

Additional personal computers are used for various detection techniques, e.g., absorption imaging or photon detection, which are synchronized with the main computer via LAN communication. Each of these computers requests a copy of the XML-data in the beginning of the run, sets up the detection hardware (e.g., cameras, ADCs, ...) accordingly and records the data upon a TTL-trigger pulse send from the runner. The recorded data is stored with the XML-code as meta data. The use of this meta-data system has proven to be useful for later data analysis, as every piece of data stored includes a full set of information on the corresponding experimental run.

The next section will briefly describe the standard experimental cycle for preparation of a BEC. Most of the steps are not only separated in time, but also in space as the atomic cloud is physically shifted during the experimental sequence. An overview of the experimental vacuum chamber alongside the timing sequence is displayed in figure 3.1.

3.1.1. MOT - Transport - QUIC

The experimental sequence starts in a vacuum chamber with a background pressure of 10^{-9} mbar where a magneto-optical trap (MOT) [103, 104] is loaded with ^{87}Rb atoms from a dispenser source. The MOT operates at the D2 line of ^{87}Rb [105] at a wavelength of 780.2 nm with a loading time of 18 s and yields $\approx 2 \cdot 10^9$ atoms in the µK regime. We subsequently further reduce the temperature by sub-Doppler cooling in an optical molasses during 10 ms [106]. This step is followed by a 2 ms optical-pumping sequence [106], preparing the atoms in the low-field seeking state $|\mathrm{F} = 1, \mathrm{m_F} = -1\rangle$, where F denotes the total angular momentum and $\mathrm{m_F}$ the magnetic quantum number. The cloud is then trapped with a magnetic quadrupole trap.

The high background pressure in the MOT chamber prevents reaching quantum degeneracy due to collisions. The atoms are thus magnetically transported horizontally [107] through a differential pumping tube into the main chamber with a pressure of 10^{-11} mbar. Trapped in a quadrupole-Ioffe type trap (QUIC) [108], radio-frequency induced evaporative cooling is performed until just above the critical temperature for Bose-Einstein condensation to set in.

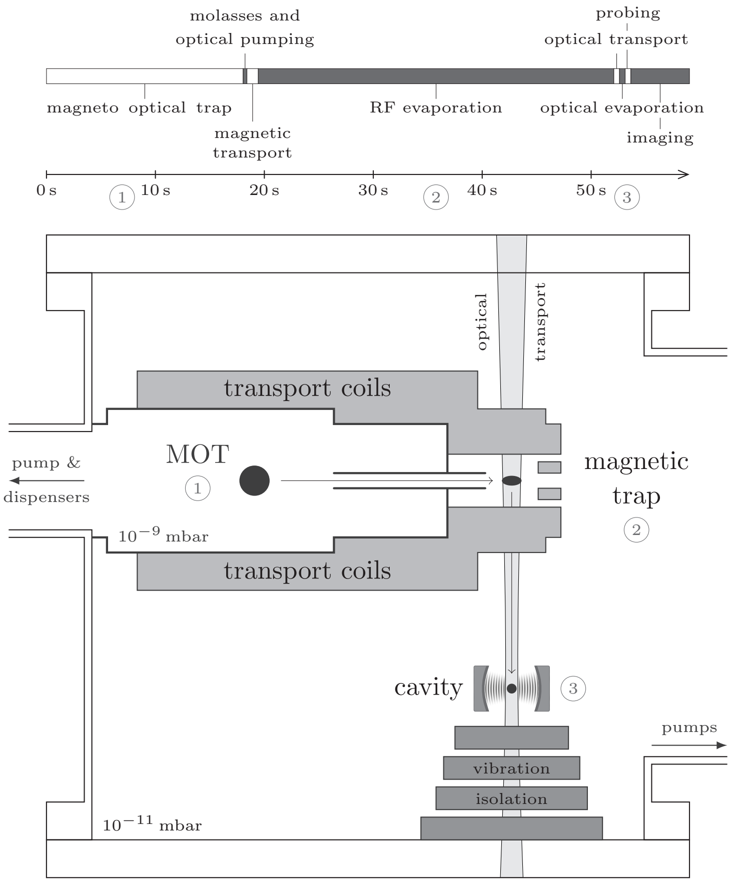
molasses and
optical pumping
probing
optical transport
magneto optical trap
magnetic
transport
RF evaporation
optical evaporation
imaging
0 s
①
10 s
20 s
30 s
②
40 s
50 s
③
optical
transport
transport coils
MOT
①
pump &
dispensers
10^{-9} mbar
magnetic
trap
②
transport coils
cavity
③
pumps
vibration
isolation
10^{-11} mbar

FIGURE 3.1.: Timing sequence and sketch of the experimental apparatus. The atoms are pre-cooled in a magneto-optical trap, transported into an ultra-high vacuum chamber and evaporatively cooled to near quantum degeneracy. After optical transportation, the atoms are trapped in the cavity by a crossed-beam dipole trap where a last step of evaporative cooling yields a BEC.

3.1.2. Optical Transport and Trapping

The atomic cloud is then vertically transported by 36 mm to the position of the high-finesse cavity in an optical conveyor belt [109, 110], generated by two counter-propagating laser beams. We provide the light by two tapered amplifiers, giving ≈ 100 mW light power on the experimental table each. Both amplifiers are seeded by a common external-cavity diode laser [101] at 852 nm which is stabilized onto the D2 transition of ^{133}Cs [111] via frequency modulation spectroscopy [112]. At the position of the cavity, the atoms are loaded into a crossed-beam dipole trap formed by one of the transport beams and an additional beam on the horizontal axis. In this optical trap, a further step of evaporative cooling is performed to reach quantum degeneracy, yielding a BEC with condensation fraction of $> 90\,\%$.

3.2. The High-Finesse Cavity

The centerpiece of the apparatus is a high-finesse optical cavity in Fabry-Pérot geometry [113] which is mounted on a vibration isolation stack to reduce mechanical noise. We work in the near-planar symmetric limit with two identical mirrors having a radius of curvature of 75 mm and a separation of 178 μm. In this geometry, the longitudinal modes are spaced by 852 GHz with a transverse-mode spacing of 18.5 GHz. The TEM_{00} mode, to which we couple experimentally, has a waist radius of 25.3 μm and a corresponding mode volume of $88 \cdot 10^3\,\mu\mathrm{m}^3$. The dielectric reflective coating of the mirrors is of very high optical quality, showing transmission of only 2.3 ppm and losses of 6.9 ppm. We achieve a Finesse of $\mathcal{F} = 3.4 \cdot 10^5$ corresponding to a quality factor of $1.6 \cdot 10^9$ and the cavity resonance shows a line width (FWHM) of 2.5 MHz at 780 nm.

In the experiment, we load a BEC of ^{87}Rb atoms, optically pumped into the $|\mathrm{F} = 1, \mathrm{m_F} = -1\rangle$ state, into the cavity mode. Only σ_+ or σ_- polarized cavity photons can couple to atomic transition due to a small magnetic field along the cavity axis ($B \approx 0.1\,\mathrm{G}$). For a single σ_+ or σ_- polarized photons we calculate an atom-light coupling strength of $g_+ = 2\pi \cdot 14.1\,\mathrm{MHz}$ and $g_- = 2\pi \cdot 10.9\,\mathrm{MHz}$ [99, 67] corresponding to single-photon cooperativity parameters of $C_+ = 25.5$ and $C_- = 15.5$. The system is thus in the regime of single-atom single-photon strong coupling, where the coherent coupling rate $g_{+/-}$ is larger than all decoherence rates, dominated by the cavity-field decay rate $\kappa = 2\pi \cdot 1.3\,\mathrm{MHz}$ and the decay rate of the atomic dipole $\gamma = 2\pi \cdot 3\,\mathrm{MHz}$ [105].

3.3. The Transverse Pump

For the experiments presented in this thesis, the existing setup had to be extended to allow for transverse pumping of the BEC with a standing-wave light field. We will describe the setup here and it is shown in figure 3.2.

The principal concept is to use the same optical fiber and optical beam path as used for the transport and trapping light. On the laser table side, the optical transport light at 852 nm and the transverse pumping light at 785 nm are combined with a dichroic mirror and coupled into a single-mode optical fiber, that guides the light to the top of the experimental chamber. After an optical isolator, the beam is expanded along one axis with a cylinder-lens telescope to account for the restricted optical access in the vacuum chamber. Light leaking through mirrors in the beam path is filtered with optical-bandpass filters (to distinguish between the two wavelengths) and detected with photodiodes used to actively stabilize the intensity of the beams via electronic control-loops. After a second telescope to further increase the beam waists, the beams pass a special dichroic waveplate. This custom-made waveplate has no influence on the transport light but the polarization axis of the transverse pump beam is rotated by 90 ° to be linearly polarized orthogonal to the cavity axis. A lens with focal length of 400 mm focuses both beams to the center of the cavity mode. This lens is mounted on an a x-y-z translation stage for aligning the position of the beams with respect to the cavity mode. After the beams have passed the vacuum chamber, the almost identical optical setup is reversed, assuring that the lower transport beam, traveling in the opposite direction, shows identical properties. The major difference is a dichroic mirror in the beam path, that transmits the transverse pump light from the top. After this mirror, a retro-reflecting

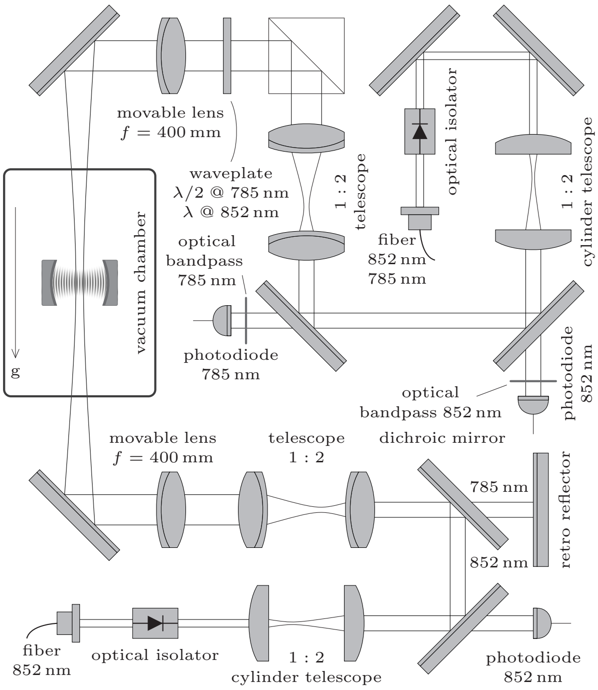
movable lens
$f = 400$ mm
waveplate
$\lambda/2$ @ 785 nm
λ @ 852 nm
optical
bandpass
785 nm
1 : 2
telescope
optical isolator
fiber
852 nm
785 nm
1 : 2
cylinder telescope
vacuum chamber
g
photodiode
785 nm
optical
bandpass 852 nm
photodiode
852 nm
movable lens
$f = 400$ mm
telescope
1 : 2
dichroic mirror
785 nm
852 nm
retro reflector
fiber
852 nm
optical isolator
1 : 2
cylinder telescope
photodiode
852 nm

Figure 3.2.: Optical setup for the transverse pumping beam at 785 nm. The same optical fiber is used for the transport light at 852 nm. A custom made waveplate rotates the polarization axis of the pump light to be orthogonal to the cavity axis while leaving the polarization axis of the transport light unaffected. Gravity (g) points downwards.

mirror, i.e., reflective under 0° angle of incidence, is installed on a mount, that is adjustable by piezo actuators (Newport Agilis AG-M100N). The back reflected beams together with the initial pump beam forms the standing-wave pump at the position of the atoms. The use of piezo actuators is necessary, because the geometric length of the beam path after the vacuum chamber exceeds 1 m which requires an angle resolution for adjusting the retro reflector below 10^{-5} rad.

The described scheme of using the identical beam path for trapping and pumping light ensures a perfect geometrical overlap between both beams. The spatial extension of both the transport beam and the pumping beam are intrinsically matched at the position of the cavity mode and measured to be 29 μm (cavity axis) and 53 μm. The scheme however suffers from chromatic aberrations of the optical elements. The lenses, even though achromatic, are not optimized for the used wavelengths. Using a commercial ray-tracing software, we confirmed that the focal position of the two wavelengths differs by 1.3 mm along the beam path. The Rayleigh range of the beams is however calculated to be 3.6 mm, which is larger than the mismatch in focal position. The wavefront distortion of the transverse pump beam at the position of the atoms is thus expected to be small.

3.4. Single-Photon Counting Module

We detect photons leaking out of the cavity with single-photon counting modules (SPCM) from the manufacturer “PerkinElmer”. These very convenient detection units employ a silicon avalanche photodiode and incorporate high-speed electronics to yield a TTL-level pulse whenever a photon is detected (quantum efficiency is $\approx 50\,\%$). After a photon has been detected, the avalanche photodiode and the electronics needs $\approx 50\,\mathrm{ns}$ to recover in which no photon can be detected (typically referred to as “dead time”). This yields an absolute maximum detectable count rate of $20 \cdot 10^6$ photons/s, where severe saturation effects set in already at much lower count rates.

The electronic pulses signaling detected photons are registered with a time digitizer “P7888” from the manufacturer “Fast Comtech GmbH”. The arrival times of each photon, within a 1 ns resolution, are written into a FIFO memory buffer and transferred via the PCI-bus into the main memory. This architecture allows for peak rates of up to 1 GHz, but cannot maintain this count rates for long time due to the limited band with of the PCI bus as well as system latencies. Detected events are overwritten if the amount of data stored in the FIFO buffer exceeds its capacity. If the experiments performed yield high count rates, it is crucial to decrease the optical efficiency of the beam path (with neutral density filters) to prevent saturation effects in the SPCM and data loss in the digitizer. The software controlling the digitizer and synchronization with the experiment is described in the section 3.6.

3.5. Balanced Optical Heterodyne Setup

A balanced optical heterodyne-detection system as an alternative to the single photon counting modules (previous section) is described. After giving a general introduction to the concept of balanced heterodyne detection, we will present details of our system. We then proceed by presenting the calibration procedure and compare our system with the theoretical achievable noise limit.

Principle of Optical Heterodyne Detection

A photodiode measures the photon flux impinging on it and is thus insensitive to the optical phase of the incident light field. It is however possible to measure the complex electric field (i.e., both amplitude and phase) of the incoming field by optically mixing it with a coherent reference field of stable phase, called local oscillator (LO). By detecting the superposition of both fields, we can reconstruct the relative phase information. In addition, small optical fields can be measured with this technique due to optical amplification of the signal by a strong LO field. The method is called “heterodyne detection” if the frequency of the signal field ω_s differs from the LO frequency ω_lo.

Let $\mathcal{E}_\mathrm{s}(t) = E_\mathrm{s} e^{i(\omega_\mathrm{s} t + \phi(t))}$ and $\mathcal{E}_\mathrm{lo}(t) = E_\mathrm{lo} e^{i\omega_\mathrm{lo} t}$ be the time-varying complex electric field of signal and LO with real amplitudes E_s and E_lo. The factor $\phi(t)$ describes a time varying phase factor, which is the signal to be measured. These fields are overlapped on an optical beam splitter and the two output ports are measured with photodiodes. The 50/50 beam splitter will induce a phase shift, different for the transmitted and reflected beam and depends on the exact type of the optical device. We will use the standard convention for the phase shift in a single beam splitter, which includes a π phase shift for one of the reflected beams [114]. The intensity impinging on the photodiodes labeled with 1 and 2 is written as

$$I_{1/2} = I_\mathrm{s} + I_\mathrm{lo} \pm 2\sqrt{I_\mathrm{s} I_\mathrm{lo}} \cos\left[\Delta \cdot t + \phi(t)\right],$$

where we have introduced the bare intensities I_s and I_lo of the signal and LO beam as well as the difference frequency $\Delta = \omega_\mathrm{s} - \omega_\mathrm{lo}$. The optical power P detected by the photodiodes is given by the intensity integrated over the photo-diode detection area which should be larger than the beam extension. This power generates a photocurrent that is proportional to the quantum efficiency of the photodiode and the photon flux, i.e., the integrated power divided by the energy of a photon. Denoting $\bar{i}_\mathrm{s}$ and $\bar{i}_\mathrm{lo}$ as the bare photocurrents from the beams, we write the photodiode currents as

$$\bar{i}_{1/2} \approx \bar{i}_\mathrm{lo} + \bar{i}_\mathrm{s} \pm 2\sqrt{\bar{i}_\mathrm{s} \bar{i}_\mathrm{lo}} \cos\left(\Delta \cdot t + \phi(t)\right).$$

The photocurrents of the detectors are subtracted electronically which strongly reduces the influence of technical noise on the LO. The resulting current is thus given by

$$\bar{i}_\mathrm{tot} \propto \sqrt{\bar{i}_\mathrm{s} \bar{i}_\mathrm{lo}} \cos\left(\Delta \cdot t + \phi(t)\right).$$

This expression shows one great advantage of balanced heterodyne detection compared to direct intensity measurements: the measured photocurrent depends on the product of the light intensity of both the signal and LO beam. A small signal field can thus be amplified optically by increasing the LO intensity. On the other, the signal oscillates at a frequency Δ, which can be chosen freely by setting ω_lo appropriately. Setting the frequency difference Δ in the radio-frequency regime (RF) allows to use off-the-shelve components for the following electronic processing.

We want to extract the phase term $\phi(t)$ from the photocurrent $\bar{i}_\mathrm{tot}$, which oscillates in time with a frequency of Δ. This task is achieved fully electronically. At first, the current signal is converted into a voltage signal with a trans-impedance amplifier. The voltage signal, still oscillating at radio frequency, is then split into two parts where one of these signals is shifted in phase by $\pi/2$. Both are then electronically mixed with a RF signal proportional to $\cos(\Delta t + \tau)$ (τ is an arbitrary but constant phase factor). The non-linearity of this process, generates terms oscillating at 2Δ and terms oscillating at the difference of the input frequencies, i.e., in our case $\Delta - \Delta = 0\,\mathrm{Hz}$. The quickly oscillating terms are filtered by electronic means and the remaining two signals are proportional to $\sin(\phi(t) - \tau)$ and $\cos(\phi(t) - \tau)$. From this we can reconstruct the signal field (apart from a phase factor determined by τ) by

$$\begin{aligned} E_\mathrm{s} &\propto \left[\cos(\phi(t) - \tau) + i \sin(\phi(t) - \tau)\right] \\ &= e^{-i\tau} e^{i\phi(t)}. \end{aligned}$$

The overall efficiency of the system is determined by many factors, for example LO intensity, optical losses, quantum efficiency of the photodiodes and amplifier gain. We must therefore calibrate the setup, to relate a measured voltage value with an impinging signal intensity. The procedure will be presented after the description of our implementation.

Implementation

Our implementation of the heterodyne detection is sketched in figure 3.3. A laser beam is split already on the laser table, to give the transverse pumping beam and the local-oscillator beam. We couple both into two independent optical fibers guiding the light towards the experimental setup, where the transverse pumping beam enters the optical setup described in section 3.3. The advantage of using two independent fibers is that we can freely place the local oscillator beam near the detection photodiodes. A great disadvantage however is low-frequency phase noise on the light fields introduced by the optical fibers in the kHz regime. This noise, different for the two fibers, has to be actively compensated.

Both beams pass acousto-optical modulators (AOM) before the optical fibers which are operated at different frequencies to induce a small frequency difference between LO and pump beam (55 MHz in our setup). The AOMs are used as actuators to control the beam intensities via the amplitude of their driving RF input and we can additionally control the phase of the light fields by shifting the frequency of the RF inputs. We have chosen not to compensate the noise of both fibers independently, but rather stabilize the local-oscillator field onto the transverse-pump field, so that their relative phase is constant.

To measure the relative phase, we have set up an additional heterodyne setup. As reference beam, we us a small fraction of the pump light, that leaks through the retro-reflecting mirror (see section 3.3). Half of the local-oscillator power on the experiment side is combined with this reference on a 50/50 beam splitter and detected. The photodiode output is electronically mixed with a 55 MHz RF source to yield the phase noise introduced by the fibers. This signal is directly fed into the frequency modulation input of the RF source driving the local-oscillator AOM. This setup effectively realizes a proportional control loop that keeps the relative phase between LO and pump field constant. The remaining phase noise at the position of the retro reflector is measured to be below $\pi/10$.

The cavity output, which we want to measure, propagates along a different beam path compared to the LO path on their way to the photodiodes. We have measured the drift of the differential path length of the beam lines, which translate into drifts of the detected phase signal, to be about 0.1π /s. Our typical measurement time on a BEC is below one second, and we can thus easily distinguish the two superradiant configurations, separated by a π-phase difference. Due to the long separation between measurements of 60 s (because of the long BEC preparation time), we can however not compare the measured phase values between consecutive runs.

The intensity of the transverse pump beam is further actively stabilized in order to reduce technical noise. Leakage light through a mirror after the optical fiber is detected with a standard photodiode and used as error signal for a home-build proportional-integral controller. The set point of this control loop is provided by the runner pc and the AOM before the optical fiber is used as actuator for the control loop.

The main heterodyne setup follows the theoretical description above. We use a package of balanced photodiodes including the electronic subtraction and an amplifier stage (Thorlabs PDB110A). Electronic splitting, mixing and amplification is achieved with discrete components from the manufacturer Mini-Circuits and a last filter stage employs a programmable dual-channel Butterworth filter (Krohn Hitec Co. model 3940). For digitizing we use high-speed analog-to-digital converters in a personal computer (National Instruments PCI-6132).

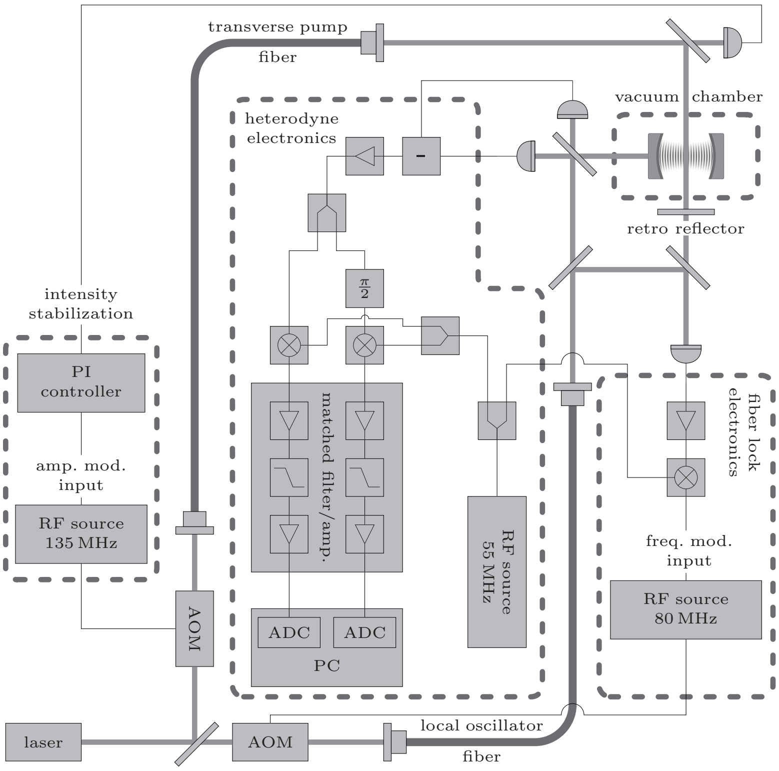
transverse pump
fiber
vacuum chamber
heterodyne
electronics
-
retro reflector
intensity
stabilization
$\frac{\pi}{2}$
PI
controller
matched filter/amp.
fiber lock
electronics
amp. mod.
input
RF source
135 MHz
RF source
55 MHz
freq. mod.
input
RF source
80 MHz
AOM
ADC
ADC
PC
laser
AOM
local oscillator
fiber

Figure 3.3.: Schematic representation of the heterodyne setup and phase stabilization of the local-oscillator fiber. Also shown is the intensity regulation for the transverse pump beam. The thin lines (—) represent electronic signals, the medium gray lines (▬) correspond to optical beam lines and the thick dark-gray lines (▬) correspond to optical fibers, that introduce phase noise, which has to be canceled with the help of an active phase stabilization loop. The symbols correspond to: ▷ RF amplifier, ⊏ RF splitter 3 dB, $\boxed{-}$ RF electronic difference, $\boxed{\frac{\pi}{2}}$ RF $\frac{\pi}{2}$-phase shifter, ⊗ RF mixer, ╲ RF low-pass filter, ▯ fiber coupler, ◖ photodiode and ⁄ (semi-transparent) mirror.

Calibration of the System

We digitize two voltage values with the heterodyne setup, where their squared sum is proportional to the impinging light intensity. To be able to assign an intracavity photon number to the heterodyne voltages, we have to calibrate the setup. The basic procedure is presented.

The cavity is driven (i.e., pumped with a laser) on the cavity axis. A fraction of this pump beam is split off before the cavity to monitor its amplitude. The challenge in calibration stems from the desire to detect ultra-small light fields with the heterodyne system. This design choice demands for high amplification of the involved RF signals to allow to measure light powers on the order of pW. This power level is however much to small to detect with a commercial calibrated power meter. Increasing the power to a level, detectable with the power meter, fully saturates the heterodyne electronics, prohibiting to directly compare the optical power with the measured heterodyne voltages.

The calibration scheme we use consists of two steps. We first set the pump-light level to different values and measure the transmitted light power with the power meter directly after the cavity output (only one vacuum window is in between the cavity mirror and the power meter). With this data, we can assign a pump level (measured before the cavity) with the cavity-transmitted power. In a second step, we repeat a similar sequence with much lower light levels detected by the heterodyne system. From this measurement, we can relate the pump level to a heterodyne voltage. From both measurements, the system's voltage response on cavity-output light is calculated to be $\approx 2.5\,\frac{\mathrm{nW}}{\mathrm{V}}$ (at a LO power of $450\,\mu\mathrm{W}$).

We now have to assign the light power leaking out of the cavity to a mean intracavity photon number. This is readily done by calculating the power leakage of a coherent cavity field with one mean photon. It is given by (for a derivation see reference [99, 67, 115])

$$\mathrm{P}_{\mathrm{photon}} = h\nu\Delta_\nu\mathcal{T},$$

where we have introduce the resonance frequency of the cavity ν, the free spectral range of the cavity $\Delta_\nu = \frac{c}{2L}$ with c the speed of light and L the length of the cavity and the transmission of the cavity mirror $\mathcal{T} = 2.3\,\mathrm{ppm}$. We evaluate the response of the heterodyne system to be $\approx 0.2\,\frac{\mathrm{V}^2}{\text{cavity photon}}$ (at a LO power of $450\,\mu\mathrm{W}$).

Comparison with the Theoretical Noise Limit

The performance in terms of noise of our system will now be compared to the theoretical limit of optical heterodyne detection where the noise of a detected signal is dominated by optical shot noise of the local oscillator beam. We follow the procedure described in reference [116, 117], where it is shown, that a heterodyne setup at the fundamental limit follows

$$\left(\frac{S^2}{N}\right)_{\mathrm{het}} = 4T\eta\mathscr{S}m, \tag{3.1}$$

where S is the mean value of the quadrature amplitude signal, N its variance, T is the measurement time, η the overall photon detection efficiency, $\mathscr{S}$ the cavity decay rate due to mirror transmission and $m = |\langle\alpha\rangle|^2$ is the mean intracavity photon number.

The noise of the system should be given by the optical shot-noise of the local-oscillator beam which can always be achieved if the power of the LO beam is chosen large enough. The condition was confirmed by blocking the signal beam and evaluating the photo-current noise for different DC-power levels of the LO. From the analysis we conclude that the noise on the photocurrent is indeed given by LO photon shot-noise.

The photon detection efficiency is determined by three factors $\eta = \mathcal{V}\zeta\tau$, where $\sqrt{\mathcal{V}}$ gives the spatial overlap of the signal and local-oscillator beam, ζ the quantum efficiency of the photodiodes and τ the optical efficiency of the detection path. This optical efficiency is readily determined with an optical power meter by measuring the optical power after the cavity output and comparing it with the optical power measured directly in front of the photodiodes. In our system, this value was determined to a value of $\tau = 0.70$. The quantum efficiency is taken from the data sheet of the photodiode to be $\epsilon = 0.84$. By evaluating the contrast of the photodiode output signal measuring the interfering signal and local-oscillator beam, we infer the spatial overlap to be $\sqrt{\mathcal{V}} = 0.75$. We determined an overall value of $\eta = 0.33$. From the knowledge of the mirror transmission $\mathcal{T}$ and the loss-coefficient $\mathcal{L}$, the value of $\mathscr{S}$ is calculated to be $\mathscr{S} = \kappa\frac{\mathcal{T}}{2\mathcal{T}+2\mathcal{L}} = 162.5\,\mathrm{kHz}$.

Equation (3.1) is reinterpreted as a calibration method by rewriting it as

$$|\langle\alpha\rangle|^2 = \frac{1}{4T\eta\mathscr{S}}\left(\frac{S^2}{N}\right)_{\mathrm{het}}. \tag{3.2}$$

For analyzing a measured cavity-output signal, we can evaluate all quantities on the right hand side of this equation and compute the intracavity photon number $|\langle\alpha\rangle|^2$. Comparing this method (which is based on the signal's noise and only valid for a truly shot-noise limited system) with the power-meter based calibration procedure presented before, we find a deviation by a factor of ≈ 1.7 in photon numbers. The method based on noise (equation (3.2)) gives a lower value, which hints to excess noise on the intensity of the measured pump beam. Indeed, many weeks after the data was taken, we found discrete peaks at acoustic frequencies in the Fourier spectrum of the cavity-field traces. To check whether this is the origin of the discrepancy, we have eliminated those peaks in the Fourier spectrum and transformed the traces back into the time domain. The relative factor in the photon number between the two calibration methods then reduces to ≈ 1.4. Hence, the quoted number of comparing our system to the theoretical limit should be interpreted as an upper bound because it seems dominated by technical noise of the signal beam.

3.6. Data Acquisition Software

The single photon counting modules and the optical heterodyne setup have to be synchronized with the experimental cycle. The recorded data is displayed immediately to allow real-time analysis and the data is saved to the hard disk. This is accomplished by a software, developed in the course of this thesis. It runs on two separate personal computers, each designated for read-out of the SPCM and the heterodyne setup respectively. The underlying software framework is identical for both purposes, only replacing the hardware-specific code part.

The basis of this framework is implemented in Python using GTK+ for displaying a graphical user interface. The framework Twisted is used for multi-threaded implementation of the network protocols to communicate with the runner computer. This part of the software, also controlling the hardware and data storage, is referred to as the backend. An additional part, referred to as the frontend, is implemented using "MathWorks MATLAB". Its purpose is to display the acquired data and give functionality for real-time analysis (e.g., filtering, Fourier transform, second order correlation functions, . . .). This hybrid approach was chosen, so that the frontend can be easily expanded due to the widespread knowledge of MATLAB. The communication between Python and MATLAB is implemented via the "MATLAB COM Automation Server" interface. It should be noted, that the names "frontend" and "backend" do not imply only one having a graphical user interface where rather both give the user graphical possibilities to interact.

We will now describe an experimental cycle in terms of software logic, also displayed in figure 3.4. After start up, the software connects to the runner computer and requests information on the next cycle. This TCP/IP is kept open until the next experimental sequence starts and the runner computer sends the XML set of information, describing the next run. The XML data is parsed and all relevant parameters are extracted, which is for example the total time of recording. The hardware is set in a state where it waits for an external TTL trigger (which is supplied by the runner computer) to start the recording. The software waits

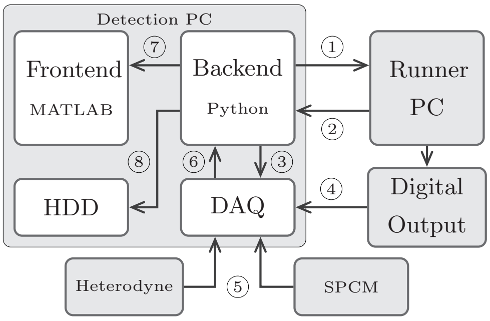

Figure 3.4.: Schematic representation and timing sequence of the heterodyne/SPCM data-acquisition software. The numbers show the timing sequence: ① backend initiates network connection to runner pc, ② runner pc sends XML data set for run, ③ backend initializes data acquisition hardware, ④ runner pc sends TTL-trigger pulse to start data acquisition, ⑤ data acquisition hardware reads values from SPCM/heterodyne, ⑥ data is transferred to backend, ⑦ data is transferred to frontend and displayed, ⑧ data is saved to hard-disk drive.

until the data is taken, reads it and pushes it into a variable in the MATLAB workspace. It then invokes a MATLAB function, which processes and displays the data. This is the only time, when both the MATLAB interface and the Python program are blocked and do not accept user interaction. The period takes $< 1\,\mathrm{s}$, depending on the amount of data taken. After MATLAB finishes, the backend compresses the data and stores it on the hard disk drive. Then the cycle restarts with the communication to the controlling computer.

The full data set stored on the hard-disk drive consists of the raw data taken in a binary format, the XML data from the runner and further settings made locally. All these separate files are compressed using TAR as a container format and GZIP as compression algorithm. The format was chosen, because MATLAB has build-in commands to read it and there are good tools to extract the data on Windows computers (besides every Linux distribution including the required tools by default). The SPCM data is very efficiently stored because the arrival time of each photon is written in a 32-bit integer representing a time in ns. If no photons are detected, no data is stored. This is fundamentally different from the hardware used to record the heterodyne data, which is an analog-to-digital converter. Even if no actual signal is applied, the hardware reads voltage values for every time bin. This voltage value is stored in a 64-bit float variable. At full sampling-rate of 4 MHz with all four channels read, this results in a data-rate of 120 Mbyte/s. Even though in principal no problem, it is not desirably for hard-disk space and processing-speed reasons. The underlying analog-to-digital converters operate at a 15-bit resolution. A linear calibration curve is then applied by the software drivers to yield 64-bit floats representing a voltage. We can thus reverse this calibration procedure, to recover the raw 15 bit data. When storing the raw data, the calibration curve is saved as meta data, so that any software reading it later, must apply the calibration. This trick reduces the data by a factor of four, yielding a maximal data rate of 30 Mbyte/s.

4 The Dicke Phase Transition with a Superfluid Gas

A phase transition describes the sudden change of state of a physical system, such as melting or freezing. Quantum gases provide the opportunity to establish a direct link between experiments and generic models that capture the underlying physics. The Dicke model describes a collective matter–light interaction and has been predicted to show an intriguing quantum phase transition. Here we realize the Dicke quantum phase transition in an open system formed by a Bose–Einstein condensate coupled to an optical cavity, and observe the emergence of a self-organized supersolid phase. The phase transition is driven by infinitely long-range interactions between the condensed atoms, induced by two-photon processes involving the cavity mode and a pump field. We show that the phase transition is described by the Dicke Hamiltonian, including counter-rotating coupling terms, and that the supersolid phase is associated with a spontaneously broken spatial symmetry. The boundary of the phase transition is mapped out in quantitative agreement with the Dicke model. Our results should facilitate studies of quantum gases with long-range interactions and provide access to novel quantum phases.

This chapter is published in reference [2]: K. Baumann, C. Guerlin, F. Brennecke and T. Esslinger, *Dicke quantum phase transition with a superfluid gas in an optical cavity*, Nature 464(7293), 1301 (2010).

4.1. Introduction

The realization of Bose-Einstein condensation (BEC) in a dilute atomic gas [118, 119] marked the beginning of a new approach to quantum many-body physics. Meanwhile, quantum degenerate atoms are regarded as an ideal tool to study many-body quantum systems in a very well controlled way. Excellent examples are the BEC-BCS crossover [120, 121, 122] and the observation of the superfluid to Mott-insulator transition [123]. The high control available over these many-body systems has also stimulated the notion of quantum simulation [124, 125], one of the goals being to generate a phase diagram of an underlying Hamiltonian. However, the phase transitions and crossovers which have been experimentally investigated with quantum gases up to now are conceptually similar since their physics is governed by short-range interactions.

In order to create many-body phases dominated by long-range interactions different routes have been suggested, most of which exploit dipolar forces between atoms and molecules [126]. A rather unique approach considers atoms inside a high-finesse optical cavity, so that the cavity field mediates infinitely long-range forces between all atoms [127, 128]. In such a setting a phase transition from a Bose-Einstein condensate to a self-organized phase has been predicted once the atoms induce a sufficiently strong coupling between a pump field and an empty cavity mode [35, 34]. Indeed, self-organization of a classical, laser-cooled atomic gas in an optical cavity was observed experimentally [36]. Conceptually related experiments studied the atom-induced coupling between a pump field and a vacuum mode using ultracold or condensed atoms. This led to the observation of free-space [15, 16] and cavity-enhanced [18] superradiant Rayleigh scattering, as well as to collective atomic recoil lasing [18, 17]. Both phenomena did not support steady-state quantum phases, and became visible in transient matter wave pulses.

A rather general objective of many-body physics is to understand quantum phase transitions [21] and to unravel their connection to entanglement [129, 130]. An important concept within this effort is a system of interacting spins in which each element is coupled to all others with equal strength. The most famous example for such an infinitely coordinated [131] spin system is the Dicke model [1], which has been predicted to exhibit a quantum phase transition more than thirty years ago [19, 20]. The Dicke model considers an ensemble of two-level atoms, i.e., spin-1/2 particles, coupled to a single electromagnetic field mode. For sufficient coupling this system enters a superradiant phase with macroscopic occupation of the field mode. A promising route to realize this transition has been proposed recently in the setting of cavity quantum electrodynamics by Carmichael and coworkers [33]. In their scheme strong coupling between two ground states of an atomic ensemble is induced by balanced Raman transitions involving a cavity mode and a pump field. This idea circumvents the thought to be unattainable condition for the Dicke quantum phase transition which requires a coupling strength on the order of the energy separation between the two involved atomic levels.

In this work we realize the Dicke quantum phase transition in an open system and observe self-organization of a Bose-Einstein condensate. In the experiment, a condensate is trapped inside an ultrahigh-finesse optical cavity, and pumped from a direction transverse to the cavity axis, as shown in figure 4.1. We will theoretically show that the onset of self-organization is equivalent to the Dicke quantum phase transition where the two-level system is formed by two different momentum states which are coupled via the cavity field. At the phase transition a spatial symmetry of the underlying lattice structure, given by the pump and cavity modes, is spontaneously broken. This steers the system from a flat superfluid phase into a quantum phase with macroscopic occupation of the higher-order momentum mode and the cavity mode. The corresponding density wave together with the presence of off-diagonal long-range order allows to regard the organized phase as a supersolid [45, 46, 47] akin the proposed two-component systems [48].

4.2. Theoretical Description and Dicke Model

Let us consider a single two-level atom of mass m interacting with a single cavity mode and the standing-wave pump field. The Hamiltonian then reads in a frame rotating with the pump laser frequency ([66] and chapter 2)

$$\begin{aligned}\hat{H}_{(1)} = \frac{\hat{p}_x^2 + \hat{p}_z^2}{2m} &+ V_0 \cos^2(k\hat{z}) + \hbar\eta(\hat{a}^\dagger + \hat{a})\cos(k\hat{x})\cos(k\hat{z}) \\ &- \hbar\Big(\Delta_c - U_0\cos^2(k\hat{x})\Big)\hat{a}^\dagger\hat{a}. \end{aligned} \tag{4.1}$$

Here, the excited atomic state is adiabatically eliminated which is justified for large detuning $\Delta_a = \omega_p - \omega_a$ between the pump laser frequency ω_p and the atomic transition frequency ω_a. The first term describes the kinetic energy of the atom with momentum operators $\hat{p}_{x,z}$. The pump laser creates a standing-wave potential of depth $V_0 = \hbar\Omega_p^2/\Delta_a$ along the z-axis, where Ω_p denotes the maximum pump Rabi frequency, and $\hbar$ the Planck constant. Scattering between the pump field and the cavity mode, which is oriented along x, induces a lattice potential which dynamically depends on the scattering rate and the relative phase between the pump field and the cavity field. This phase is restricted to the values 0 or π, for which the scattering induced light potential has a $\lambda_p/\sqrt{2}$ periodicity along the x-z direction, with $\lambda_p = 2\pi/k$ denoting the pump wavelength (see figure 4.1c). The scattering rate is determined by the two-photon Rabi frequency $\eta = g_0\Omega_p/\Delta_a$, with g_0 being the atom-cavity coupling strength. The last term describes the cavity field, with photon creation and annihilation operators $\hat{a}^\dagger$ and $\hat{a}$. The cavity resonance frequency ω_c is detuned from the pump laser frequency by $\Delta_c = \omega_p - \omega_c$, and the light-shift of a single maximally coupled atom is given by $U_0 = \frac{g_0^2}{\Delta_a}$.

For a condensate of N atoms, the process of self-organization can be captured by a mean-field description [34]. It assumes that all atoms occupy a single quantum state characterized by the wave function ψ, which is normalized to the atom number N. The light-atom interaction can now be described by a dynamic light potential [132] felt by all atoms. Since the timescale of atomic dynamics in the motional degree of freedom is much larger than the inverse of the cavity field decay rate κ, the coherent cavity field amplitude α adiabatically follows the atomic density distribution according to $\alpha = \eta\Theta/(\Delta_c - U_0\mathcal{B} + i\kappa)$. The order parameter describing self-organization is given by $\Theta = \langle\psi|\cos(kx)\cos(kz)|\psi\rangle$ which measures the localization of the atoms on either the even ($\Theta > 0$) or the odd ($\Theta < 0$) sublattice of the underlying checkerboard pattern defined by $\cos(kx)\cos(kz) = \pm 1$ (see figure 4.1c). The sign of the order parameter determines which of the two possible relative phases is adapted by the cavity field. According to the spatial overlap between the atomic density and the cavity mode profile, the atoms dispersively shift the cavity resonance proportional to $\mathcal{B} = \langle\psi|\cos^2(kx)|\psi\rangle$.

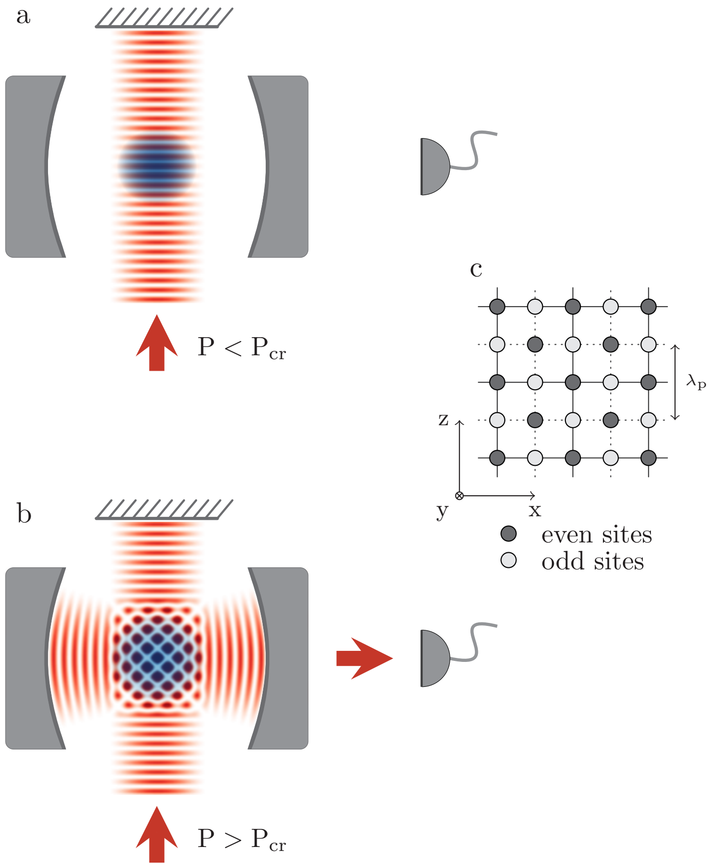

FIGURE 4.1.: Concept of the experiment. A Bose-Einstein condensate which is placed inside an optical cavity is driven by a standing-wave pump laser oriented along the vertical z-axis. The frequency of the pump laser is far red-detuned with respect to the atomic transition line but close detuned to a particular cavity mode. Correspondingly, the atoms coherently scatter pump light into the cavity mode with a phase depending on their position within the combined pump–cavity mode profile. **a**, For a homogeneous atomic density distribution along the cavity axis, the build-up of a coherent cavity field is suppressed due to destructive interference of the individual scatterers. **b**, Above a critical pump power P_{cr} the atoms self-organize onto either the even or odd sites of a checkerboard pattern (**c**) thereby maximizing cooperative scattering into the cavity. This dynamical quantum phase transition is triggered by quantum fluctuations in the condensate density. It is accompanied by spontaneous symmetry breaking both in the atomic density and the relative phase between pump field and cavity field. **c**, Geometry of the checkerboard pattern. The intensity maxima of the pump and cavity field are depicted by the horizontal and vertical lines, respectively, with λ_p denoting the pump wavelength.

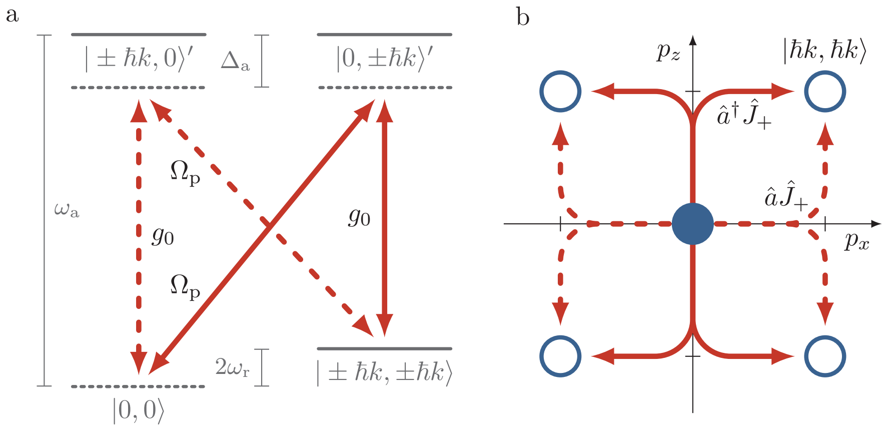

FIGURE 4.2.: Analogy to the Dicke model. In an atomic two-mode picture the pumped BEC–cavity system is equivalent to the Dicke model including counter-rotating interaction terms. **a**, Light scattering between the pump field and the cavity mode induces two balanced Raman channels between the atomic zero-momentum state $|p_x,p_z\rangle = |0,0\rangle$ and the symmetric superposition of the states $|\pm\hbar k,\pm\hbar k\rangle$ with an additional photon momentum along the x and z directions. **b**, The two excitation paths (dashed and solid) corresponding to the two Raman channels are illustrated in a momentum diagram. For the notation see text.

The resulting dynamic lattice potential reads

$$V(x,z) = V_0\cos^2(kz) + \hbar U_0|\alpha|^2\cos^2(kx) + \hbar\eta(\alpha+\alpha^*)\cos(kx)\cos(kz). \tag{4.2}$$

The atoms self-organize due to positive feedback from the interference term in equation (4.2) above a critical two-photon Rabi frequency η_{cr}. Assuming that a density fluctuation of the condensate induces an order parameter, e.g., $\Theta > 0$, and the pump-cavity detuning is chosen to yield $\Delta_c - U_0\mathcal{B} < 0$, the lattice potential resulting from light scattering further attracts the atoms towards the even sites. This in turn increases light scattering into the cavity and starts a runaway process. The system reaches a steady state once the gain in potential energy is balanced by the cost in kinetic energy and collisional energy.

Fundamental insight into the onset of self-organization is gained from a direct analogy to the Dicke model quantum phase transition [1, 19, 20]. This analogy uses a two-mode description for the atomic field, where the initial Bose-Einstein condensate is approximated by the zero-momentum state $|p_x,p_z\rangle = |0,0\rangle$. Photon scattering between the pump and cavity field couples the zero-momentum state to the symmetric superposition of states which carry additional photon momenta along the x and z directions: $|\pm\hbar k,\pm\hbar k\rangle = \sum_{\mu,\nu=\pm1}|\mu\hbar k,\nu\hbar k\rangle/2$. The energy of this state is correspondingly lifted by twice the recoil frequency $\omega_r \equiv E_r/\hbar = \hbar k^2/(2m)$ compared to the zero-momentum state. (For the inclusion of Bloch states, see section 4.5.)

There are two possible paths from the zero-momentum state $|p_x,p_z\rangle = |0,0\rangle$ to the excited momentum state $|\pm\hbar k,\pm\hbar k\rangle$: i) the absorption of a standing-wave pump photon followed by the emission into the cavity, $\hat{a}^\dagger\hat{J}_+$, and ii) the absorption of a cavity photon followed by the emission into the pump field, $\hat{a}\hat{J}_+$ (see figure 4.2b). Here, the collective excitations to the higher-energy mode are expressed by the ladder operators $\hat{J}_+ = \sum_i|\pm\hbar k,\pm\hbar k\rangle_i\,{}_i\langle 0,0| = \hat{J}_-^\dagger$, with the index i labelling the atoms. Including the reverse processes, the interaction

Hamiltonian describing light scattering between pump field and cavity field reads (sec. 4.5)

$$\frac{\hbar\lambda}{\sqrt{N}}(\hat{a}^\dagger + \hat{a})(\hat{J}_+ + \hat{J}_-).$$

This is exactly the interaction Hamiltonian of the Dicke model which describes N two-level systems with transition frequency ω_0 interacting with a bosonic field mode at frequency ω. This system exhibits a quantum phase transition from a normal phase to a superradiant phase once the coupling strength λ between atoms and light reaches the critical value of [19, 20] $\lambda_{\mathrm{cr}} = \sqrt{\omega_0\omega}/2$. Our system realizes the Dicke Hamiltonian with $\omega = -\Delta_c + U_0 N/2$, $\omega_0 = 2\omega_r$ and $\lambda = \eta\sqrt{N}/2$. Correspondingly, the process of self-organization is equivalent to the Dicke quantum phase transition where both the cavity field and the atomic polarization $\langle \hat{J}_+ + \hat{J}_- \rangle = 2\Theta$ acquire macroscopic occupations.

The experimental realization of the Dicke quantum phase transition is usually inhibited because the transition frequencies by far exceed the available dipole coupling strengths. Using optical Raman transitions instead brings the energy difference between the atomic modes from the optical scale to a much lower energy scale, which makes the phase transition experimentally accessible. A similar realization of an effective Dicke Hamiltonian has been theoretically considered using two balanced Raman channels between different electronic (instead of motional) states of an atomic ensemble interacting with an optical cavity and an external pump field [33]. It is important to point out that these systems are externally driven and subject to cavity loss. Therefore they realize a dynamical version of the original Dicke phase transition. However, the cavity output field offers the unique possibility to *in situ* monitor the phase transition as well as to extract important properties of the system [33].

4.3. Observing the Phase Transition

To observe the onset of self-organization in the transversely pumped BEC, we gradually increase the pump power over time while monitoring the light leaking out of the cavity, see figure 4.1 and section 4.5. As long as the pump power is kept below a threshold value no light is detected at the cavity output, and the expected momentum distribution of a condensate loaded into the shallow standing-wave potential of the pump field is observed (see figure 4.3b,c). Once the pump power reaches the critical value an abrupt build-up of the mean intracavity photon number marks the onset of self-organization (see figure 4.3a). Simultaneously, the atomic momentum distribution undergoes a striking change to show additional momentum components at $(p_x, p_z) = (\pm\hbar k, \pm\hbar k)$ (see figure 4.3d). This provides direct evidence for the acquired density modulation along one of the two sublattices of a checkerboard pattern associated with a non-zero order parameter Θ.

Conceptually, the self-organized quantum gas can be regarded as a supersolid [133], similar to those proposed for two-component systems [48]. This requires the coexistence of non-trivial diagonal long-range order corresponding to a periodic density modulation, and off-diagonal long-range order associated with phase coherence. In our system the checkerboard structure of the density modulation is determined by the long-range cavity-mediated atom-atom interactions in a non-trivial way. This is because the arrangement of the atoms is restricted to two possible checkerboard patterns which are intimately linked to the spontaneous breaking of the relative phase between pump and cavity field. In contrast, the spatial atomic structure

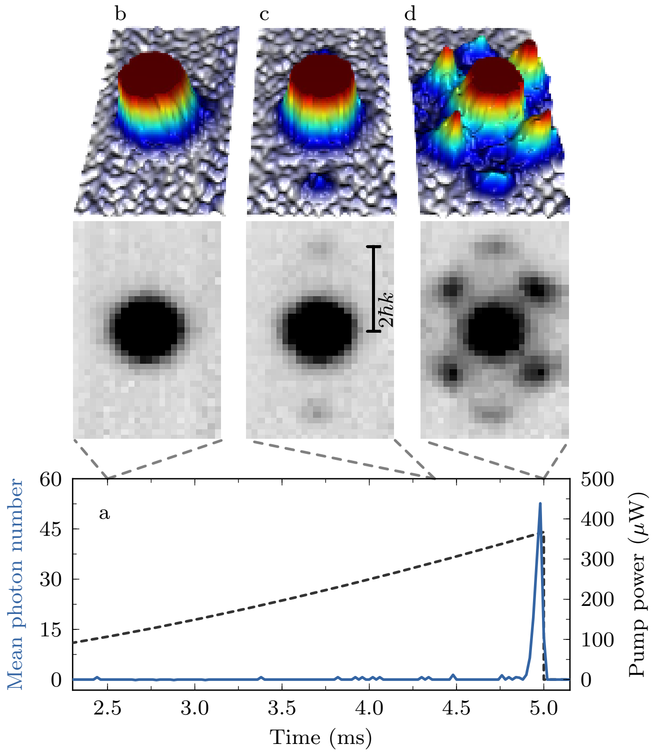

FIGURE 4.3.: Observation of the phase transition. **a**, The pump power (dashed) is gradually increased while monitoring the mean intracavity photon number (solid, binned over 20 μs). After sudden release and subsequent ballistic expansion of 6 ms, absorption images (clipped equally in atomic density) are taken for different pump powers corresponding to lattice depths of: **b**, 2.6 $\mathrm{E_r}$, **c**, 7.0 $\mathrm{E_r}$, **d**, 8.8 $\mathrm{E_r}$. Self-organization is manifested by an abrupt build-up of the cavity field accompanied by the formation of momentum components at $(p_x, p_z) = (\pm\hbar k, \pm\hbar k)$ (**d**). The weak momentum components at $(p_x, p_z) = (0, \pm 2\hbar k)$ (**c**) originate from loading the atoms into the 1D standing-wave potential of the pump laser. The pump-cavity detuning was $\Delta_c = -2\pi \times 14.9(2)$ MHz and the atom number $N = 1.5(3) \times 10^5$.

in traditional optical lattice experiments is solely given by the externally applied light fields (sec. 4.5). In addition, the off-diagonal long-range order of the Bose-Einstein condensate is not destroyed by the phase transition. The atomic coherence length extends over almost the full atomic ensemble, as we deduce from the width of the higher-order momentum peaks.

After crossing the phase transition the system quickly reaches a steady state in the organized phase. As shown by a typical photon trace (figure 4.4a), light is scattered into the cavity for up to 10 ms while the pump intensity is kept constant. This shows that the organized phase is stabilized by scattering induced light forces, which is in strict contrast to previous experiments observing (cavity-enhanced) superradiant light scattering [15, 18] where transfer of momentum on the atomic cloud inhibited a steady state. The overall decrease of the mean cavity photon number for constant pump intensity (figure 4.4a) is attributed to atom loss caused by residual spontaneous scattering at a rate of $\Gamma_{\mathrm{sc}} = 3.7\,/\mathrm{s}$ and backaction-induced heating of the atoms [134]. Atom loss raises the critical pump power according to $P_{\mathrm{cr}} \propto N^{-1}$ which, close to the transition point, explains the reduction of the mean intracavity photon number. This was confirmed by entering the organized phase twice within one run and com-

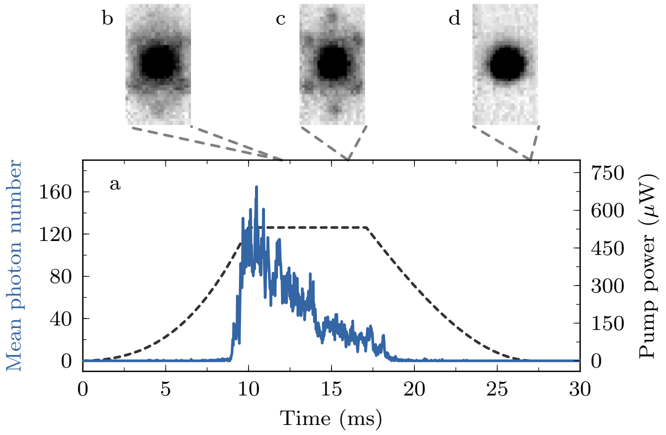

FIGURE 4.4.: Steady state in the self-organized phase. **a**, Pump power sequence (dashed) and recorded mean intracavity photon number (solid, binned over 20 μs). After crossing the transition point at 9 ms, the system reaches a steady state within the self-organized phase. The slow decrease in photon number is due to atom loss (see text). The short-time fluctuations are due to detection shot-noise. **b-d**, Absorption images are taken after different times in the phase: (**b**) 3 ms, (**c**) 7 ms, and (**d**) after lowering the pump power again to zero. The pump-cavity detuning was $\Delta_c = -2\pi \times 6.3(2)$ MHz and the atom number $N = 0.7(1) \times 10^5$.

paring the corresponding critical pump powers of self-organization. From absorption imaging we deduce an overall atom loss of 30% for the pump-power sequence shown in figure 4.4a. Experimentally however, the atom-loss induced photon-number reduction can be compensated for by either steadily increasing the pump intensity or chirping the pump-cavity detuning.

From figure 4.4a we infer a maximum depth of the checkerboard lattice potential of 22 $\mathrm{E_r}$ which corresponds to single-site trapping frequencies of 19 kHz and 30 kHz along the x- and z-direction, respectively. Accordingly, the atoms are confined to an array of tubes which are oriented along the weakly confined y-direction and contain on average a few hundred atoms. Due to the strongly suppressed tunnelling rate between adjacent tubes separated by $\lambda_p/\sqrt{2}$ a dephasing of the different tubes is expected [135]. This is directly observed via the reduced interference contrast in the absorption images reflecting that the supersolid phase evolved into a normal crystalline phase (see figure 4.4b). However, the phase coherence between the tubes is quickly restored when the mean intracavity photon number decreases and the lattice depth correspondingly lowers (see figure 4.4c). After ramping the pump intensity to zero, an almost pure BEC is retrieved (see figure 4.4d).

4.4. Mapping out the Phase Diagram

From the analogy to the Dicke quantum phase transition we can deduce the dependence of the critical pump power on the pump-cavity detuning Δ_c. To experimentally map out the phase boundary we gradually increase the pump power similar to figure 4.3a for different values of Δ_c (see figure 4.5b). The corresponding intracavity photon number traces are shown as a 2D color plot in figure 4.5a.

A sharp phase boundary is observed over a wide range of pump-cavity detuning Δ_c. For large negative values of Δ_c the critical pump power $P_{\mathrm{cr}} \propto \lambda_{\mathrm{cr}}^2$ scales linearly with the effective

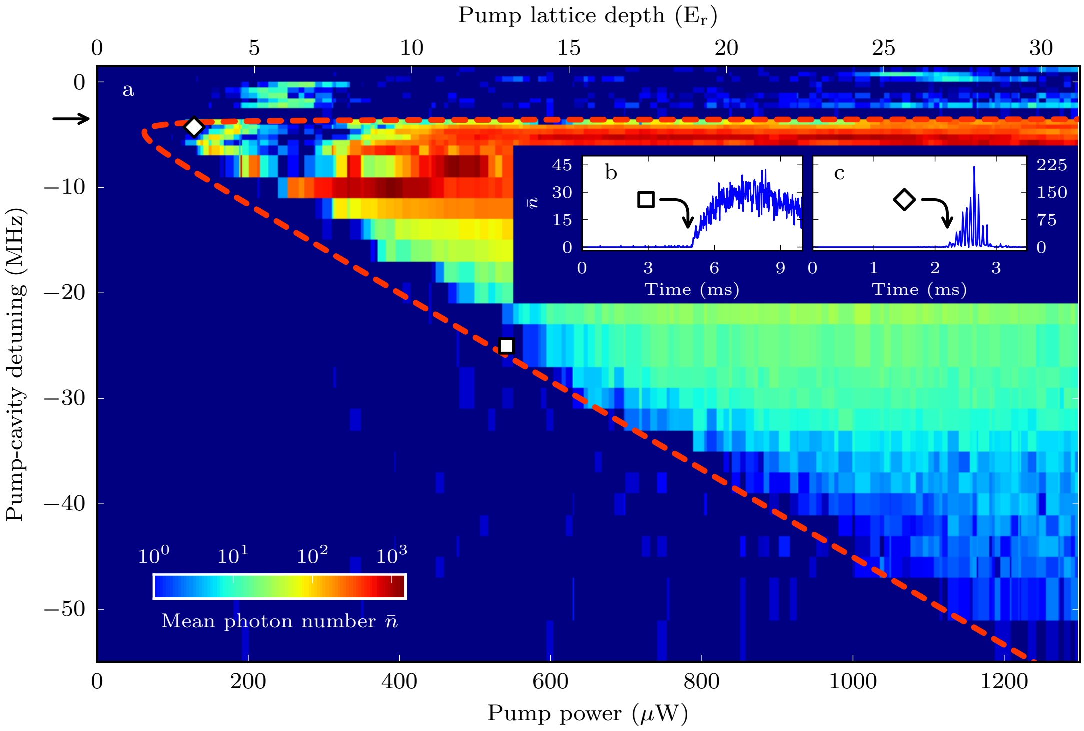

FIGURE 4.5.: Phase diagram. **a**, The pump power is increased to 1.3 mW over 10 ms for different values of the pump-cavity detuning Δ_c. The recorded mean intracavity photon number $\bar{n}$ is displayed in color along the rescaled horizontal axis, showing pump power and corresponding pump lattice depth. A sharp phase boundary is observed over a wide range of the pump-cavity detuning Δ_c, which is in very good agreement with a theoretical mean-field model (dashed curve). The dispersively shifted cavity resonance for the non-organized atom cloud is marked by the arrow. **b-c**, Typical traces showing the intracavity photon number for different pump-cavity detuning: (**b**) $\Delta_c = -2\pi \times 23.0(2)\,\mathrm{MHz}$, binned over $20\,\mu\mathrm{s}$, (**c**) $\Delta_c = -2\pi \times 4.0(2)\,\mathrm{MHz}$, binned over $10\,\mu\mathrm{s}$. The atom number was $N = 1.0(2) \times 10^5$. In the detuning range $-2\pi \times 7\,\mathrm{MHz} \geq \Delta_c \geq -2\pi \times 21\,\mathrm{MHz}$ the pump power ramp was interrupted at $540\,\mu\mathrm{W}$. Therefore, no photon data was taken under the insets.

cavity frequency $\omega = -\Delta_c + U_0\mathcal{B}_0$, which agrees with the dependence expected from the Dicke model (see section 4.5). For $\omega < 0$, the critical coupling strength λ_{cr} has no real solution. Indeed, almost no light scattering is observed if the pump-cavity detuning is larger than the dispersively shifted cavity resonance at $U_0\mathcal{B}_0 = -2\pi \times 3.5\,\mathrm{MHz}$, where $\mathcal{B}_0$ denotes the spatial overlap between the cavity mode profile and the atomic density in the non-organized phase. As the pump-cavity detuning approaches the shifted cavity resonance from below, scattering into the cavity and the intracavity photon number increase.

We quantitatively compare our measurements with the phase boundary calculated in a mean-field description, including the external confinement of the atoms, the transverse pump and cavity mode profiles, and the collisional atom-atom interaction (see section 4.5). The agreement between measurements and theoretically expected phase boundary is excellent (see figure 4.5a, dashed curve).

The organization of the atoms on a checkerboard pattern not only affects the scattering rate between pump and cavity field, but also changes the spatial overlap [95] $\mathcal{B}$. This dynamically shifts the cavity resonance, which goes beyond the Dicke model (see section 4.5), and results in a frustrated system [76] for $U_0 N > \Delta_c > U_0 \mathcal{B}_0$. Here the onset of self-organization brings the coupled atoms-cavity system into resonance with the pump laser, and the positive feedback which drives self-organization is interrupted (see equation (4.2)). This is observed in an oscillatory behavior of the system between the organized and the non-organized phase (see figure 4.5c).

4.5. Methods

Our experimental setup has been described previously [97, 94]. In brief, we prepare almost pure Bose-Einstein condensates of typically 10^5 ^{87}Rb atoms in a crossed-beam dipole trap which is centered inside an ultrahigh-finesse optical Fabry-Pérot cavity. The atoms are prepared in the $|F, m_F\rangle = |1, -1\rangle$ hyperfine ground state, where F denotes the total angular momentum and m_F the magnetic quantum number. Perpendicular to the cavity axis the atoms are driven by a linearly polarized standing-wave laser beam whose wavelength λ_p is red-detuned by 4.3 nm from the atomic D_2 line. The pump-atom detuning is more than five orders of magnitude larger than the atomic linewidth. This justifies that we neglect spontaneous scattering in our theoretical description, and consider only coherent scattering between the pump beam and a particular TEM_{00} cavity mode which is quasi-resonant with the pump laser frequency. The system operates in the regime of strong dispersive coupling [136] where the maximum dispersive shift of the empty cavity resonance induced by all atoms, NU_0, exceeds the cavity decay rate $\kappa = 2\pi \times 1.3\,\mathrm{MHz}$ by a factor of 6.5. The light leaking out of the optical resonator is detected with calibrated single-photon counting modules allowing us to *in-situ* monitor the intracavity light intensity. In addition, we infer about the atomic momentum distribution from absorption imaging along the y-axis after a few milliseconds of ballistic expansion of the atomic cloud.

4.5.1. Experimental Details

We prepare almost pure ^{87}Rb Bose-Einstein condensates in a crossed-beam dipole trap with trapping frequencies of $(\omega_x, \omega_y, \omega_z) = 2\pi \times (252, 48, 238)\,\mathrm{Hz}$, where x denotes the cavity axis and z the pump axis. For a typical atom number of $N = 10^5$ this results in condensate radii of $(R_x, R_y, R_z) = (3.2, 16.6, 3.3)\,\mu\mathrm{m}$ which were deduced in a mean-field approximation [75]. Experimentally, the position of the dipole trap is aligned to maximize the spatial overlap between the BEC and the cavity TEM_{00} mode which has a waist radius of $w_c = 25\,\mu\mathrm{m}$. The cavity has a finesse of 3.4×10^5. Its length of $178\,\mu\mathrm{m}$ is actively stabilized using a weak laser beam at 830 nm which is referenced onto the transverse pump laser [97]. The intracavity stabilization light results in a weak lattice potential with a depth of less than $0.35\,\mathrm{E_r}$.

The pump laser beam has waist radii of $(w_x, w_y) = (29, 53)\,\mu\mathrm{m}$ at the position of the atoms. To accomplish optimal mode matching with the atomic cloud we use the same optical fiber for the pump light and the vertical beam of the crossed-beam dipole trap. The retro-reflected pump power is reduced by a factor of 0.6 with respect to the incoming one due to clipping at the cavity mirrors and losses at the optical elements. All pump powers given in the text refer to the incoming one. The systematic uncertainties in determining the pump intensity at the position of the atoms is estimated to be 20 %. The pump light has a wavelength of $\lambda_p = 784.5\,\mathrm{nm}$ and is linearly polarized along the y-axis (within an uncertainty of 5 %) to optimize scattering into the cavity mode. A weak magnetic field of 0.1 G pointing along the cavity axis provides a quantization axis for the atoms prepared in the $|F, m_F\rangle = |1, -1\rangle$ ground state. Accordingly, only σ_+ or σ_- polarized photons can be scattered into the cavity mode. We observe the onset of self-organization always with σ_+ polarized cavity light since the corresponding atom-cavity coupling strength exceeds the one for σ_- polarized light.

The light which leaks out of the cavity is monitored on two single-photon counting modules each of which is sensitive to one of the two different circular polarizations. In principle this allows to detect single intracavity photons with an efficiency of about 5%. However, for the experiments reported in this work the detection efficiency was reduced by a factor of 10 in order to enlarge the dynamical range of our light detection (limited by the saturation effects of the photon counting modules). The systematic uncertainties in determining the intracavity photon number is estimated to be 25 %.

4.5.2. Mapping to the Dicke Hamiltonian

The onset of self-organization is equivalent to a dynamical version of the normal to superradiant quantum phase transition of the Dicke model. This analogy is derived in a two-mode expansion of the atomic matter field, and allows to infer about properties of the transition into the organized phase.

In the absence of collisional atom-atom interactions the many-body Hamiltonian describing the driven BEC–cavity system is given by

$$\hat{H} = \int \hat{\Psi}^\dagger(x, z)\hat{H}_{(1)}\hat{\Psi}(x, z)\mathrm{d}x\,\mathrm{d}z \tag{4.3}$$

where $\hat{\Psi}$ denotes the atomic field operator, and $\hat{H}_{(1)}$ is the single-particle Hamiltonian given in equation (4.1). In the non-organized phase the mean intracavity photon number vanishes and all atoms occupy the lowest-energy Bloch state ψ_0 of the 1D lattice Hamiltonian $\frac{\hat{p}_z^2}{2m} + V_0\cos^2(k\hat{z})$. Scattering of photons between the pump field and the cavity mode couples the state ψ_0 to the state $\psi_1 \propto \psi_0 \cos(kx)\cos(kz)$ which carries additional $\hbar k$ momentum components along the x and z direction. In order to understand the onset of self-organization we expand the field operator $\hat{\Psi}$ in the reduced Hilbert space spanned by the modes ψ_0 and ψ_1. Note that for describing the deeply organized phase, higher-order momentum states have to be included in the description in order to account for atomic localization at the sites of the emergent checkerboard pattern.

After inserting the expansion $\hat{\Psi} = \psi_0\hat{c}_0 + \psi_1\hat{c}_1$ into the many-body Hamiltonian (see equation (4.3)) we obtain up to a constant term

$$\hat{H}/\hbar = \omega_0\hat{J}_z + \omega\hat{a}^\dagger\hat{a} + \frac{\lambda}{\sqrt{N}}(\hat{a}^\dagger + \hat{a})(\hat{J}_+ + \hat{J}_-) + U_0\mathcal{M}\hat{c}_1^\dagger\hat{c}_1\hat{a}^\dagger\hat{a}, \tag{4.4}$$

with bosonic mode operators $\hat{c}_0$ and $\hat{c}_1$, and the total atom number $N = \hat{c}_0^\dagger\hat{c}_0 + \hat{c}_1^\dagger\hat{c}_1$. Here, the collective spin operators $\hat{J}_+ = \hat{c}_1^\dagger\hat{c}_0 = \hat{J}_-^\dagger$ and $\hat{J}_z = \frac{1}{2}(\hat{c}_1^\dagger\hat{c}_1 - \hat{c}_0^\dagger\hat{c}_0)$ were introduced. Apart from the last term, $\hat{H}$ is the Dicke Hamiltonian [33] which describes the coupling between N two-level systems with transition frequency $\omega_0 = 2\omega_r$ and a bosonic field mode with frequency

$\omega = -\Delta_c + NU_0/2$. Their collective coupling strength is given by $\lambda = \sqrt{N}\eta/2$, which experimentally can be tuned by varying the pump laser power. The last term in equation (4.4) (which is proportional to the matrix element $\mathcal{M} \sim 1$) describes the dynamic (dispersive) shift of the cavity frequency, which is negligible in the close vicinity of the phase transition. Therefore, self-organization of the transversely pumped BEC–cavity system corresponds to the phase transition of the Dicke model from a normal into a superradiant phase [33].

The Dicke Hamiltonian is invariant under the parity transformation [52] $\hat{a} \to -\hat{a}$ and $\hat{J}_\pm \to -\hat{J}_\pm$. This symmetry is spontaneously broken by the process of self-organization corresponding to the atomic arrangement on the even or odd sites of a checkerboard pattern with $\langle \hat{J}_+ + \hat{J}_- \rangle = 2\Theta$ taking either positive or negative values. At the same time the relative phase between the pump and cavity field takes one of two possible values separated by π. This is in contrast to traditional optical lattice experiments where the phase between different laser beams determining their interference pattern is externally controlled [137].

4.5.3. Derivation of the Phase Boundary in a Mean-Field Description

To derive a quantitative expression for the critical pump intensity of self-organization, we perform a stability analysis of the compound BEC–cavity system in a mean-field description, following Ref. [34]. For comparison with our experimental findings we take into account the external trapping potential, the transverse sizes of the cavity mode and the pump beam, as well as collisional atom-atom interactions. The system is described by the generalized Gross-Pitaevskii equation

$$\Big(\frac{\mathbf{p}^2}{2m} + V_{\text{ext}}(\mathbf{r}) + \hbar U_0 |\alpha|^2 \phi_c^2(\mathbf{r}) + \hbar\eta(\alpha + \alpha^*)\phi_c(\mathbf{r})\phi_p(\mathbf{r}) + g|\psi|^2\Big)\psi(\mathbf{r}, t) = \mu\psi(\mathbf{r}, t) \tag{4.5}$$

where $\psi(\mathbf{r})$ denotes the condensate wave function (normalized to the total atom number N), and α denotes the coherent cavity field amplitude which was adiabatically eliminated according to:

$$\alpha = \frac{\eta\Theta}{\Delta_c - U_0\mathcal{B} + i\kappa}.$$

The mode profiles of the cavity and the pump beam are given by $\phi_c(\mathbf{r}) = \cos(kx)e^{-\frac{y^2+z^2}{w_c^2}}$ and $\phi_p(\mathbf{r}) = \cos(kz)e^{-\frac{x^2}{w_x^2}-\frac{y^2}{w_y^2}}$, respectively. The external potential V_{ext} consists of the harmonic trapping potential $m(\omega_x^2 x^2 + \omega_y^2 y^2 + \omega_z^2 z^2)/2$ given by the crossed-beam dipole trap, and the lattice potential $V_0\phi_p^2(\mathbf{r})$ provided by the pump beam. The order parameter $\Theta = \langle\psi|\phi_c\phi_p|\psi\rangle$ and the bunching parameter $\mathcal{B} = \langle\psi|\phi_c^2|\psi\rangle$ are defined according to the main text. The collisional interaction strength is given by $g = \frac{4\pi\hbar^2 a}{m}$ with the s-wave scattering length a. The chemical potential of the condensate is denoted by μ.

A defining condition for the critical two-photon Rabi frequency η_{cr} is obtained from a linear stability analysis of equation (4.5) around the non-organized phase ψ_0 with $\alpha = 0$. Starting with the two-mode ansatz $\psi = \psi_0(1 + \epsilon\phi_c\phi_p)$ with $\epsilon \ll 1$, we carry out an infinitesimal propagation step into imaginary time in equation (4.5). This yields the following condition for the critical pump strength η_{cr} where the system exhibits a dynamical instability

$$\eta_{\text{cr}}\sqrt{N_{\text{eff}}} = \frac{1}{2}\sqrt{\frac{\tilde{\Delta}_c^2 + \kappa^2}{-\tilde{\Delta}_c}}\sqrt{2\omega_r + 4E_{\text{int}}}. \tag{4.6}$$

Here, we introduced the effective number of maximally scattering atoms $N_{\text{eff}} = \langle\psi_0|\phi_c^2\phi_p^2|\psi_0\rangle$, and denoted the detuning between the pump frequency and the dispersively shifted cavity resonance by $\tilde{\Delta}_c = \Delta_c - U_0\mathcal{B}_0$, with $\mathcal{B}_0 = \langle\psi_0|\phi_c^2|\psi_0\rangle$. The interaction energy per particle, given by $E_{\text{int}} = \frac{g}{2\tilde{N}}\int|\psi_0|^4 d\mathbf{r}$, accounts for the mean-field shift of the dispersion relation. Identifying $\omega = -\tilde{\Delta}_c$, $\omega_0 = 2\omega_r + 4E_{\text{int}}$ and $\lambda_{\text{cr}} = \eta_{\text{cr}}\sqrt{N_{\text{eff}}}$ our result agrees with the critical coupling strength λ_{cr} obtained in the Dicke model including cavity decay [33]

$$\lambda_{\text{cr}} = \frac{1}{2}\sqrt{\frac{\omega^2+\kappa^2}{\omega}\omega_0}.$$

The phase boundary shown in figure 4.5a (dashed curve) is obtained from equation (4.6) by approximating the condensate wave function ψ_0 by the Thomas-Fermi solution in the crossed-beam dipole trap [75].

4.6. Conclusions and Outlook

We have experimentally realized a second-order dynamical quantum phase transition in a driven Bose-Einstein condensate coupled to the field of an ultrahigh-finesse optical cavity. At a critical driving strength the steady state realized by the system spontaneously breaks an Ising-type symmetry accompanied by self-organization of the superfluid atoms. We identify regimes where the emergent light-atom crystal is accompanied by phase coherence, and can thus be considered as a supersolid. The process of self-organization is shown to be equivalent to the Dicke quantum phase transition in an open system. We gain experimental access to the phase diagram of the Dicke model by observing the cavity output *in situ*. In a very cold classical gas the corresponding phase boundary is predicted to scale with the temperature instead of the recoil energy [138], and the transition is triggered by classical fluctuations in the atomic density instead of quantum fluctuations.

For the presented experiments the collective interaction λ_{cr} between the induced atomic dipoles and the cavity field approaches the order of the cavity decay rate κ, with a maximum ratio of $\lambda_{\text{cr}}/\kappa = 0.2$. Reaching the regime where the Hamiltonian dynamics dominates the cavity losses offers possibilities to study the coherent dynamics of the Dicke model at the critical point which was shown theoretically to be dominated by macroscopic atom-field and atom-atom entanglement [52, 60, 139]. Detecting the phase of the light leaving the resonator opens the opportunity to study spontaneous symmetry breaking induced by pure quantum fluctuations. Furthermore, recording the statistics of the scattered light may enable quantum non-demolition measurements and the preparation of exotic many-body states [49, 140].

5 Symmetry Breaking at the Dicke Phase Transition

We study symmetry breaking at the Dicke quantum phase transition by coupling a motional degree of freedom of a Bose-Einstein condensate to the field of an optical cavity. Using an optical heterodyne detection scheme we observe symmetry breaking in real-time and distinguish the two superradiant phases. We explore the process of symmetry breaking in the presence of a small symmetry-breaking field, and study its dependence on the rate at which the critical point is crossed. Coherent switching between the two ordered phases is demonstrated.

This chapter is published in reference [3]: K. Baumann, R. Mottl, F. Brennecke, T. Esslinger, *Exploring Symmetry Breaking at the Dicke Quantum Phase Transition*, Phys. Rev. Lett. 107, 140402 (2011).

5.1. Introduction

Spontaneous symmetry breaking at a phase transition is a fundamental concept in physics [85]. At zero temperature, it is caused by the appearance of two or more degenerate ground states in the Hamiltonian. As a result of fluctuations, a macroscopic system evolves into one particular ground state which does not possess the same symmetry as the Hamiltonian. Finding a clean testing ground to experimentally study the process of symmetry breaking is notoriously difficult as external fluctuations and asymmetries have to be minimized or controlled. The protected environment of atomic quantum gas experiments and the increasing control over these systems offer new prospects to experimentally approach the concept of symmetry breaking. Recently, rapid quenches across a phase transition were studied in multi-component Bose-Einstein condensates [141, 142, 143] and optical lattices [144, 145]. Such a non-adiabatic quench causes a response of the system at correspondingly high energies. Therefore, a central characteristic of a phase transition, which is its diverging susceptibility to perturbations, remains partially hidden.

In this work we study the symmetry breaking process while slowly varying a control parameter several times across a zero-temperature phase transition. Compared to quenching, this allows us to explore the low energy spectrum of the system which probes its symmetry most sensitively. For very slow crossing speeds we identify the presence of a residual symmetry breaking field of varying strength. Larger values of this residual field can be correlated to the repeated observation of one particularly ordered state. For increasingly steeper ramps across the phase transition the influence of the symmetry breaking field almost vanishes.

We investigate the symmetry breaking in the motional degree of freedom of a Bose-Einstein condensate coupled to a single mode of an optical cavity. Our system realizes the Dicke model [1, 2, 44] which exhibits a second-order zero-temperature phase transition [19, 20, 22, 55]. The broken symmetry is associated with the formation of one of two identical atomic density waves, which are shifted by half an optical wavelength [2, 44, 35, 36]. Using an interferometric heterodyne technique, we monitor the symmetry-breaking process in real time while crossing the transition point. A similar technique has been used to test self-organization in a classical ensemble of laser-cooled atoms [36], where the symmetric phase is stabilized by thermal energy rather than kinetic energy [34].

5.2. Realizing the Dicke Model

The Dicke model [1] considers the interaction between N two-level atoms and the quantized field of a single-mode cavity, which is described by the Hamiltonian

$$\hat{H} = \hbar\omega_0 \hat{J}_z + \hbar\omega \hat{a}^\dagger \hat{a} + \frac{2\hbar\lambda}{\sqrt{N}}(\hat{a}^\dagger + \hat{a})\hat{J}_x. \tag{5.1}$$

Here, $\hat{a}$ and $\hat{a}^\dagger$ denote the annihilation and creation operators for the cavity mode at frequency ω, and $\hat{\mathbf{J}} = (\hat{J}_x, \hat{J}_y, \hat{J}_z)$ describes the atomic ensemble with transition frequency ω_0 in terms of a pseudospin of length $N/2$. The cavity light field couples with coupling strength λ to the collective atomic dipole $\hat{J}_x$. In the thermodynamic limit, the Dicke model exhibits a zero-temperature phase transition from a normal to a superradiant phase when the control parameter λ exceeds a critical value given by $\lambda_{\mathrm{cr}} = \sqrt{\omega\omega_0}/2$ [19, 20, 22]. Simultaneously, the

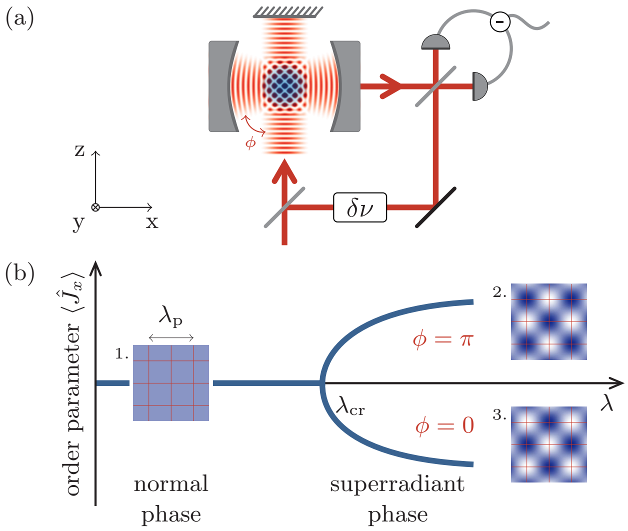

FIGURE 5.1.: (a) Experimental setup. A Bose-Einstein condensate is placed inside an optical cavity and driven by a far-detuned standing-wave laser field (wavelength λ_p) along the z-axis. Phase and amplitude of the intracavity field are measured with a balanced heterodyne setup (PD: photodiodes). (b) Steady-state order parameter $\langle \hat{J}_x \rangle$ as a function of coupling strength λ, with corresponding atomic density distributions (1.-3.). The order parameter vanishes in the normal phase (1.) and bifurcates at the critical point λ_cr, where a discrete $\lambda_\mathrm{p}/2$-spatial symmetry is broken. The two emergent superradiant phases (2. and 3.) can be distinguished via the relative time-phase ϕ.

parity symmetry of the Dicke Hamiltonian, given by the invariance under the transformation $(\hat{a}, \hat{J}_x) \rightarrow (-\hat{a}, -\hat{J}_x)$, is spontaneously broken [55]. While parity is conserved in the normal phase with $\langle \hat{a} \rangle = 0 = \langle \hat{J}_x \rangle$, two equivalent superradiant phases (denoted by even and odd) emerge for $\lambda > \lambda_\mathrm{cr}$, which are characterized by $\langle \hat{J}_x \rangle \lessgtr 0$ and $\langle \hat{a} \rangle \gtrless 0$ (figure 5.1b).

In our experiment [2] we couple motional degrees of freedom of a Bose-Einstein condensate (BEC) with a single cavity mode using a transverse coupling laser (figure 5.1a). Within a two-mode momentum expansion of the matter-wave field, the Hamiltonian dynamics of this system is described by the Dicke model (equation 5.1) [2, 44, 33] where the effective atomic transition frequency is given by $\omega_0 = 2\omega_\mathrm{r}$ with the recoil frequency $\omega_\mathrm{r} = \hbar k^2/2m$, the atomic mass m and the wavelength $\lambda_\mathrm{p} = 2\pi/k$ of the coupling laser. The frequency and power of this laser controls the effective mode frequency ω and the coupling strength λ, respectively [2]. Above a critical laser power, the discrete $\lambda_\mathrm{p}/2$-spatial symmetry, defined by the optical mode structure $u(x,z) = \cos(kx)\cos(kz)$, is spontaneously broken and the condensate exhibits either of two density waves (figure 5.1b). Correspondingly, the atomic order parameter $\langle \hat{J}_x \rangle$, given by the population difference between the even $(u(x,z) > 0)$ and odd $(u(x,z) < 0)$ sublattice, exhibits a negative or positive macroscopic value, while the emergent cavity field oscillates (for $\omega \gg \kappa$) either in $(\phi = 0)$ or out of phase $(\phi = \pi)$ with the coupling laser.

As described previously [2], we prepare BECs of typically 2×10^5 ^{87}Rb atoms in a crossed-beam dipole trap centered inside an ultrahigh-finesse optical Fabry-Pérot cavity, which has a length of $176\,\mu$m. The transverse coupling laser at wavelength $\lambda_\mathrm{p} = 784.5\,$nm is red-detuned by typically ten cavity linewidths $2\kappa = 2\pi \times 2.5\,$MHz from a TEM$_{00}$ cavity mode, realizing

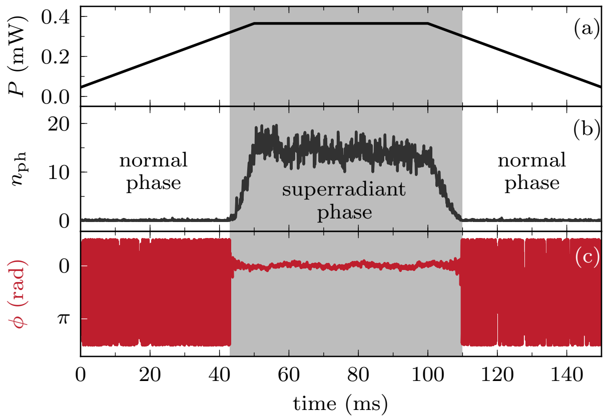

FIGURE 5.2.: Observation of symmetry breaking and steady-state superradiance. Shown are simultaneous traces of (a) the coupling laser power P, (b) the mean intracavity photon number n_{ph}, and (c) the relative time-phase ϕ between coupling laser and cavity field (both averaged over $150\,\mu$s). The coupling laser frequency is red-detuned by 31.3(2) MHz from the empty cavity resonance and the atom number is $2.3(5) \times 10^5$. Residual atom loss causes a slight decrease of the cavity photon number in the superradiant phase.

the dispersive regime $\omega \gg \omega_0$ of the Dicke model. We monitor amplitude and phase of the intracavity field in real-time using a balanced heterodyne detection scheme (figure 5.1a). Due to slow residual drifts of the differential path length of our heterodyne setup, which translate into drifts of the detected phase signal of about 0.1π /s, we cannot relate the phase signals between consecutive experimental runs separated by 60 s.

5.3. Observing Symmetry Breaking

To observe symmetry breaking, we gradually increase the coupling laser power across the critical point (figure 5.2a). The transition from the normal to the superradiant phase is marked by a sharp increase of the mean intracavity photon number (figure 5.2b). Simultaneously, the time-phase ϕ between the two light fields locks to a constant value, implying that the symmetry of the system has been broken (figure 5.2c). The observation of a constant time-phase above threshold confirms that the system reaches a steady-state superradiant phase in which the induced cavity field oscillates at the coupling laser frequency. When lowering the laser power to zero again, the system recovers its initial symmetry and a pure BEC is retrieved, as was inferred from absorption imaging after free ballistic expansion.

To identify the two different superradiant states (figure 5.1b), we cross the phase transition multiple times within one experimental run (figure 5.3a). Above threshold, the corresponding phase signal takes always one of two constant values. From multiple traces of this type we extract a time-phase difference of $1.00(2) \times \pi$ between the two superradiant phases, where the statistical error can be attributed to residual phase drifts of our detection system.

If the system was perfectly symmetric, the two ordered phases would be realized with equal probabilities, when repeatedly crossing the phase transition. However, the presence of any symmetry-breaking field will always drive the system into the same particularly ordered state when adiabatically crossing the critical point. We experimentally quantify the even-odd imbalance by performing 156 experimental runs (similar to figure 5.3a), in each of which the system enters the superradiant phase ten times within 1 s. A measure for the even-odd imbalance is given by the parameter $\epsilon = (m_1 - m_2)/10$, where $m_2 \leq m_1$ denote the number of occurrences of the two superradiant configurations in individual traces. In 73 % of the traces, the system realized ten times the same time-phase, corresponding to the maximum imbalance of $\epsilon = 1$ (figure 5.3b). However, 12 % of the runs exhibited an imbalance below 0.5, which is not compatible with a constant even-odd asymmetry.

We attribute our observations to the finite spatial extension of the atomic cloud. This can result, even for zero coupling λ, in a small, but finite population difference between the even and odd sublattice, determined by the spatial overlap $\mathcal{O}$ between the atomic column density $n(x, z)$ (normalized to N) and the optical mode profile $u(x, z)$. This asymmetry enters the two-mode description (equation 5.1) via the symmetry-breaking term $2\hbar\lambda\mathcal{O}(\hat{a}^\dagger + \hat{a})/\sqrt{N}$, and renormalizes the order parameter $\langle \hat{J}_x \rangle$ by the additive constant $\mathcal{O}$. The resulting coherent cavity field below threshold drives the system dominantly into either of the two superradiant phases, depending on the sign of $\mathcal{O}$. In the experiment, the resulting even-odd imbalance is likely to change between experimental runs, as the overlap integral $\mathcal{O}$ depends λ_p-periodically on the relative position between the mode structure $u(x, z)$ and the center of the trapped atomic cloud, with amplitude $\mathcal{O}_0$. We can exclude a drift of the relative trap position by more than half a wavelength λ_p on the timescale given by our probing time of 1 s, as it would lead to equal probabilities of the two phases, pretending spontaneous symmetry breaking.

The openness of the system gives us direct experimental access to the symmetry-breaking field $\propto \mathcal{O}$. Indeed, we detect a small coherent cavity field ($n_\mathrm{ph} < 0.02$) in the normal phase whose magnitude varies between experimental runs. In all runs with an imbalance of $\epsilon = 1$ (figure 5.3b), the relative time-phases of the cavity field below and above threshold are equal. Furthermore, the even-odd imbalance increases significantly with the light level observed below threshold. Post-selection of those 10 % runs with the smallest light level yields a much smaller imbalance (figure 5.3b, inset).

In general, the influence of a symmetry breaking field becomes negligible, if the mean value of the order parameter, induced by this field, is smaller than the quantum or thermal fluctuations present in the system. From a mean-field calculation performed in the Thomas-Fermi limit for $N = 2 \times 10^5$ harmonically trapped atoms, we estimate a maximum order parameter of $\mathcal{O}_0 = 40$ for zero coupling strength, corresponding to an even-odd population difference of 40 atoms. This value is much smaller than the uncertainty $\Delta J_x = \sqrt{N}/2 = 224$, given by vacuum fluctuations of the excited momentum mode. Therefore, one expects in the extreme case of a sudden quench of the coupling strength beyond λ_cr, that the apparent symmetry is spontaneously broken, resulting in nearly equal probabilities of the two superradiant phases.

5.4. Crossing Rate

In the experiment we determined the even-odd imbalance ϵ for increasingly larger rates $\dot{\lambda}/\lambda_\mathrm{cr}$ at which the critical point was crossed, i.e., in an increasingly non-adiabatic situation (figure 5.3c). As the transition is crossed faster, the mean imbalance between the two superradiant phases decreases significantly and approaches the value $\epsilon \approx 0.25$ corresponding to the balanced situation (figure 5.3c, dashed line). This indicates that the effect of the symmetry breaking term can be overcome by non-adiabatically crossing the phase transition.

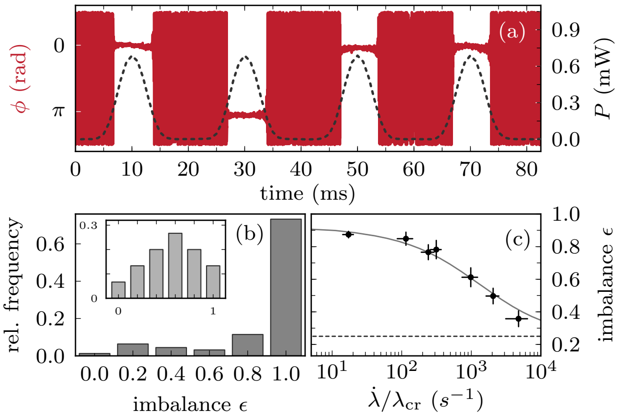

FIGURE 5.3.: (a) Cavity time-phase (red, averaged over $30\,\mu$s) for a single run, and corresponding time sequence of the coupling laser power P (dashed). (b) Probability distribution of the imbalance ϵ (see text) for 156 runs, where the phase transition was crossed at a rate of $\dot{\lambda}/\lambda_{\mathrm{cr}} = 18(3)\,\mathrm{s}^{-1}$. The inset displays the distribution of post-selected data (see text). (c) Mean imbalance (dots) as a function of the rate $\dot{\lambda}/\lambda_{\mathrm{cr}}$ at which the transition was crossed (extracted from 356 runs in total), and theoretical model (solid line). The error bars indicate the standard error of the mean of ϵ and systematic changes of λ_{cr} during probing.

Our observations (figure 5.3c) are in quantitative agreement with a simple model based on the adiabaticity condition known from the Kibble-Zurek theory [146, 147]. We divide the evolution of the system during the increase of the transverse laser power into a quasi-adiabatic regime, where the system follows the change of the control parameter, and an impulse regime, where the system is effectively frozen. After crossing the critical point, fluctuations of the order parameter, which are present at the instance of freezing, become instable and are amplified. The coupling strength which separates the two regimes is determined by Zurek's equation [146] $|\dot{\zeta}/\zeta| = \Delta/\hbar$, with $\zeta = (\lambda_{\mathrm{cr}} - \lambda)/\lambda_{\mathrm{cr}}$ and the energy gap between ground and first excited state given by $\Delta = \hbar\omega_0\sqrt{1 - \lambda^2/\lambda_{\mathrm{cr}}^2}$ for $\omega \gg \omega_0$ [55, 33].

We deduce the probability with which the system chooses the even phase, $p_{\mathrm{even}} = \int_0^\infty p(\Theta)\mathrm{d}\Theta$, from the probability distribution $p(\Theta)$ at the instance of freezing, where $\hat{\Theta}$ denotes the shifted dipole operator $\hat{\Theta} = \hat{J}_x + \mathcal{O}$. In the thermodynamic limit the distribution $p(\Theta)$ becomes Gaussian with a mean value $\langle\hat{\Theta}\rangle = \langle\hat{J}_x\rangle + \mathcal{O}$ and a width determined by the quantum fluctuations of the order parameter ΔJ_x. These values are determined from the linear quantum Langevin equations based on the Dicke model [33] including the symmetry breaking term. Besides the decay of the cavity field we also take into account dissipation of the excited momentum state at a rate $\gamma = 2\pi \times 0.6\,\mathrm{kHz}$. This value was deduced from independent measurements of the cavity output field below threshold.

From the steady-state solution of the quantum Langevin equations we find that the mean order parameter $\langle\hat{\Theta}\rangle$ grows faster in λ than its fluctuations. If $\mathcal{O} > 12$ the order parameter exceeds its uncertainty already below critical coupling. Thermal fluctuations are neglected in this analysis. For our typical condensate temperatures of about 100 nK quantum fluctuations dominate as long as $\zeta > 0.005$. We account for shot-to-shot fluctuations of the overlap $\mathcal{O}$ by suitably averaging over the position of the harmonic trap. The solid line in figure 5.3c shows a least square fit of our model to the data with the single free parameter $\mathcal{O}_0$. We obtain

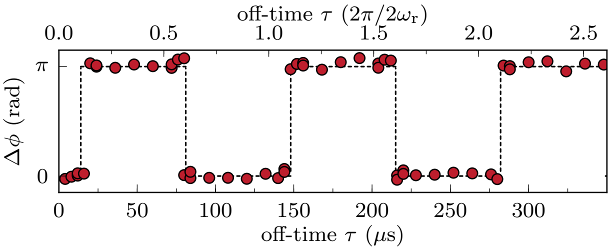

FIGURE 5.4.: Coherent switching between the two ordered phases. After adiabatically preparing the system in one of the two superradiant phases, the coupling field is turned off for a time τ. Displayed is the steady-state cavity time-phase $\Delta\phi$ (averaged over 0.5 ms) after turning on the coupling field, referenced to the value recorded before the turning-off. Each data point corresponds to a single measurement. The dashed line shows the time evolution as expected from the two-mode model.

a value of $\mathcal{O}_0 = 77$ which is in reasonable agreement with the theoretically expected value of $\mathcal{O}_0 = 40$. This verifies the predominance of the considered symmetry breaking field over other possible noise terms.

5.5. Coherent Switching

Finally, we experimentally demonstrate coherent switching between the two ordered states. To this end we suddenly turn off the coupling laser field after adiabatically preparing the system in one of the two superradiant phases. The atoms are then allowed to freely evolve according to their momentum state occupation, giving rise to standing-wave oscillations of the atomic density distribution. In the two-mode description this corresponds to harmonic oscillations of the order parameter $\langle \hat{J}_x \rangle$ at frequency $2\omega_\mathrm{r}$. We probe this time evolution by turning on the coupling laser after a variable off-time τ, thereby deterministically re-trapping the atoms either in the initial or in the opposite superradiant state. As expected, we observe regular π-jumps in the difference $\Delta\phi$ between the steady-state phase signals measured before and after the free evolution, with a frequency of $2\omega_\mathrm{r}$ (figure 5.4, dashed line). The inertia of the atoms traveling at finite momentum causes the π-jumps in figure 5.4 to occur before those times at which the order parameter has evolved by an odd number of quarter periods.

6 Dynamical Coupling of a BEC and a Cavity Lattice

The physical phenomena discussed in the following chapter are performed driving the cavity directly without using a transverse pumping field. The underlying Hamiltonian description is still given by equation 2.9, which also described atomic self-organization and formed the basis for the mapping to the Dicke model.

Changing the pumping geometry shows a drastic impact on the observed physics: the BEC coupled the cavity does not show a phase transition. The system is however still governed by strong interactions between the atomic motion and the light field even at the level of single quanta. While coherently pumping the cavity mode the condensate is subject to the cavity optical lattice potential whose depth depends nonlinearly on the atomic density distribution. We observe optical bistability already below the single photon level and strong back-action dynamics which tunes the coupled system periodically out of resonance.

This chapter is published in reference [96]: S Ritter, F. Brennecke, K. Baumann, T. Donner, C. Guerlin, T. Esslinger, *Dynamical Coupling between a Bose-Einstein Condensate and a Cavity Optical Lattice*, Applied Physics B 95(2), 213 (200).

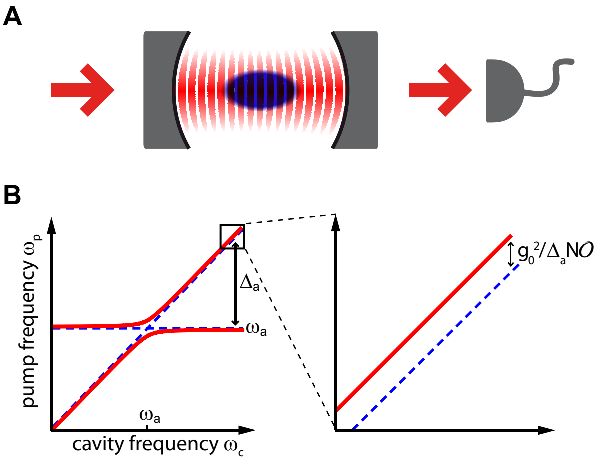

FIGURE 6.1.: **A.** Sketch of the coupled BEC-cavity system. To study the nonlinear coupling between condensate and cavity light field the cavity mode is coherently driven by a pump laser while the transmitted light is monitored on a single photon counter. **B.** Energy diagram of the coupled system. We work in the dispersive regime where the pump laser frequency ω_p is far detuned from the atomic transition frequency ω_a. The collective coupling between BEC and cavity mode leads to dressed states (solid). In the dispersive regime their energy is shifted with respect to the bare state energies (dashed) by an amount which depends on the spatial overlap $\mathcal{O}$ between the cavity mode and the atomic density distribution. Correspondingly, the condensate is subject to a dynamical lattice potential whose depth depends non-locally on the atomic density distribution.

6.1. Introduction

The coherent interaction between matter and a single mode of light is a fundamental theme in cavity quantum electrodynamics [148]. Experiments have been realized both in the microwave and the optical domain, with the cavity field being coupled to Rydberg atoms [149, 150], neutral atoms [151, 152], ions [153] or artificial atoms like superconducting qubits [30]. The energy spectrum of these systems is characterized by an avoided crossing between the atomic and cavity excitation branches. Far detuned from the atomic resonance the dispersive regime is realized. The atom-light coupling then predominantly affects the motional degrees of freedom of the atoms through the dipole force. In turn, the atoms induce a phase shift on the cavity field which depends on their spatial position within the cavity mode. This regime has been investigated both with single atoms strongly coupled to optical cavities [154, 155] and with cold,ultracold and condensed ensembles of atoms collectively coupled to large volume cavities [39, 156, 36, 136, 18].

Access to a new regime has recently been attained by combining small volume ultra-high finesse optical cavities with ultracold atomic ensembles [41, 134] and Bose-Einstein condensates (BEC) [94, 42, 95]. Here a very strong coupling to the ensemble is achieved and the light forces significantly influence the motion of the atoms already at the single photon level. In turn, the atoms collectively act as a dynamical index of refraction shifting the cavity resonance according to their density distribution. Atomic motion thus acts back on the intracavity light intensity, providing a link to cavity optomechanics [157, 158, 159, 160, 161, 162, 163, 164, 165, 166]. Recently, bistability at photon numbers below unity [41], measurement back-action [134], and triggered coherent excitations of mechanical motion [95] have been observed.

Here, we further investigate the steady state and non-steady state aspects of this highly nonlinear regime including bistability and coherent oscillations. We present experimental observations and compare them with ab-initio calculations in a mean-field approximation.

6.2. Experimental setup

In our setup a ^{87}Rb BEC is coupled dispersively to an ultra-high finesse Fabry-Pérot optical cavity [94] (figure 6.1A). The atoms are trapped inside the cavity within a crossed beam dipole trap formed by two far-detuned laser beams oriented perpendicularly to the cavity axis. The trapping frequencies are $(\omega_x, \omega_y, \omega_z) = 2\pi \times (220, 48, 202)\,\mathrm{Hz}$ where x denotes the cavity axis and z the vertical axis. The BEC contains typically $N = 10^5$ atoms, which corresponds to Thomas-Fermi radii of (R_x, R_y, R_z)= (3.2, 19.3, 3.4) μm.

The atoms are prepared in the sub-level $|F, m_F\rangle = |1, -1\rangle$ of the $5S_{1/2}$ ground state manifold, where F denotes the total angular momentum and m_F the magnetic quantum number. The atomic D_2 transition couples to a TEM_{00} mode of the cavity with bare frequency ω_c corresponding to a wavelength of $\lambda = 780\,\mathrm{nm}$. The mode has a waist radius of 25 μ m and is coherently driven at amplitude η through one of the cavity mirrors with a circularly polarized pump laser at frequency ω_p. For the experiments reported here, the pump laser was blue-detuned by $2\pi \times 58\,\mathrm{GHz}$ from the atomic transition frequency ω_a. Due to a weak magnetic field oriented along the cavity axis pump photons couple only to σ^+ transitions. Summing over all accessible hyperfine levels we obtain a maximum coupling strength between a single atom and a σ^+ polarized intracavity photon of $g_0 = 2\pi \times 14.1\,\mathrm{MHz}$. This is larger than the cavity decay rate $\kappa = 2\pi \times 1.3\,\mathrm{MHz}$ and the atomic spontaneous emission rate $\gamma = 2\pi \times 3.0\,\mathrm{MHz}$. Therefore the condition of strong coupling is fulfilled even at the single atom level.

A piezo actuator between the cavity mirrors allows us to actively stabilize the cavity length ($\approx 178\,\mu$ m) via a Pound-Drever-Hall lock onto a far detuned laser at 829 nm that is tuned to resonance with a different longitudinal cavity mode. The corresponding weak standing wave potential inside the cavity has no significant influence on the results presented here.

6.3. Theoretical description

Since the detuning $\Delta_a = \omega_p - \omega_a$ between pump laser frequency and atomic transition frequency is large compared to the collective coupling strength $\sqrt{N} g_0$ and the spontaneous emission rate γ, the population of the atomic excited state is small [167]. This allows us to neglect spontaneous emission, and to eliminate the atomic excited state [66] from the Tavis-Cummings Hamiltonian which describes the collective coupling between N atoms and the cavity field [168]. The coupling induces a light shift of the atomic ground state energy and a collective phase shift of the cavity light field (figure 6.1B). This results in an one-dimensional optical lattice potential $\hbar U_0 \cos^2(kx)$ with the atom-light coupling varying along the cavity axis as $g_0 \cos(kx)$. Here, $U_0 = g_0^2/\Delta_a$ denotes the light shift of a maximally coupled atom in the presence of a single cavity photon, with $k = 2\pi/\lambda$. For our parameters this lattice depth

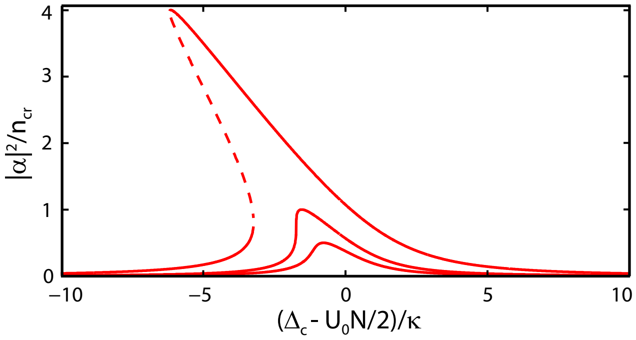

FIGURE 6.2.: Mean intracavity photon number $|\alpha|^2$ of the pumped BEC-cavity system versus the cavity-pump detuning Δ_c calculated for three different pump strengths $\eta = (0.7, 1, 2)\eta_{\mathrm{cr}}$ (bottom to top curve). The blue-detuned cavity light field pushes the atoms to regions of lower coupling strength which gives rise to bistability. The initially symmetric resonance curve centered around $\Delta_c = U_0N/2$ develops above a critical pump strength η_{cr} a bistable region with two stable (solid lines) and one unstable branch (dashed).

is comparable to the recoil energy $\hbar\omega_{\mathrm{rec}} = \hbar^2k^2/(2m)$, i.e., already mean intracavity photon numbers on the order of one are able to significantly modify the atomic density distribution. In turn, the intracavity light intensity of the driven system itself depends on the spatial distribution of the atoms in the cavity mode. The overall frequency shift of the cavity resonance is determined by the spatial overlap $\mathcal{O}$ between atomic density and cavity mode profile. Correspondingly, the coupled BEC-cavity system is governed by a strong back-action mechanism between the atomic external degree of freedom and the cavity light field.

To describe the BEC-cavity dynamics quantitatively we use an one-dimensional mean field approach. Light forces of the cavity field affecting the transverse degrees of freedom can be neglected for low intracavity photon numbers. With ψ denoting the condensate wave function along the cavity axis (normalized to unity) and α the coherent state amplitude of the cavity field, the equations of motion read [169]

$$\begin{aligned} i\hbar\dot{\psi}(x,t) &= \Big(\frac{-\hbar^2}{2m}\frac{\partial^2}{\partial x^2} + |\alpha(t)|^2\hbar U_0\cos^2(kx) \\ &\quad + V_{\mathrm{ext}}(x) + g_{1\mathrm{D}}|\psi|^2\Big)\psi(x,t) \qquad (6.1) \\ i\dot{\alpha}(t) &= -(\Delta_c - U_0N\mathcal{O} + i\kappa)\alpha(t) + i\eta. \qquad (6.2) \end{aligned}$$

Here, V_{ext} denotes the weak external trapping potential, N is the total number of atoms, $g_{1\mathrm{D}}$ the atom-atom interaction strength integrated along the transverse directions, and $\Delta_c = \omega_p - \omega_c$ denotes the cavity-pump detuning.

These coupled equations of motion reflect that the depth of the cavity lattice potential, which is experienced by the atoms, depends non-locally on the atomic state ψ via the overlap $\mathcal{O} = \langle\psi|\cos^2(kx)|\psi\rangle$. To get insight into the steady-state behavior of the condensate in this dynamical lattice potential we first solve equation (6.1) for the lowest energy state in case of a fixed lattice depth. Starting from the variational ansatz

$$\psi(x) = c_0 + c_2\sqrt{2}\cos(2kx) \qquad (6.3)$$

which is appropriate for moderate lattice depths, we find the overlap integral in the ground state to be $\mathcal{O} = \frac{1}{2} - \frac{|\alpha|^2 U_0}{16\omega_{\mathrm{rec}}}$. Here, the external trapping potential V_{ext} and atom-atom interactions have been neglected for simplicity. Correspondingly, the BEC acts as a Kerr medium that shifts the empty cavity resonance proportionally to the intracavity light intensity. After inserting this result into the steady state solution of equation (6.2)

$$|\alpha|^2 = \frac{\eta^2}{\kappa^2 + (\Delta_c - U_0 N \mathcal{O})^2},$$

an algebraic equation of third order in $|\alpha|^2$ is obtained which determines the resonance curve of the system. For sufficient pump strength η the system exhibits bistable behavior (figure 6.2), a property which is known from optical and mechanical Kerr nonlinearity [170, 171, 172, 173, 39, 41]. Namely, while increasing the pump strength η the initially Lorentzian resonance curve of height η^2/κ^2 gets asymmetric and develops an increasing region with three possible steady states above a critical value η_{cr}. A detailed analysis results in a corresponding critical intracavity photon number on resonance of $n_{\mathrm{cr}} = \frac{8}{3\sqrt{3}} \frac{16\kappa\omega_{\mathrm{rec}}}{N U_0^2}$.

6.4. Bistability measurement

To study the nonlinear coupling between BEC and cavity field experimentally, the pump laser frequency was scanned slowly (compared to the atomic motion) across the resonance while recording the cavity transmission on a single photon counter. From the measured photon count rate the mean intracavity photon number is deduced by correcting for the quantum efficiency (≈ 0.5) and the saturation of the single photon counter, and by taking into account the transmission (2.3 ppm) of the output coupling mirror as well as the losses at the detection optics (15 %). The systematic uncertainty in determining the intracavity photon number is estimated to be 25 %.

Typical resonance curves obtained for different pump strengths are shown in figure 6.3. For maximum intracavity photon numbers well below the critical photon number n_{cr} the resonance curve is Lorentzian shaped and does not depend on the scan direction of the pump laser (A). When increasing the pump strength beyond the critical value we observe a pronounced asymmetry of the resonance and hysteretic behavior which indicates bistability of the system (B). The frequency range over which bistability occurs gets enlarged by further increasing the pump strength (C).

We compare our experimental data with resonance curves obtained from a numerical solution of the coupled set of equations (6.1) and (6.2) including atom-atom interactions and the external trapping potential (red lines in figure 6.3). We find a critical photon number of $n_{\mathrm{cr}} = 0.21$, in accordance with our experimental observations within the systematic uncertainties. The inclusion of atom-atom interactions results in a critical photon number which is slightly larger than the value 0.18 obtained from the analytical interaction-free model. For very low photon numbers (A and B) we find good agreement between the measured and calculated resonance curves. However, for increasing pump strengths we observe that the system deviates more and more from the calculated steady state curves (C). This is visible in a precipitate transition from the upper branch to the lower one while scanning with decreasing Δ_c. Such deviations indicate a superposed non-steady state dynamics. This dynamics is governed by the inertia of our refractive index medium, and goes beyond the physics of a

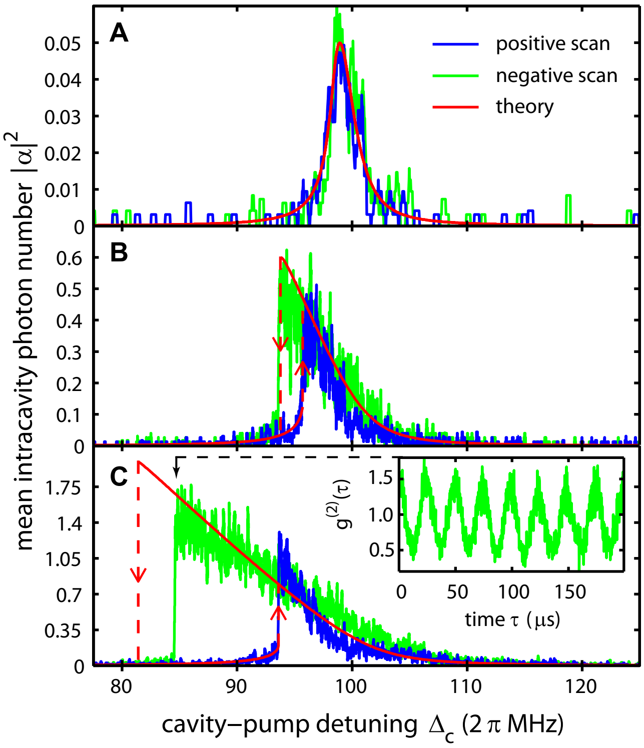

FIGURE 6.3.: Bistable behavior at low photon number. The traces show the mean intracavity photon number $|\alpha|^2$ versus the cavity-pump detuning Δ_c. Traces A, B and C correspond to pump strengths of $\eta = (0.22, 0.78, 1.51)\kappa$, respectively. The intracavity photon number is deduced from the detector count rate. Each graph corresponds to a single experimental sequence during which the pump laser frequency was scanned twice across the resonance, first with increasing detuning Δ_c (blue curve) and then with decreasing detuning (green curve). The scan speed was $2\pi \times 1\,\mathrm{MHz/ms}$ and the raw data has been averaged over $400\,\mu$ s (A) and $100\,\mu$ s (B and C). We corrected for a drift of the resonance caused by a measured atom loss rate of 92/ms assumed to be constant during the measurement. The theoretically expected stable resonance branches (red) have been calculated for 10^5 atoms (deduced from absorption images) taking a transverse part of the mode overlap of 0.6 into account. This value was deduced from several scans across the resonance in the non-bistable regime and is about 25% below the value expected from the BEC and cavity mode geometry. Shot-to-shot fluctuations in the atom number resulting in uncontrolled frequency shifts were corrected for by overlapping the individual data traces A,B and C with the theoretically expected curves. The inset of C shows photon-photon correlations of the green trace calculated from the last $400\,\mu$ s right before the system transits to the lower stable branch. Due to averaging these oscillations are not visible in the main graph.

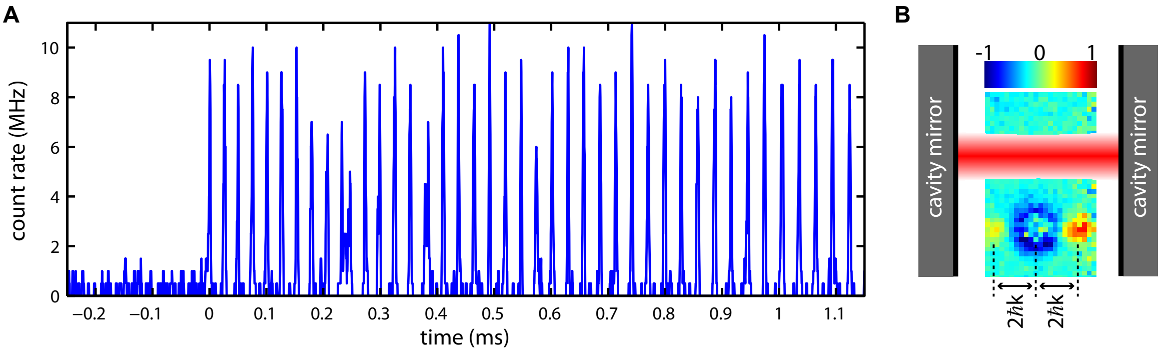

FIGURE 6.4.: **A.** Coherent dynamics of the BEC in the dynamical lattice potential. Shown is the count rate of the single photon detector while scanning with increasing cavity-pump detuning across the bistable resonance curve. The scan speed was set to $2\pi \times 2\,\mathrm{MHz/ms}$ with a maximum intracavity photon number of 9.5. The condensate is excited due to the non-adiabatic branch transition resulting in oscillations of the overlap $\mathcal{O}$ clearly visible in a periodic cavity output. **B.** Absorption image revealing the population in the $|p = \pm 2\hbar k\rangle$ momentum components during the coherent oscillations. Once the coherent dynamics was excited both trapping potential and pump laser were switched off and the cloud was imaged after 4 ms free expansion. To clearly detect the small $|p = \pm 2\hbar k\rangle$ population we averaged over 9 independent images and subtracted the average of 9 different images without excitation (taken after the oscillations had stopped [95]).

pure Kerr medium [174]. Experimentally, this is supported by detecting regular oscillations in the second order correlation function $g^{(2)}(\tau)$ which was evaluated from the transmission signal right before the system leaves the upper resonance branch (figure 6.3C inset).

6.5. Dynamics

Coherent non-steady state dynamics of the system can also be excited more directly by means of a non-adiabatic increase in the cavity light intensity. This is naturally provided by the sudden transition which appears while scanning with increasing Δ_c across the bistable resonance (figure 6.4A). Once the system reaches the turning point of the lower stable branch (figure 6.2) a periodic dynamics is excited which gets observable through a strongly pulsed cavity transmission. This dynamics has been reported on previously [95]. In short, a small fraction of condensate atoms is scattered by the cavity lattice into the higher momentum states $|p = \pm 2\hbar k\rangle$. Due to matter-wave interference with the remaining $|p = 0\rangle$ atoms the atomic cloud develops a density oscillation which shifts the system periodically in resonance with the pump laser. Direct evidence for the coherence of this dynamics is obtained via the atomic momentum distribution from absorption imaging (figure 6.4B).

Further insight into the non-steady state behavior can be gained from the analogy between the coupled BEC-cavity system and a mechanical oscillator coupled to a cavity field via radiation pressure [95]. The mechanical oscillator can be identified with the c_2-mode in the state expansion equation (6.3). Matter-wave interference with the c_0-mode gives rise to a spatial modulation of the atomic density, and results in harmonic oscillations of the overlap $\mathcal{O}$ at a frequency of $4\omega_{\mathrm{rec}} \approx 2\pi \times 15\,\mathrm{kHz}$.

This mapping to cavity optomechanics shown in [95] helps to gain knowledge on the dynamical behavior of the system. Since the mechanical oscillator is subject to the radiation pressure force its stiffness is modified according to the intracavity light intensity. This mechanism is known in the literature as 'optical spring' [171, 175]. We observe a clear signature of this effect in the photon-photon correlations (figure 6.3C inset) oscillating at approximately 42 kHz which is a factor of 2.9 larger than the bare oscillator frequency. A detailed study of this dynamics including the amplification effects due to retardation between cavity light field and oscillator motion is the subject of ongoing work.

6.6. Conclusion

Here we have studied the dynamical coupling between a BEC and a cavity optical lattice. We have observed a strong optical nonlinearity at the single photon level, manifested by bistable behavior and coherent oscillations around the steady state. These results complement the cavity optomechanical studies traditionally conducted on microfabricated or high precision interferometric devices (for a recent review see [176]). Our system has remarkable properties which should allow us to experimentally explore the quantum regime of cavity optomechanics [176, 177]. The mechanical oscillator intrinsically starts in the ground state, from which, due to collective enhancement of the coupling, a single motional excitation can cause a shift of the cavity resonance on the order of the cavity linewidth. Inversely, a change of one photon in the light field strongly modifies the atomic motional state. Beyond the classical nonlinear observations reported here, the system is therefore promising to reveal signatures of the quantum nature of the light and matter fields [134, 177, 178].

7 Conclusions and Outlook

In this thesis, the first experimental realization of the Dicke quantum phase transition was presented. We have achieved this long-standing experimental goal by employing atomic momentum states of a Bose-Einstein Condensate (BEC) dispersively coupled to a high-finesse optical cavity [2]. This enables a light-matter coupling strength larger than the elementary energy of an atomic or photonic excitation. We have observed spontaneous self-organization of the atoms on a checkerboard pattern when sufficiently driven by a transverse laser field. The theoretical equivalence of the BEC self-organization and the zero-temperature Dicke phase transition was shown. Conceptually, the phase transition is driven by infinite-range interactions between the atoms which are mediated by the cavity field. The phase boundary of the superradiant phase was mapped out in quantitative agreement with the model description. We have demonstrated controlled crossing of the phase transition making it possible to enter the ordered phase and subsequently recover a BEC again. We have further investigated the symmetry-breaking process and identified a residual symmetry-breaking field, caused by the finite spatial extension of our system [3]. By varying the rate, at which the critical point is crossed, we can approach a symmetric regime, where both symmetry-broken states appear with equal probability.

Ongoing experimental work focuses on precursors of the Dicke phase transition below threshold. We have recently spectroscopically mapped out the mode softening in the excitation energy spectrum towards the critical point. The characteristic momentum selectivity of the infinite-range interaction modifies excitations at distinct momenta, in close analogy to the physics of a roton minimum. We have further observed an increasing susceptibility upon density fluctuations when approaching the critical point. The cavity output field, due to these density fluctuations, reveals an incoherent population of the cavity mode and an oscillating second-order correlation function. By comparing the experimental data with a quantum statistical model we have identified a regime, in which quantum fluctuations dominate the dynamics of the system.

The experimental setup gives us many opportunities and possibilities for the future. One exciting aspect of the system is the dynamics at the Dicke phase transition, as strict adiabaticity can not be met experimentally when approaching the critical point. A perfect adiabatic process in finite time at the critical point is forbidden due to the vanishing excitation-energy gap. The resulting state after crossing the critical point consequently shows excess energy, corresponding to the formation of defects. The Kibble-Zurek theory [179, 146] gives a good estimation of the defect production rate. Our system potentially allows to detect these defects via either the atomic momentum distribution or real-time detection of the cavity-output field. Recently, concepts of quantum optimal-control theory, which is the study of optimization strategies to improve the outcome of a quantum process, have been successfully applied to many-body systems [180, 181, 182]. The dynamical crossing of a quantum phase transition under optimal control conditions is however still experimentally unexplored.

Cavity loss, inevitable from an experimental point of view, allows us to infer about the many-body system inside the cavity in real time without disturbing the system. Mekhov et al. have shown theoretically, that the atomic quantum statistics is mapped to the cavity field via atom-light interactions [49]. Transverse light scattering is thus an excellent tool to study complex many-body phenomena such as the superfluid to Mott-insulating phase transition of ultracold atoms in an optical lattice [123]. Implementing a three dimensional optical lattice inside our cavity might allow us to non-destructively monitor this phase transition in real time and possibly study the quantum critical region, where quantum fluctuations dominate the dynamics of the system. It would also enable us to go beyond pure Bose-Hubbard physics. By tuning the light-matter interaction strength, we can engineer a hybrid system, where both Bose-Hubbard type physics and self-organization physics become equally relevant. An interplay of short-ranged interaction, due to atomic s-wave scattering, and infinite-ranged interaction, due to the cavity mode, will certainly generate a rich many-body phase diagram.

The ultimate control over all atomic degrees of freedom achieved in a BEC combined with the clean electromagnetic environment in a high-finesse optical cavity provides an ideal playground to study a plethora of quantum many-body phenomena. We have demonstrated, that we can explore general physical concepts beyond the field of ultracold atoms. Minor experimental changes allow us to explore strongly-correlated atomic phases that are governed by infinite-range interactions, with an detection method allowing for non-destructive and real-time observation of quantum many-body dynamics.

A Rotating-Frame Transformation

In this appendix we present the technical details on transforming Hamiltonian (2.1) into the interaction picture [183]. The transformation is used twice in a similar fashion in this thesis: the rotating-wave approximation is applied in section 2.1.2 after transforming into a the frame rotating with the pump frequency. Explicit time dependencies are further eliminated in section 2.1.3 by transforming into a rotating frame. We start by repeating the Hamiltonian (2.1) (for the individual terms see section 2.1.1)

$$\hat{\mathcal{H}} = \hbar\omega_\mathrm{c}\hat{a}^\dagger\hat{a} + \hbar\omega_\mathrm{a}\hat{\sigma}_+\hat{\sigma}_- + \hbar g_0\left(\hat{\sigma}_+ + \hat{\sigma}_-\right)\left(\hat{a} + \hat{a}^\dagger\right).$$

The Hamiltonian (2.1) is split into $\hat{\mathcal{H}} = \hat{\mathcal{H}}_0 + \hat{\mathcal{H}}_1$ where $\hat{\mathcal{H}}_0 = \hat{\mathcal{H}}_\mathrm{a} + \hat{\mathcal{H}}_\mathrm{c}$ describes the bare cavity and atoms and $\hat{\mathcal{H}}_1 = \hat{\mathcal{H}}_\mathrm{int}$ describes the interaction. We introduce the transformation operator

$$\begin{aligned}
\hat{U}(t) &= \exp\left(i\hat{\mathcal{H}}_0 t/\hbar\right) = \exp\left(i\omega_\mathrm{a}t\hat{\sigma}_+\hat{\sigma}_- + i\omega_\mathrm{c}t\hat{a}^\dagger\hat{a}\right)\\
&= \underbrace{\exp(i\omega_\mathrm{a}t\hat{\sigma}_+\hat{\sigma}_-)}_{\hat{U}_1(t)}\underbrace{\exp(i\omega_\mathrm{c}t\hat{a}^\dagger\hat{a})}_{\hat{U}_2(t)} = \hat{U}_1(t)\hat{U}_2(t).
\end{aligned}$$

With this definition, the commutator $\left[\hat{U}_1, \hat{U}_2\right] = 0$ vanishes. An operator in the Schrödinger picture $\hat{\mathcal{A}}_\mathrm{S}$ is transformed into an operator $\hat{\mathcal{A}}_\mathrm{I}$ in the interaction picture via the operation $\hat{\mathcal{A}}_\mathrm{I} = \hat{U}\hat{\mathcal{A}}_\mathrm{S}\hat{U}^\dagger$ and correspondingly a state vector via $|\psi_\mathrm{I}\rangle = \hat{U}\,|\psi_\mathrm{s}\rangle$.

Explicitly the transformed atomic operators read

$$\begin{aligned}
\hat{\sigma}_+ \to \hat{U}\hat{\sigma}_+\hat{U}^\dagger &= \hat{U}_1\hat{\sigma}_+\hat{U}_1^\dagger = e^{i\omega_\mathrm{a}t\hat{\sigma}_+\hat{\sigma}_-}\hat{\sigma}_+e^{-i\omega_\mathrm{a}t\hat{\sigma}_+\hat{\sigma}_-}\\
&= \sum_{n,m=0}^{\infty}\frac{(i\omega_\mathrm{a}t)^n(\hat{\sigma}_+\hat{\sigma}_-)^n}{n!}\underbrace{\hat{\sigma}_+\frac{(i\omega_\mathrm{a}t)^m(\hat{\sigma}_+\hat{\sigma}_-)^m}{m!}}_{=0\forall m\neq 0}\\
&= \sum_{n}^{\infty}\frac{(i\omega_\mathrm{a}t)^n}{n!}\underbrace{(\hat{\sigma}_+\hat{\sigma}_-)^n\hat{\sigma}_+}_{=\hat{\sigma}_+} = e^{i\omega_\mathrm{a}t}\hat{\sigma}_+\\
\hat{\sigma}_- \to \hat{U}\hat{\sigma}_-\hat{U}^\dagger &= \hat{U}_1\hat{\sigma}_-\hat{U}_1^\dagger = \ldots = e^{-i\omega_\mathrm{a}t}\hat{\sigma}_-.
\end{aligned}$$

The transformation of the photonic operators is analogous. We employ the relation $e^{\hat{X}}\hat{Y}e^{-\hat{X}} = \hat{Y} + \frac{1}{1!}\left[\hat{X},\hat{Y}\right] + \frac{1}{2!}\left[\hat{X},\left[\hat{X},\hat{Y}\right]\right] + \ldots$ [184] and the commutator $\left[\hat{a}^\dagger\hat{a},\hat{a}\right] = \hat{a}$ to obtain

$$\begin{aligned}
\hat{a} \to \hat{U}\hat{a}\hat{U}^\dagger &= \hat{U}_2\hat{a}\hat{U}_2^\dagger = e^{i\omega_\mathrm{c}t\hat{a}^\dagger\hat{a}}\hat{a}e^{-i\omega_\mathrm{c}t\hat{a}^\dagger\hat{a}} \\
&= \hat{a} + \left[i\omega_\mathrm{c}t\hat{a}^\dagger\hat{a},\hat{a}\right] + \frac{1}{2!}\left[i\omega_\mathrm{c}t\hat{a}^\dagger\hat{a},\left[i\omega_\mathrm{c}t\hat{a}^\dagger\hat{a},\hat{a}\right]\right] + \ldots \\
&= \hat{a} + (-i\omega_\mathrm{c}t)^1\hat{a} + \frac{1}{2!}(-i\omega_\mathrm{c}t)^2\hat{a} + \ldots \\
&= e^{-i\omega_\mathrm{c}t}\hat{a} \\
\hat{a}^\dagger \to \hat{U}\hat{a}^\dagger\hat{U}^\dagger &= \hat{U}_2\hat{a}^\dagger\hat{U}_2^\dagger = \ldots = e^{i\omega_\mathrm{c}t}\hat{a}^\dagger.
\end{aligned}$$

Next, Schrödinger's equation is written in the interaction picture

$$\begin{aligned}
i\hbar\frac{\partial}{\partial t}|\psi_\mathrm{I}\rangle &= i\hbar\frac{\partial}{\partial t}\left(\hat{U}|\psi_\mathrm{S}\rangle\right) \\
&= -\hat{\mathcal{H}}_0\hat{U}|\psi_\mathrm{S}\rangle + i\hbar\hat{U}\frac{\partial}{\partial t}|\psi_\mathrm{S}\rangle \\
&= -\hat{\mathcal{H}}_0|\psi_\mathrm{I}\rangle + \hat{U}\hat{\mathcal{H}}_\mathrm{S}|\psi_\mathrm{S}\rangle \\
&= -\hat{\mathcal{H}}_0|\psi_\mathrm{I}\rangle + \hat{U}\hat{\mathcal{H}}_\mathrm{S}\hat{U}^\dagger\hat{U}|\psi_\mathrm{S}\rangle \\
&= -\hat{\mathcal{H}}_0|\psi_\mathrm{I}\rangle + \hat{\mathcal{H}}_\mathrm{I}|\psi_\mathrm{I}\rangle \\
&= \hat{\mathcal{H}}^*|\psi_\mathrm{I}\rangle.
\end{aligned}$$

Inserting the transformed atomic and photonic operators into the Hamiltonian $\hat{\mathcal{H}}^*$ yields

$$\begin{aligned}
\hat{\mathcal{H}}^* = \hbar g_0 \Big[\hat{\sigma}_-\hat{a}^\dagger e^{-i(\omega_\mathrm{a}-\omega_\mathrm{c})t} &+ \hat{\sigma}_+\hat{a}e^{i(\omega_\mathrm{a}-\omega_\mathrm{c})t} \\
\hat{\sigma}_+\hat{a}^\dagger e^{i(\omega_\mathrm{a}+\omega_\mathrm{c})t} &+ \hat{\sigma}_-\hat{a}e^{-i(\omega_\mathrm{a}+\omega_\mathrm{c})t}\Big].
\end{aligned}$$

B Numerical Methods

In this appendix we will briefly introduce the split-step Fourier method as a numerical tool to solve nonlinear partial-differential equations [185, 186, 187]. We will then present the method of imaginary-time propagation to approximate the ground state solution of a Gross-Pitaevskii equation. The appendix closes with a discussion on the treatment of s-wave interaction in low dimensional simulations.

Split-Step Fourier-Transform Technique

A time-independent Hamiltonian $\hat{\mathcal{H}}$ usually consists of a kinetic energy term $\hat{T}$ and a potential Term $\hat{V}$. The assumption is that the kinetic energy term $\hat{T}$ is diagonal in Fourier space whereas the potential term $\hat{V}$ is diagonal in real space. Numerically, the kinetic energy is thus cheaply calculate in Fourier-space whereas the potential term is easily applied in real-space. In general however, these terms do not commute $\left[\hat{T},\hat{V}\right] \neq 0$ and the time-propagation operator can thus not be split exactly

$$e^{-i\Delta t\hat{H}/\hbar} = e^{-i\Delta t(\hat{T}+\hat{V})/\hbar} \neq e^{-i\Delta t\hat{T}/\hbar}e^{-i\Delta t\hat{V}/\hbar}.$$

To overcome this issue, we can rewrite the time-evolution operator using the Baker-Hausdorff formula [184]

$$\begin{aligned} e^{-i\Delta t\hat{H}/\hbar} &= e^{-i\frac{\Delta t}{2}\hat{T}/\hbar}e^{-i\Delta t\hat{V}/\hbar}e^{-i\frac{\Delta t}{2}\hat{T}/\hbar}e^{\mathcal{O}(\Delta t^3)} \\ &\underset{\Delta t\to 0}{\longrightarrow} e^{-i\frac{\Delta t}{2}\hat{T}/\hbar}e^{-i\Delta t\hat{V}/\hbar}e^{-i\frac{\Delta t}{2}\hat{T}/\hbar}. \end{aligned} \tag{B.1}$$

The last term $e^{\mathcal{O}(\Delta t^3)}$ tends to unity for $\Delta t \to 0$. We will thus neglect it, keeping in mind to choose a sufficiently small Δt when running the simulation.

Equation (B.1) provides us with an algorithm sketched in figure B.1 that is readily implemented. Application of the full time propagator is approximated by applying half a time step in Fourier-space (involving $\hat{T}$), a full time step in real-space (involving $\hat{V}$) and again half a time step in Fourier-space (involving $\hat{T}$). Repeating this scheme multiple times yields the time evolution of the wave function.

The advantage of this algorithm is that each application of the time propagator corresponds to simple multiplications since the operators are diagonal in their corresponding space. Computational costly is however the transformation back and forth between real space and Fourier space. The broad availability of highly optimized fast-Fourier transform techniques [188] helps to achieve short run-times of the simulation while keeping the development time reasonable.

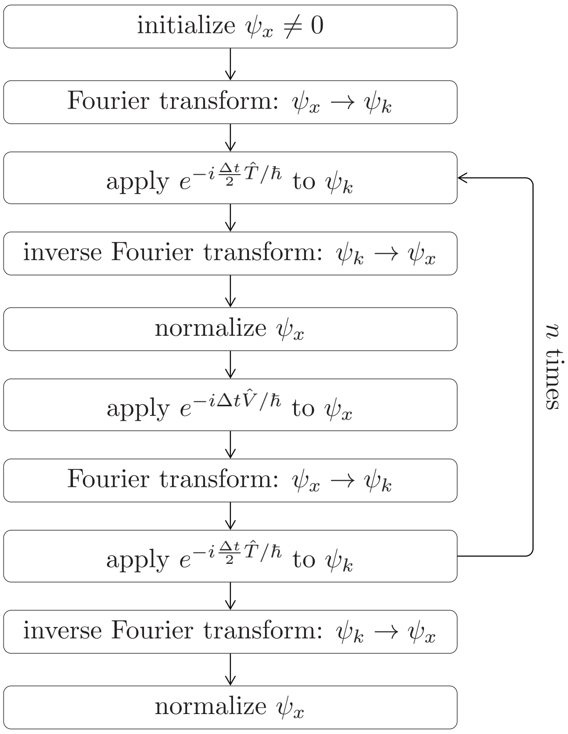
initialize $\psi_x \neq 0$
Fourier transform: $\psi_x \to \psi_k$
apply $e^{-i\frac{\Delta t}{2}\hat{T}/\hbar}$ to ψ_k
inverse Fourier transform: $\psi_k \to \psi_x$
normalize ψ_x
apply $e^{-i\Delta t\hat{V}/\hbar}$ to ψ_x
Fourier transform: $\psi_x \to \psi_k$
apply $e^{-i\frac{\Delta t}{2}\hat{T}/\hbar}$ to ψ_k
inverse Fourier transform: $\psi_k \to \psi_x$
normalize ψ_x
n times

Figure B.1.: Sketch of the split-step Fourier algorithm.

Imaginary-Time Propagation

Imaginary-time propagation is used to find an approximation of the ground state of a Hamiltonian. Lets consider a general wave function $|\psi\rangle = \sum_{k=0}^{\infty} c_k |k\rangle$, where the basis state $|k\rangle$ are eigenstates of the Hamiltonian $\hat{\mathcal{H}}$, i.e., $\hat{\mathcal{H}}|k\rangle = \epsilon_k |k\rangle$. For simplicity, we choose $\epsilon_0 = 0$. We will now apply the time propagator $e^{i\hat{\mathcal{H}}\Delta_t/\hbar}$ but will choose the time-step $\Delta_t = -i\tau$ to be an imaginary time. Applying this operator to $|\psi\rangle$ gives

$$|\psi(\tau)\rangle = e^{-\hat{\mathcal{H}}\tau} \sum_{k=0}^{\infty} c_k |k\rangle = \sum_{k=0}^{\infty} e^{-\epsilon_k \tau} c_k |k\rangle.$$

All basis states are exponentially damped in time τ. The damping rate is given by the eigenenergy ϵ_k, yielding to a bigger damping for states with higher energy. The biggest contribution in the sum will thus be given by the lowest energy eigenstate for sufficiently large τ. It should be noted, that propagation in imaginary time is not unitary and thus does not preserve the normalization of the wave function. It has to be re-normalized after each application of the propagator.

The combination of the imaginary-time propagation with the split-step Fourier method yields an efficient algorithm to numerically find the ground state of a non-liner Schrödinger equation. Great care has to be taken in the choice of the time-step τ. The split-step method demands a small value of τ to justify the approximation in equation B.1. On the other hand, imaginary-time propagation demands a large value of τ to “damp out” all states apart from the ground state. This can to be achieved by successive application of many small time-steps.

S-Wave Scattering

A complication arises from the non-linear s-wave interaction term present in the Gross-Pitaevskii equation (GPE) [75, 69]. It is written as

$$\frac{4\pi\hbar^2 a}{m}\left|\psi(x)\right|^2,$$

where a is the s-wave scattering length, m is the atomic mass and $\psi(x)$ is the atomic wave function. Typical system sizes regarded in the scope of this thesis suffer from the high memory usage and slow simulation speed. It is thus often desirable to perform the simulations in lower dimensions. While this can be readily done from an algorithmic point of view, the interaction strength has to be rescaled to give physical results.

Different methods are used for rescaling. For simulating a BEC in a trap, we follow reference [189]. The idea it to rescale the interaction strength to give the same chemical potential in lower dimensions (1D and 2D) as we would get in the full 3D calculation. The chemical potentials are readily calculated analytically in the Thomas-Fermi limit and set equal. This leads to following expressions for the interaction strength in one and two dimensions

$$\begin{aligned} a_{1\mathrm{d}} &= \left(\frac{15Na}{\bar{a}}\right)^{2/5}\left(\frac{\hbar\bar{\omega}}{2}\right)^{3/2}\frac{\sqrt{2m}}{3\omega_x\hbar 2\pi N} \\ a_{2\mathrm{d}} &= \frac{5^{4/5}\left(\frac{aN}{\bar{a}}\right)^{2/5}\bar{\omega}^2}{2\cdot 3^{1/5}N\pi\omega_x\omega_y}, \end{aligned}$$

where N is the particle number, $(\omega_x, \omega_y, \omega_z)$ are the trap frequencies along the three orthogonal axis, $\bar{\omega} = (\omega_x\omega_y\omega_z)^{1/3}$ is the mean trapping frequency and $\bar{a} = \sqrt{\frac{\hbar}{m\bar{\omega}}}$.

C Physical constants

All physical constants used in this thesis have been published in [190] which can be accessed via `http://physics.nist.gov/constants`.
All data concerning the physical properties of ^{87}Rb have been taken from [105] and can be accessed via `http://steck.us/alkalidata/`.

Bibliography

[1] R. H. Dicke. *Coherence in Spontaneous Radiation Processes.* Phys. Rev. **93**(1), 99 (1954)

[2] K. Baumann, C. Guerlin, F. Brennecke and T. Esslinger. *Dicke quantum phase transition with a superfluid gas in an optical cavity.* Nature **464**(7293), 1301 (2010)

[3] K. Baumann, R. Mottl, F. Brennecke and T. Esslinger. *Exploring Symmetry Breaking at the Dicke Quantum Phase Transition.* Phys. Rev. Lett. **107**(14), 140402 (2011)

[4] *Breakthrough of the Year: The Runners-Up.* Science **330**(6011), 1605 (2010)

[5] M. Gross and S. Haroche. *Superradiance: An essay on the theory of collective spontaneous emission.* Phys. Rep. **93**(5), 301 (1982)

[6] J. P. Gordon, H. J. Zeiger and C. H. Townes. *Molecular Microwave Oscillator and New Hyperfine Structure in the Microwave Spectrum of NH3.* Phys. Rev. **95**(1), 282 (1954)

[7] J. P. Gordon, H. J. Zeiger and C. H. Townes. *The Maser - New Type of Microwave Amplifier, Frequency Standard, and Spectrometer.* Phys. Rev. **99**(4), 1264 (1955)

[8] T. H. Maiman. *Stimulated Optical Radiation in Ruby.* Nature **187**(4736), 493 (1960)

[9] N. Skribanowitz, I. P. Herman, J. C. MacGillivray and M. S. Feld. *Observation of Dicke Superradiance in Optically Pumped HF Gas.* Phys. Rev. Lett. **30**(8), 309 (1973)

[10] M. Gross, C. Fabre, P. Pillet and S. Haroche. *Observation of Near-Infrared Dicke Superradiance on Cascading Transitions in Atomic Sodium.* Phys. Rev. Lett. **36**(17), 1035 (1976)

[11] A. Flusberg, T. Mossberg and S. R. Hartmann. *Observation of Dicke superradiance at 1.30 um in atomic Tl vapor.* Phys. Lett. A **58**(6), 373 (1976)

[12] Q. H. F. Vrehen, H. M. J. Hikspoors and H. M. Gibbs. *Quantum Beats in Superfluorescence in Atomic Cesium.* Phys. Rev. Lett. **38**(14), 764 (1977)

[13] H. M. Gibbs, Q. H. F. Vrehen and H. M. J. Hikspoors. *Single-Pulse Superfluorescence in Cesium.* Phys. Rev. Lett. **39**(9), 547 (1977)

[14] P. Cahuzac, H. Sontag and P. E. Toschek. *Visible superfluorescence from atomic europium.* Opt. Commun. **31**(1), 37 (1979)

[15] S. Inouye, A. P. Chikkatur, D. M. Stamper-Kurn, J. Stenger, D. E. Pritchard and W. Ketterle. *Superradiant Rayleigh Scattering from a Bose-Einstein Condensate.* Science **285**(5427), 571 (1999)

[16] Y. Yoshikawa, Y. Torii and T. Kuga. *Superradiant Light Scattering from Thermal Atomic Vapors.* Phys. Rev. Lett. **94**(8), 83602 (2005)

[17] R. Bonifacio and L. D. Salvo. *Collective atomic recoil laser (CARL) optical gain without inversion by collective atomic recoil and self-bunching of two-level atoms.* Nucl. Instr. Meth. Phys. A **341**(1), 360 (1994)

[18] S. Slama, S. Bux, G. Krenz, C. Zimmermann and P. W. Courteille. *Superradiant Rayleigh Scattering and Collective Atomic Recoil Lasing in a Ring Cavity.* Phys. Rev. Lett. **98**(5), 053603 (2007)

[19] K. Hepp and E. H. Lieb. *On the superradiant phase transition for molecules in a quantized radiation field: the dicke maser model.* Ann. Phys. **76**(2), 360 (1973)

[20] Y. K. Wang and F. T. Hioe. *Phase Transition in the Dicke Model of Superradiance.* Phys. Rev. A **7**(3), 831 (1973)

[21] S. Sachdev. *Quantum Phase Transitions* (Cambridge University Press, Cambridge, 1999)

[22] H. J. Carmichael, C. W. Gardiner and D. F. Walls. *Higher order corrections to the Dicke superradiant phase transition.* Phys. Rev. Lett. **46**(1), 47 (1973)

[23] Y. Kaluzny, P. Goy, M. Gross, J. M. Raimond and S. Haroche. *Observation of Self-Induced Rabi Oscillations in Two-Level Atoms Excited Inside a Resonant Cavity: The Ringing Regime of Superradiance.* Phys. Rev. Lett. **51**(13), 1175 (1983)

[24] P. Goy, J. M. Raimond, M. Gross and S. Haroche. *Observation of Cavity-Enhanced Single-Atom Spontaneous Emission.* Phys. Rev. Lett. **50**(24), 1903 (1983)

[25] D. Meschede, H. Walther and G. Müller. *One-atom maser.* Phys. Rev. Lett. **54**(6), 551 (1985)

[26] G. Rempe, H. Walther and N. Klein. *Observation of quantum collapse and revival in a one-atom maser.* Phys. Rev. Lett. **58**(4), 353 (1987)

[27] G. Rempe, R. J. Thompson, R. J. Brecha, W. D. Lee and H. J. Kimble. *Optical bistability and photon statistics in cavity quantum electrodynamics.* Phys. Rev. Lett. **67**(13), 1727 (1991)

[28] R. J. Thompson, G. Rempe and H. J. Kimble. *Observation of normal-mode splitting for an atom in an optical cavity.* Phys. Rev. Lett. **68**(8), 1132 (1992)

[29] G. Khitrova, H. M. Gibbs, M. Kira, S. W. Koch and A. Scherer. *Vacuum Rabi splitting in semiconductors.* Nat. Phys. **2**(2), 81 (2006)

[30] A. Wallraff, D. I. Schuster, A. Blais, L. Frunzio, R. S. Huang, J. Majer, S. Kumar, S. M. Girvin and R. J. Schoelkopf. *Strong coupling of a single photon to a superconducting qubit using circuit quantum electrodynamics.* Nature **431**(7005), 162 (2004)

[31] T. Niemczyk, F. Deppe, H. Huebl, E. P. Menzel, F. Hocke, M. J. Schwarz, J. J. Garcia-Ripoll, D. Zueco, T. Hummer, E. Solano, A. Marx and R. Gross. *Circuit quantum electrodynamics in the ultrastrong-coupling regime.* Nat. Phys. **6**(10), 772 (2010)

[32] P. Forn-Díaz, J. Lisenfeld, D. Marcos, J. J. García-Ripoll, E. Solano, C. J. P. M. Harmans and J. E. Mooij. *Observation of the Bloch-Siegert Shift in a Qubit-Oscillator System in the Ultrastrong Coupling Regime.* Phys. Rev. Lett. **105**(23), 237001 (2010)

[33] F. Dimer, B. Estienne, A. Parkins and H. Carmichael. *Proposed realization of the Dicke-model quantum phase transition in an optical cavity QED system.* Phys. Rev. A **75**(1), 013804 (2007)

[34] D. Nagy, G. Szirmai and P. Domokos. *Self-organization of a Bose-Einstein condensate in an optical cavity.* Eur. Phys. J. D **48**(1), 127 (2008)

[35] P. Domokos and H. Ritsch. *Collective Cooling and Self-Organization of Atoms in a Cavity.* Phys. Rev. Lett. **89**(25), 253003 (2002)

[36] A. Black, H. Chan and V. Vuletić. *Observation of Collective Friction Forces due to Spatial Self-Organization of Atoms: From Rayleigh to Bragg Scattering.* Phys. Rev. Lett. **91**(20), 203001 (2003)

[37] B. Nagorny, T. Elsässer, H. Richter, A. Hemmerich, D. Kruse, C. Zimmermann and P. Courteille. *Optical lattice in a high-finesse ring resonator.* Phys. Rev. A **67**(3), 031401 (2003)

[38] D. Kruse, M. Ruder, J. Benhelm, C. Von Cube, C. Zimmermann, P. W. Courteille, T. Elsässer, B. Nagorny and A. Hemmerich. *Cold atoms in a high-Q ring-cavity.* Phys. Rev. Lett. **67**(5), 051802 (2003)

[39] B. Nagorny, T. Elsässer and A. Hemmerich. *Collective atomic motion in an optical lattice formed inside a high finesse cavity.* Phys. Rev. Lett. **91**(15), 153003 (2003)

[40] A. Öttl, S. Ritter, M. Köhl and T. Esslinger. *Correlations and Counting Statistics of an Atom Laser.* Phys. Rev. Lett. **95**(9), 90404 (2005)

[41] S. Gupta, K. L. Moore, K. W. Murch and D. M. Stamper-Kurn. *Cavity Nonlinear Optics at Low Photon Numbers from Collective Atomic Motion.* Phys. Rev. Lett. **99**(21), 213601 (2007)

[42] Y. Colombe, T. Steinmetz, G. Dubois, F. Linke, D. Hunger and J. Reichel. *Strong atom-field coupling for Bose-Einstein condensates in an optical cavity on a chip.* Nature **450**(7167), 272 (2007)

[43] K. J. Arnold, M. P. Baden and M. D. Barrett. *Collective Cavity QED with Multiple Atomic Levels.* arXiv:1105.1236 (2011)

[44] D. Nagy, G. Kónya, G. Szirmai and P. Domokos. *Dicke-Model Phase Transition in the Quantum Motion of a Bose-Einstein Condensate in an Optical Cavity.* Phys. Rev. Lett. **104**(13), 130401 (2010)

[45] A. F. Andreev and I. M. Lifshitz. *Quantum theory of crystal defects.* Soviet Physics (JETP) **56**, 2057 (1969)

[46] G. V. Chester. *Speculations on Bose-Einstein Condensation and Quantum Crystals.* Phys. Rev. A **2**(1), 256 (1970)

[47] A. J. Leggett. *Can a Solid Be "Superfluid"?* Phys. Rev. Lett. **25**(22), 1543 (1970)

[48] H. Büchler and G. Blatter. *Supersolid versus Phase Separation in Atomic Bose-Fermi Mixtures.* Phys. Rev. Lett. **91**(13), 130404 (2003)

[49] I. B. Mekhov, C. Maschler and H. Ritsch. *Probing quantum phases of ultracold atoms in optical lattices by transmission spectra in cavity quantum electrodynamics.* Nat. Phys. **3**, 319 (2007)

[50] S. Schneider and G. J. Milburn. *Entanglement in the steady state of a collective-angular-momentum (Dicke) model.* Phys. Rev. A **65**(4), 42107 (2002)

[51] A. Messikh, Z. Ficek and M. R. B. Wahiddin. *Entanglement and spin squeezing in the two-atom Dicke model.* J. Opt. B **5**(2), 1 (2003)

[52] N. Lambert, C. Emary and T. Brandes. *Entanglement and the Phase Transition in Single-Mode Superradiance.* Phys. Rev. Lett. **92**(7), 73602 (2004)

[53] V. Buzcaronek, M. Orszag and M. Roscaronko. *Instability and Entanglement of the Ground State of the Dicke Model.* Phys. Rev. Lett. **94**(16), 163601 (2005)

[54] J. Reslen, L. Quiroga and N. F. Johnson. *Direct equivalence between quantum phase transition phenomena in radiation-matter and magnetic systems: Scaling of entanglement.* Europhys. Lett. **69**(1), 8 (2005)

[55] C. Emary and T. Brandes. *Quantum Chaos Triggered by Precursors of a Quantum Phase Transition: The Dicke Model.* Phys. Rev. Lett. **90**(4), 044101 (2003)

[56] C. Emary and T. Brandes. *Chaos and the quantum phase transition in the Dicke model.* Phys. Rev. E **67**(6), 66203 (2003)

[57] X. W. Hou and B. Hu. *Decoherence, entanglement, and chaos in the Dicke model.* Phys. Rev. A **69**(4), 42110 (2004)

[58] G. Chen, J. Li and J. Q. Liang. *Critical property of the geometric phase in the Dicke model.* Phys. Rev. A **74**(5), 54101 (2006)

[59] F. Plastina, G. Liberti and A. Carollo. *Scaling of Berry's phase close to the Dicke quantum phase transition.* Europhys. Lett. **76**(2), 182 (2006)

[60] J. Vidal and S. Dusuel. *Finite-size scaling exponents in the Dicke model.* Europhys. Lett. **74**(5), 817 (2006)

[61] Q. H. Chen, Y. Y. Zhang, T. Liu and K. L. Wang. *Numerically exact solution to the finite-size Dicke model.* Phys. Rev. A **78**(5), 51801 (2008)

[62] T. Liu, Y. Y. Zhang, Q. H. Chen and K. L. Wang. *Large- N scaling behavior of the ground-state energy, fidelity, and the order parameter in the Dicke model.* Phys. Rev. A **80**(2), 23810 (2009)

[63] E. T. Jaynes and F. W. Cummings. *Comparison of quantum and semiclassical radiation theories with application to the beam maser.* Proc. IEEE **51**(1), 89 (1963)

[64] P. Meystre and M. Sargant III. *Elements of Quantum Optics* (Springer-Verlag, Berlin Heidelberg New York, 1999), 3rd edition

[65] M. O. Scully and M. S. Zubairy. *Quantum Optics* (Cambridge University Press, Cambridge, 1997)

[66] C. Maschler, I. B. Mekhov and H. Ritsch. *Ultracold atoms in optical lattices generated by quantized light fields.* Eur. Phys. J. D **46**(3), 545 (2008)

[67] F. Brennecke. *Collective Interaction Between a Bose-Einstein Condensate and a Coherent Few-Photon Field.* Ph.D. thesis, ETH Zürich (2009)

[68] E. Brion, L. H. Pedersen and K. Mø lmer. *Adiabatic elimination in a lambda system.* J. Phys. A **40**(5), 1033 (2007)

[69] C. J. Pethick and H. Smith. *Bose-Einstein Condensation in Dilute Gasses* (Cambridge University Press, Cambridge, 2008), 2nd edition

[70] E. M. Purcell. *Proceedings of the American Physical Society.* Phys. Rev. **69**(11-12), 674 (1946)

[71] J. Dalibard and C. Cohen-Tannoudji. *Dressed-atom approach to atomic motion in laser light: the dipole force revisited.* J. Opt. Soc. Am. B **2**(11), 1707 (1985)

[72] R. Grimm, M. Weidemüller and Y. Ovchinnikov. *Optical dipole traps for neutral atoms.* Adv. At., Mol., Opt. Phys. **42**, 95 (2000)

[73] P. Münstermann, T. Fischer, P. Maunz, P. W. H. Pinkse and G. Rempe. *Observation of Cavity-Mediated Long-Range Light Forces between Strongly Coupled Atoms.* Phys. Rev. Lett. **84**(18), 4068 (2000)

[74] D. Nagy. *Collective effects of radiatively interacting ultracold atoms in an optical resonator.* Ph.D. thesis, Budapest University of Technology and Economics (2010)

[75] L. Pitaevskii and S. Stringari. *Bose-Einstein Condensation* (Oxford University Press, Oxford, 2003)

[76] D. Nagy, J. K. Asbóth, P. Domokos and H. Ritsch. *Self-organization of a laser-driven cold gas in a ring cavity.* Europhys. Lett. **74**(2), 254 (2006)

[77] H. Haken. *Cooperative phenomena in systems far from thermal equilibrium and in nonphysical systems.* Rev. Mod. Phys. **47**(1), 67 (1975)

[78] W. R. Frensley. *Boundary conditions for open quantum systems driven far from equilibrium.* Rev. Mod. Phys. **62**(3), 745 (1990)

[79] M. Esposito, U. Harbola and S. Mukamel. *Nonequilibrium fluctuations, fluctuation theorems, and counting statistics in quantum systems.* Rev. Mod. Phys. **81**(4), 1665 (2009)

[80] J. Keeling, M. J. Bhaseen and B. D. Simons. *Collective Dynamics of Bose-Einstein Condensates in Optical Cavities.* Phys. Rev. Lett. **105**(4), 43001 (2010)

[81] B. Öztop, M. Bordyuh, O. E. Müstecaplıoğlu and H. E. Türeci. *Excitations of optically driven atomic condensate in a cavity: theory of photodetection measurements.* arXiv:1107.3108 (2011)

[82] D. Nagy, G. Szirmai and P. Domokos. *On the critical exponent of a quantum noise driven phase transition: the open system Dicke-model.* arXiv:1107.4323 (2011)

[83] H. J. Carmichael. *Statistical Methods in Quantum Optics 1* (Springer-Verlag, Berlin Heidelberg New York, 2002), 2nd edition

[84] T. Andrews. *Bakerian Lecture: On the Continuity of the Gaseous and Liquid States of Matter.* Proc. R. Soc. London **18**, 42 (1869)

[85] K. Huang. *Statistical Mechanics* (John Wiley & Sons, 1987)

[86] L. D. Landau and E. M. Lifshitz. *Statistical Physics, Part 1* (Reed Educational and Professional Publishing Ltd, Oxford, 1980), 3rd edition

[87] M. O. Mewes, M. R. Andrews, D. M. Kurn, D. S. Durfee, C. G. Townsend and W. Ketterle. *Output coupler for Bose-Einstein condensed atoms.* Phys. Rev. Lett. **78**(4), 582 (1997)

[88] B. Anderson and M. Kasevich. *Macroscopic quantum interference from atomic tunnel arrays.* Science **282**(5394), 1686 (1998)

[89] E. W. Hagley, L. Deng, M. Kozuma, J. Wen, K. Helmerson, S. L. Rolston and W. D. Phillips. *A well-collimated quasi-continuous atom laser.* Science **283**(5408), 1706 (1999)

[90] I. Bloch, T. Hänsch and T. Esslinger. *Atom Laser with a cw Output Coupler.* Phys. Rev. Lett. **82**(15), 3008 (1999)

[91] T. Bourdel, T. Donner, S. Ritter, A. Öttl, M. Köhl and T. Esslinger. *Cavity QED detection of interfering matter waves.* Phys. Rev. A **73**(4), 043602 (2006)

[92] T. Donner, S. Ritter, T. Bourdel, A. Öttl, M. Köhl and T. Esslinger. *Critical behavior of a trapped interacting Bose gas.* Science **315**(5818), 1556 (2007)

[93] S. Ritter, A. Öttl, T. Donner, T. Bourdel, M. Köhl and T. Esslinger. *Observing the Formation of Long-Range Order during Bose-Einstein Condensation.* Phys. Rev. Lett. **98**(9), 90402 (2007)

[94] F. Brennecke, T. Donner, S. Ritter, T. Bourdel, M. Köhl and T. Esslinger. *Cavity QED with a Bose-Einstein condensate.* Nature **450**(7167), 268 (2007)

[95] F. Brennecke, S. Ritter, T. Donner and T. Esslinger. *Cavity Optomechanics with a Bose-Einstein Condensate.* Science **322**(5899), 235 (2008)

[96] S. Ritter, F. Brennecke, K. Baumann, T. Donner, C. Guerlin and T. Esslinger. *Dynamical coupling between a Bose-Einstein condensate and a cavity optical lattice.* Appl. Phys. B **95**(2), 213 (2009)

[97] A. Öttl, S. Ritter, M. Köhl and T. Esslinger. *Hybrid apparatus for Bose-Einstein condensation and cavity quantum electrodynamics: Single atom detection in quantum degenerate gases.* Rev. Sci. Instrum. **77**(6), 63118 (2006)

[98] A. Öttl. *Correlations and Counting Statistics of an Atom Laser.* Ph.D. thesis, ETH Zürich (2006)

[99] S. Ritter. *Probing Coherence During Bose-Einstein Condensation.* Ph.D. thesis, ETH Zürich (2007)

[100] T. Donner. *Critical Behavior of a Trapped Interacting Bose Gas.* Ph.D. thesis, ETH Zürich (2008)

[101] L. Ricci, M. Weidemüller, T. Esslinger, A. Hemmerich, C. Zimmermann, V. Vuletić, W. König and T. W. Hänsch. *A compact grating-stabilized diode laser system for atomic physics.* Opt. Commun. **117**(5-6), 541 (1995)

[102] T. Stöferle. *Exploring Atomic Quantum Gases in Optical Lattices.* Ph.D. thesis, ETH Zürich (2005)

[103] E. L. Raab, M. Prentiss, A. Cable, S. Chu and D. E. Pritchard. *Trapping of neutral sodium atoms with radiation pressure.* Phys. Rev. Lett. **59**(23), 2631 (1987)

[104] J. Fortagh, A. Grossmann, T. W. Hänsch and C. Zimmermann. *Fast loading of a magneto-optical trap from a pulsed thermal source.* J. Appl. Phys. **84**(12), 6499 (1998)

[105] D. Steck. *Rubidium 87 D Line Data* (2010). `http://steck.us/alkalidata/`

[106] H. J. Metcalf and P. Van der Straten. *Laser Cooling and Trapping* (Springer-Verlag, New York, 1999)

[107] M. Greiner, I. Bloch, T. W. Hänsch and T. Esslinger. *Magnetic transport of trapped cold atoms over a large distance.* Phys. Rev. A **63**(3), 31401 (2001)

[108] T. Esslinger, I. Bloch and T. Hänsch. *Bose-Einstein condensation in a quadrupole-Ioffe-configuration trap.* Phys. Rev. A **58**(4), 2664 (1998)

[109] S. Kuhr, W. Alt, D. Schrader, M. Müller, V. Gomer and D. Meschede. *Deterministic delivery of a single atom.* Science **293**(5528), 278 (2001)

[110] J. A. Sauer, K. M. Fortier, M. S. Chang, C. D. Hamley and M. S. Chapman. *Cavity QED with optically transported atoms.* Phys. Rev. A **69**(5), 051804 (2004)

[111] D. Steck. *Cesium D Line Data* (2010). `http://steck.us/alkalidata/`

[112] G. C. Bjorklund, M. D. Levenson, W. Lenth and C. Ortiz. *Frequency modulation (FM) spectroscopy.* Appl. Phys. B **32**(3), 145 (1983)

[113] B. E. A. Saleh and M. C. Teich. *Fundamentals of photonics* (John Wiley & Sons, Inc., 1991)

[114] H. A. Bachor and C. R. Ralph. *A Guide to Experiments in Quantum Optics* (WILEY-VCH Verlag, Weinheim, 2004), 2nd edition

[115] K. W. Murch. *Cavity Quantum Optomechanics with Ultracold Atoms.* Ph.D. thesis, University of California, Berkeley (2008)

[116] H. Mabuchi, J. Ye and H. J. Kimble. *Full observation of single-atom dynamics in cavity QED.* Appl. Phys. B **68**(6), 1095 (1999)

[117] M. J. Collett, R. Loudon and C. W. Gardiner. *Quantum theory of optical homodyne and heterodyne detection.* J. Mod. Opt. **6**(7), 881 (1987)

[118] M. H. Anderson, J. R. Ensher, M. R. Matthews, C. . E. Wieman and E. A. Cornell. *Observation of Bose-Einstein condensation in a dilute atomic vapor.* Science **269**(5221), 198 (1995)

[119] K. B. Davis, M. O. Mewes, M. R. Andrews, N. J. van Druten, D. S. Durfee, D. M. Kurn and W. Ketterle. *Bose-Einstein Condensation in a Gas of Sodium Atoms.* Phys. Rev. Lett. **75**(22), 3969 (1995)

[120] C. A. Regal, M. Greiner and D. S. Jin. *Observation of Resonance Condensation of Fermionic Atom Pairs.* Phys. Rev. Lett. **92**(4), 040403 (2004)

[121] M. Zwierlein, C. Stan, C. Schunck, S. Raupach, A. Kerman and W. Ketterle. *Condensation of Pairs of Fermionic Atoms near a Feshbach Resonance.* Phys. Rev. Lett. **92**(12), 120403 (2004)

[122] M. Bartenstein, A. Altmeyer, S. Riedl, S. Jochim, C. Chin, J. Denschlag and R. Grimm. *Collective Excitations of a Degenerate Gas at the BEC-BCS Crossover.* Phys. Rev. Lett. **92**(20), 203201 (2004)

[123] M. Greiner, O. Mandel, T. Esslinger, T. W. Hänsch and I. Bloch. *Quantum phase transition from a superfluid to a Mott insulator in a gas of ultracold atoms.* Nature **415**(6867), 39 (2002)

[124] R. Feynman. *Simulating physics with computers.* Internat. J. Theoret. Phys. **21**(6), 467 (1982)

[125] S. Lloyd. *Universal Quantum Simulators.* Science **273**(5278), 1073 (1996)

[126] T. Lahaye, C. Menotti, L. Santos, M. Lewenstein and T. Pfau. *The physics of dipolar bosonic quantum gases.* Rep. Prog. Phys. **72**(12), 126401 (2009)

[127] J. K. Asbóth, P. Domokos and H. Ritsch. *Correlated motion of two atoms trapped in a single-mode cavity field.* Phys. Rev. A **70**(1), 13414 (2004)

[128] J. K. Asbóth, H. Ritsch and P. Domokos. *Collective Excitations and Instability of an Optical Lattice due to Unbalanced Pumping.* Phys. Rev. Lett. **98**(20), 203008 (2007)

[129] L. Amico, R. Fazio, A. Osterloh and V. Vedral. *Entanglement in many-body systems.* Rev. Mod. Phys. **80**(2), 517 (2008)

[130] A. Osterloh, L. Amico, G. Falci and R. Fazio. *Scaling of entanglement close to a quantum phase transition.* Nature **416**(6881), 608 (2002)

[131] R. Botet, R. Jullien and P. Pfeuty. *Size Scaling for Infinitely Coordinated Systems.* Phys. Rev. Lett. **49**(7), 478 (1982)

[132] P. Domokos and H. Ritsch. *Mechanical effects of light in optical resonators.* J. Opt. Soc. Am. B **20**(5), 1098 (2003)

[133] S. Gopalakrishnan, B. Lev and P. Goldbart. *Emergent crystallinity and frustration with Bose-Einstein condensates in multimode cavities.* Nat. Phys. **5**(11), 845 (2009)

[134] K. W. Murch, K. L. Moore, S. Gupta and D. M. Stamper-kurn. *Observation of quantum-measurement backaction with an ultracold atomic gas.* Nat. Phys. **4**(7), 561 (2008)

[135] C. Orzel, A. K. Tuchman, M. L. Fenselau, M. Yasuda and M. A. Kasevich. *Squeezed States in a Bose-Einstein Condensate.* Science **291**(5512), 2386 (2001)

[136] J. Klinner, M. Lindholdt, B. Nagorny and A. Hemmerich. *Normal Mode Splitting and Mechanical Effects of an Optical Lattice in a Ring Cavity.* Phys. Rev. Lett. **96**(2), 023002 (2006)

[137] M. Greiner, I. Bloch, O. Mandel, T. W. Hänsch and T. Esslinger. *Exploring Phase Coherence in a 2D Lattice of Bose-Einstein Condensates.* Phys. Rev. Lett. **87**(16), 160405 (2001)

[138] J. K. Asbóth, P. Domokos, H. Ritsch and A. Vukics. *Self-organization of atoms in a cavity field: Threshold, bistability, and scaling laws.* Phys. Rev. A **72**(5), 53417 (2005)

[139] C. Maschler, H. Ritsch, A. Vukics and P. Domokos. *Entanglement assisted fast reordering of atoms in an optical lattice within a cavity at T=0.* Opt. Commun. **273**(2), 446 (2007)

[140] I. B. Mekhov and H. Ritsch. *Quantum Nondemolition Measurements and State Preparation in Quantum Gases by Light Detection.* Phys. Rev. Lett. **102**(2), 020403 (2009)

[141] L. E. Sadler, J. M. Higbie, S. R. Leslie and M. Vengalattore. *Spontaneous symmetry breaking in a quenched ferromagnetic spinor Bose-Einstein condensate.* Nature **443**(7109), 312 (2006)

[142] J. Kronjäger, C. Becker, P. Soltan-Panahi, K. Bongs and K. Sengstock. *Spontaneous Pattern Formation in an Antiferromagnetic Quantum Gas.* Phys. Rev. Lett. **105**(9), 090402 (2010)

[143] M. Scherer, B. Lücke, G. Gebreyesus, O. Topic, F. Deuretzbacher, W. Ertmer, L. Santos, J. J. Arlt and C. Klempt. *Spontaneous Breaking of Spatial and Spin Symmetry in Spinor Condensates.* Phys. Rev. Lett. **105**(13), 135302 (2010)

[144] W. S. Bakr, A. Peng, M. E. Tai, R. Ma, J. Simon, J. I. Gillen, S. Fölling, L. Pollet and M. Greiner. *Probing the Superfluid-to-Mott Insulator Transition at the Single-Atom Level.* Science **329**(5991), 547 (2010)

[145] D. Chen, M. White, C. Borries and B. DeMarco. *Quantum Quench of an Atomic Mott Insulator.* Phys. Rev. Lett. **106**(23), 235304 (2011)

[146] W. H. Zurek, U. Dorner and P. Zoller. *Dynamics of a Quantum Phase Transition.* Phys. Rev. Lett. **95**(10), 105701 (2005)

[147] J. Dziarmaga. *Dynamics of a quantum phase transition and relaxation to a steady state.* Adv. Phys. **59**(6), 1063 (2010)

[148] S. Haroche and J. M. Raimond. *Exploring the Quantum* (Oxford University Press, Oxford, 2006)

[149] J. M. Raimond, M. Brune and S. Haroche. *Manipulating quantum entanglement with atoms and photons in a cavity.* Rev. Mod. Phys. **73**(3), 565 (2001)

[150] H. Walther. *Quantum Phenomena of Single Atoms.* Adv. Chem. Phys. **122**, 167 (2002)

[151] H. J. Kimble. *Strong interactions of single atoms and photons in cavity QED.* Phys. Scr. **1998**(76), 127 (1998)

[152] P. Maunz, T. Puppe, I. Schuster, N. Syassen, P. W. H. Pinkse and G. Rempe. *Normal-mode spectroscopy of a single-bound-atom-cavity system.* Phys. Rev. Lett. **94**(3), 033002 (2005)

[153] A. B. Mundt, A. Kreuter, C. Becher, D. Leibfried, J. Eschner, F. Schmidt-Kaler and R. Blatt. *Coupling a single atomic quantum bit to a high finesse optical cavity.* Phys. Rev. Lett. **89**(10), 103001 (2002)

[154] C. J. Hood, T. W. Lynn, A. C. Doherty, A. S. Parkins and H. J. Kimble. *The Atom-Cavity Microscope: Single Atoms Bound in Orbit by Single Photons.* Science **287**(5457), 1447 (2000)

[155] P. W. H. Pinkse, T. Fischer, P. Maunz and G. Rempe. *Trapping an atom with single photons.* Nature **404**(6776), 365 (2000)

[156] D. Kruse, C. Von Cube, C. Zimmermann and P. W. Courteille. *Observation of lasing mediated by collective atomic recoil.* Phys. Rev. Lett. **91**(18), 183601 (2003)

[157] C. Höhberger Metzger and K. Karrai. *Cavity cooling of a microlever.* Nature **432**(7020), 1002 (2004)

[158] A. Schliesser, P. Del'Haye, N. Nooshi, K. J. Vahala and T. J. Kippenberg. *Radiation pressure cooling of a micromechanical oscillator using dynamical backaction.* Phys. Rev. Lett. **97**(24), 243905 (2006)

[159] O. Arcizet, P. F. Cohadon, T. Briant, M. Pinard and A. Heidmann. *Radiation-pressure cooling and optomechanical instability of a micromirror.* Nature **444**(7115), 71 (2006)

[160] S. Gigan, H. R. Böhm, M. Paternostro, F. Blaser, G. Langer, J. B. Hertzberg, K. C. Schwab, D. Bäuerle, M. Aspelmeyer and A. Zeilinger. *Self-cooling of a micromirror by radiation pressure.* Nature **444**(7115), 67 (2006)

[161] T. Corbitt, Y. Chen, E. Innerhofer, H. Müller-Ebhardt, D. Ottaway, H. Rehbein, D. Sigg, S. Whitcomb, C. Wipf and N. Mavalvala. *An All-Optical Trap for a Gram-Scale Mirror.* Phys. Rev. Lett. **98**(15), 150802 (2007)

[162] J. D. Thompson, B. M. Zwickl, A. M. Jayich, F. Marquardt, S. M. Girvin and J. G. E. Harris. *Strong dispersive coupling of a high finesse cavity to a micromechanical membrane.* Nature **452**(7183), 72 (2008)

[163] D. Kleckner and D. Bouwmeester. *Sub-kelvin optical cooling of a micromechanical resonator.* Nature **444**(7115), 75 (2006)

[164] M. D. LaHaye, O. Buu, B. Camarota and K. C. Schwab. *Approaching the Quantum Limit of a Nanomechanical Resonator.* Science **304**(5667), 74 (2004)

[165] J. D. Teufel, J. W. Harlow, C. A. Regal and K. W. Lehnert. *Dynamical backaction of microwave fields on a nanomechanical oscillator.* Phys. Rev. Lett. **101**(19), 197203 (2008)

[166] T. J. Kippenberg and K. J. Vahala. *Cavity opto-mechanics.* Opt. Express **15**(25), 17172 (2007)

[167] A. C. Doherty, A. S. Parkins, S. M. Tan and D. F. Walls. *Motional states of atoms in cavity QED.* Phys. Rev. A **57**(6), 4804 (1998)

[168] M. Tavis and F. W. Cummings. *Exact Solution for an N-Molecule-Radiation-Field Hamiltonian.* Phys. Rev. **170**(2), 379 (1968)

[169] P. Horak, S. M. Barnett and H. Ritsch. *Coherent dynamics of Bose-Einstein condensates in high-finesse optical cavities.* Phys. Rev. A **61**(3), 033609 (2000)

[170] R. W. Boyd. *Nonlinear Optics* (Academic Press, Boston, 2008)

[171] A. Dorsel, J. D. McCullen, P. Meystre, E. Vignes and H. Walther. *Optical Bistability and Mirror Confinement Induced by Radiation Pressure.* Phys. Rev. Lett. **51**(17), 1550 (1983)

[172] A. Gozzini, F. Maccarrone, F. Mango, I. Longo and S. Barbarino. *Light-pressure bistability at microwave frequencies.* J. Opt. Soc. Am. B **2**(11), 1841 (1985)

[173] P. Meystre, E. M. Wright, J. D. McCullen and E. Vignes. *Theory of radiation-pressure-driven interferometers.* J. Opt. Soc. Am. B **2**(11), 1830 (1985)

[174] C. Fabre, M. Pinard, S. Bourzeix, A. Heidmann, E. Giacobino and S. Reynaud. *Quantum-noise reduction using a cavity with a movable mirror.* Phys. Rev. A **49**(2), 1337 (1994)

[175] B. S. Sheard, M. B. Gray, C. M. Mow-Lowry, D. E. McClelland and S. E. Whitcomb. *Observation and characterization of an optical spring.* Phys. Rev. A **69**(5), 51801 (2004)

[176] T. J. Kippenberg and K. J. Vahala. *Cavity Optomechanics: Back-Action at the Mesoscale.* Science **321**(5893), 1172 (2008)

[177] M. Ludwig, B. Kubala and F. Marquardt. *The optomechanical instability in the quantum regime.* New J. Phys. **10**(9), 095013 (2008)

[178] A. Rai and G. Agarwal. *Quantum optical spring.* Phys. Rev. A **78**(1), 013831 (2008)

[179] W. H. Zurek. *Cosmological experiments in condensed matter systems.* Phys. Rep. **276**(4), 177 (1996)

[180] T. Caneva, M. Murphy, T. Calarco, R. Fazio, S. Montangero, V. Giovannetti and G. E. Santoro. *Optimal Control at the Quantum Speed Limit.* Phys. Rev. Lett. **103**(24), 240501 (2009)

[181] P. Doria, T. Calarco and S. Montangero. *Optimal Control Technique for Many-Body Quantum Dynamics.* Phys. Rev. Lett. **106**(19), 190501 (2011)

[182] T. Caneva, T. Calarco, R. Fazio, G. E. Santoro and S. Montangero. *Speeding up critical system dynamics through optimized evolution.* arXiv:1011.6634 (2010)

[183] L. I. Schiff. *Quantum Mechanics* (McGraw-Hill Book Company, 1986), 3rd edition

[184] I. N. Bronstein, K. A. Semendjajew, G. Musiol and H. Mühlig. *Taschenbuch der Mathematik* (Verlag Harri Deutsch, Thun und Frankfurt am Main, 2001), 5th edition

[185] T. R. Taha and M. I. Ablowitz. *Analytical and numerical aspects of certain nonlinear evolution equations. II. Numerical, nonlinear Schrödinger equation.* J. Comput. Phys. **55**(2), 203 (1984)

[186] J. A. C. Weideman and B. M. Herbst. *Split-Step Methods for the Solution of the Nonlinear Schrodinger Equation.* SIAM J. Numer. Anal. **23**(3), 485 (1986)

[187] W. Bao, D. Jaksch and P. A. Markowich. *Numerical solution of the Gross-Pitaevskii equation for Bose-Einstein condensation.* J. Comput. Phys. **187**(1), 318 (2003)

[188] M. Frigo and S. G. Johnson. *FFTW: an adaptive software architecture for the FFT.* In *Proceedings of the 1998 IEEE International Conference on Acoustics, Speech and Signal Processing*, volume 3, (p. 1381) (1998)

[189] J. Schneider and A. Schenzle. *Output from an atom laser: theory vs. experiment.* Appl. Phys. B **69**(5), 353 (1999)

[190] P. J. Mohr, B. N. Taylor and D. B. Newell. *CODATA recommended values of the fundamental physical constants: 2006.* Rev. Mod. Phys. **80**(2), 633 (2008)

List of publications

List of publications

1. **Exploring symmetry breaking at the Dicke quantum**
   K. Baumann, R. Mottl, F. Brennecke and T. Esslinger
   Physical Review Letters 107, 140402 (2011).

2. **Lasing from defect states in mixed-order organic laser structures**
   K. Baumann, G. Raino, N. Moll, T. Stöferle, J. Bolten, T. Wahlbrink and R.F. Mahrt
   Optoelectronic Integrated Circuits XII 7605, 760502 (2010).

3. **Design and optical characterization of photonic crystal lasers with organic gain material**
   K. Baumann, T. Stöferle, N. Moll, G. Raino, R.F. Mahrt,
   T. Wahlbrink, J. Bolten and U. Scherf
   Journal of Optics 12, 065003 (2010).

4. **Synthetic Quantum Many-Body Systems**
   C. Guerlin, K. Baumann, F. Brennecke, D. Greif, R. Joerdens, S. Leinss,
   N. Strohmaier, L. Tarruell, T. Uehlinger, H. Moritz, and T. Esslinger
   Laser Spectroscopy, 212 (2010).

5. **Dicke quantum phase transition with a superfluid gas in an optical cavity**
   K. Baumann, C. Guerlin, F. Brennecke and T. Esslinger
   Nature 464(7293), 1301 (2010).

6. **Enhanced Surface-Emitting Photonic Device**
   K. Baumann, R.F. Mahrt, N. Moll and T. Stöferle
   US Patent, US2009/0147818 A1 (2009).

7. **Dynamical coupling between a Bose-Einstein condensate and a cavity optical lattice**
   S. Ritter, F. Brennecke, K. Baumann, T. Donner, C. Guerlin and T. Esslinger
   Applied Physics B: Lasers and Optics 95(2), 213 (2009).

8. **Ultra-small footprint photonic crystal lasers with organic gain material**
   K. Baumann, N. Moll, T. Stöferle, T. Wahlbrink, J. Bolten, T. Mollenhauer,
   C. Moormann, B. Wang, U. Scherf and R.F. Mahrt
   Organic Optoelectronics and Photonics III 6999, 699906 (2008).

9. **Fabrication and characterization of Ta2O5 photonic feedback structures**
   T. Wahlbrink, J. Bolten, T. Mollenhauer, H. Kurz,
   K. Baumann, N. Moll, T. Stöferle and R.F. Mahrt
   Microelectronic Engineering 85, 1425 (2008).

10. **Superfluid-Helium Converter for Accumulation and Extraction of Ultracold Neutrons**
    O. Zimmer, K. Baumann, M. Fertl, B. Franke, S. Mironov, C. Plonka,
    D. Rich, P. Schmidt-Wellenburg, H.F. Wirth and B. van den Brandt
    Physical Review Letters 99, 104801 (2007).

11. **Organic mixed-order photonic crystal lasers with ultrasmall footprint**
    K. Baumann, T. Stöferle, N. Moll, R.F. Mahrt, T. Wahlbrink,
    J. Bolten, T. Mollenhauer, C. Moormann and U. Scherf
    Applied Physics Letters 91(17), 171108 (2007).

12. **Time lens for high-resolution neutron time-of-flight spectrometers**
    K. Baumann, R. Gähler, P. Grigoriev and E.I. Kats
    Physical Review A 72(4), 043619 (2005).

Invited Talks

1. **Workshop "Ab-initio modeling of cold gases" (CECAM), Zurich / CH 2009**
2. **Seminar at Centre for Quantum Technologies, Singapore 2010**
3. **International Conference on Atomic Physics (ICAP), Cairns / AUS 2010**
4. **Seminar in the Theory of Condensed Matter Group, University of Cambridge / GBR 2010**
5. **Winter Colloquium on the Physics of Quantum Electronics (PQE), Snowbird / USA 2011**
6. **American Physical Society March Meeting, Dallas / USA 2011**
7. **JILA Seminar, Boulder CO / USA 2011**
8. **NIST Ion Storage Seminar, Boulder CO / USA 2011**
9. **Stanford University, Palo Alto CA / USA 2011**
10. **University of Berkeley, Berkeley CA / USA 2011**

Acknowledgments

The last three years in Zurich have been an amazing time in my life. I joined a wonderful team of friendly, helpful and encouraging people, that created a lively atmosphere both on a personal and scientific level. I would like to thank the people who have accompanied me during my Ph.D. studies:

- A very special thanks goes to Tilman Esslinger, who gave me the opportunity to pursue my Ph.D. studies in his group. His friendly, good-humored and positive personality always made it a pleasure to discuss and work with him. Thank you for all the support during my studies and your way of leading a research group, creating such a lively and inspiring atmosphere.
- I am deeply indebted to all members of the cavity team. Thank you Stephan Ritter for building a fantastic experiment and patiently introducing me to it. Thank you Tobias Donner for assisting me via phone with making my first "own" BEC. Thank you Ferdinand Brennecke for accompanying me throughout my thesis and explaining me all details of the theory. Thank your Christine Guerlin for "suffering" with me through the exciting time of "finding the transition". Thanks Silvan Leinss for the happy experimenting. Thank you Rafael Mottl for spicing up the lab atmosphere. Thanks to our newest member Renate Landig to carry on the good spirit. Thank you all for a wonderful time, great "Hohlraum" physics and stimulating discussion not only about physics.
- Daniel Greif and Jackob Meineke started their Ph.D studies at the same time as i did. Thanks for the good time and the occasional beer.
- Thanks to our lab neighbors, the (from my perspective) old lattice team Niels Strohmaier, Robert Jördens, Leticia Tarruell for standing my loud music (even though Daniel's is not better ☺) and the friendly competition whether cavities or fermions are "better".
- Thanks to the (again from my point of view) old lithium team Henning Moritz, Bruno Zimmermann and Torben Müller for always willing to help and the fruitful discussions. A special thanks goes to Henning for explaining and showing me so much and keeping the group running. Also thanks to Torben for the happy neighborhood.
- Thanks to the new generation of lithium and lattice "people" Thomas Uehlinger, Jean-Phillipe Brantut and David Stadler for the good atmosphere.
- Thanks to our newest group members Sebastian Krinner and Gregor Jotzu for spicing up the group.

- Thanks Alexander Frank for the invention of the KGB muffin. Besides that, thank you for always helping me with all kind of electronic problems, RF "voodoo" and, even though most of my ideas never made it on a PCB, always taking the time to teach me the "art of electronics".
- A very warm thanks goes to Veronica Bürgisser for relieving me of all the administrative work and supporting me wherever possible.
- I want to thank Iacopo Carusotto, Hakan Türeci, Joe Bhaseen, Jonathan Keeling, Ben Simons, Helmut Ritsch and many others for the fruitful scientific collaboration.
- A final thanks goes to my parents, sister and grandmas who have always supported me on my way. Its good to know that i can always count on you. Last but not least, i want to thank Sabrina for our time together and for being patient with me, especially in the last weeks.

Curriculum Vitae

Personal Details

KRISTIAN GOTTHOLD BAUMANN

Date of birth: 7. April, 1983
Place of birth: Leipzig, Germany
Citizenship: German

Am Börtli 17
8049 Zürich
Switzerland
kbaumann@phys.ethz.ch

Education

2008 – 2011	Ph.D. research, Zürich / Switzerland "Eidgenössiche Technische Hochschule"
2007	Diploma, München / Germany "Technische Universität München"
2006 – 2007	Diploma thesis, Zürich / Switzerland "IBM Zurich Research Laboratory"
2006	Internship, San Jose CA / USA "IBM Almaden Research Center"
2005 – 2006	Working Student, München / Germany "Technische Universität München"
2005	Internship, Grenoble / France "Institute Laue Langevin"
2002 – 2007	Undergraduate study, München / Germany "Technische Universität München"
2002	Abitur, Gräfelfing / Germany "Kurt Huber Gymnasium"